OCS Study
BOEMRE 2010-051

# Evaluation of NASA Aura's Data Products for Use in Air Quality Studies over the Gulf of Mexico

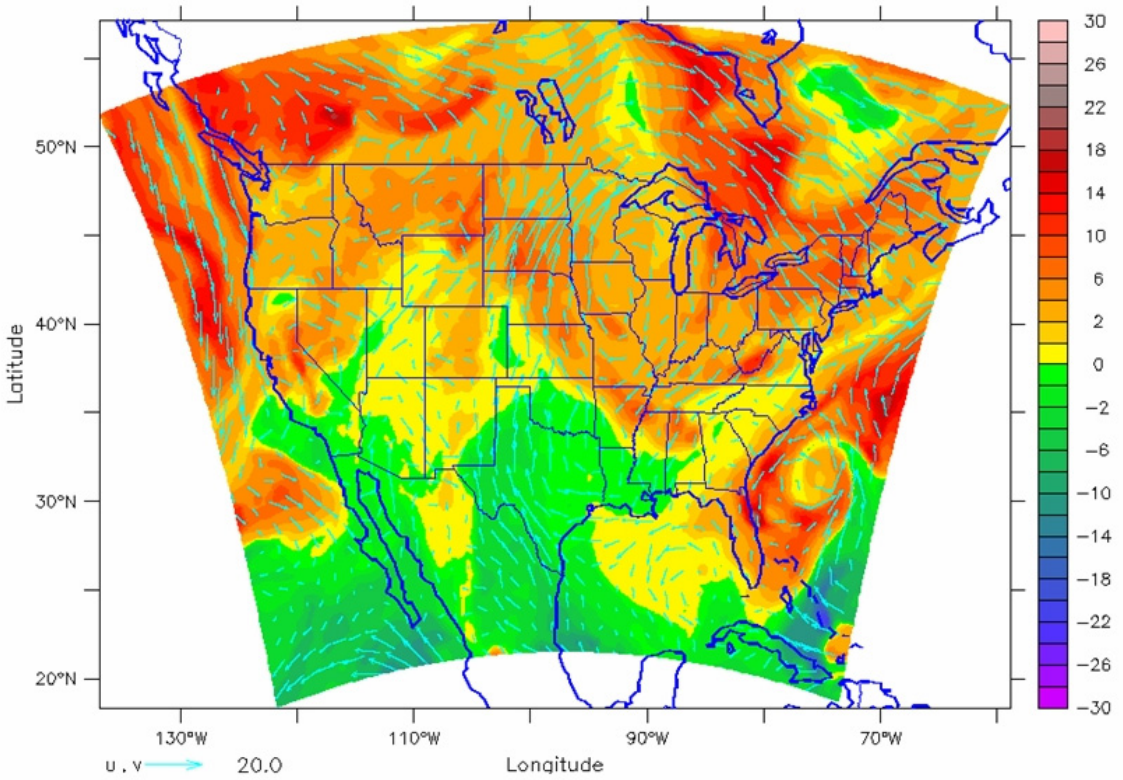


Impact of satellite derived ozone for the lateral boundary at 1-km altitude during August 16, 2006.

**U.S. Department of the Interior**
**Bureau of Ocean Energy Management, Regulation and Enforcement**
**Gulf of Mexico OCS Region**

OCS Study
BOEMRE 2010-051

# Evaluation of NASA Aura's Data Products for Use in Air Quality Studies over the Gulf of Mexico

Authors

A. Pour Biazar
R.T. McNider
Mike Newchurch
Lihua Wang
Yun Hee Park

With contributions from

Maudood Khan
The Universities Space Research Association

Prepared under BOEMRE Cooperative Agreement
M07AC13332/M07AC12463
by
University of Alabama in Huntsville
National Space Science and Technology Center
Earth System Science Center
Huntsville, Alabama 25805

Published by

U.S. Department of the Interior
**Bureau of Ocean Energy Management, Regulation and Enforcement**
**Gulf of Mexico OCS Region**

**New Orleans**
**December 2010**

## DISCLAIMER

This report was prepared under contract between the Bureau of Ocean Energy Management, Regulation and Enforcement (BOEMRE) and the University of Alabama in Huntsville (UAH). This report has been technically reviewed by the BOEMRE, and it has been approved for publication. Approval does not signify that the contents necessarily reflect the views and policies of the BOEMRE, nor does mention of trade names or commercial products constitute endorsement or recommendation for use. It is, however, exempt from review and compliance with the BOEMRE editorial standards.

## REPORT AVAILABILITY

This report is available only in compact disc format from the Bureau of Ocean Energy Management, Regulation and Enforcement, Gulf of Mexico OCS Region, at a charge of $15.00, by referencing OCS Study BOEMRE 2010-051. The report may be downloaded from the BOEMRE website through the Environmental Studies Program Information System (ESPIS). You will be able to obtain this report also from the National Technical Information Service in the near future. Here are the addresses. You may also inspect copies at selected Federal Depository Libraries.

Bureau of Ocean Energy Management,
Regulation and Enforcement
Gulf of Mexico OCS Region
Public Information Office (MS 5034)
1201 Elmwood Park Boulevard
New Orleans, Louisiana 70123-2394
Telephone requests may be placed at
(504) 736-2519, 1-800-200-GULF, or
Rush Orders: 1-800-553-6847
Fax: (504) 736-2620

U.S. Department of Commerce
National Technical Information Service
5285 Port Royal Road
Springfield, Virginia 22161
Phone: (703) 605-6040
Fax: (703) 605-6900
Email: bookstore@ntis.gov

## CITATION

Biazar, A.P., R.T. McNider, M. Newchurch, M. Khan, Y.H. Park, and L. Wang. 2010. Evaluation of NASA AURA's data products for use in air quality studies over the Gulf of Mexico. U.S. Dept. of the Interior, Bureau of Ocean Energy Management, Regulation and Enforcement, Gulf of Mexico OCS Region, New Orleans, LA. OCS Study BOEMRE 2010-051. 82 pp.

## ACKNOWLEDGMENTS

This work was accomplished under partial support from the Bureau of Ocean Energy Management, Regulation and Enforcement under Cooperative Agreement Between the University of Alabama in Huntsville and the Bureau of Ocean Energy Management, Regulation and Enforcement on Gulf of Mexico Issues, and the NASA Science Mission Directorate Applied Sciences Program.

# TABLE OF CONTENTS

# LIST OF FIGURES

# LIST OF TABLES

# 1. EXECUTIVE SUMMARY

## 1.1. Problem Statement

The Bureau of Ocean Energy Management, Regulation and Enforcement (BOEMRE), a bureau in the U.S. Department of the Interior (DOI), is responsible for the management of mineral resources on the outer continental shelf (OCS), and for regulating the activities of offshore operators. One of BOEMRE's regulatory obligations is the assessment of potential environmental impact of oil and gas operations in the Gulf of Mexico (GoM) and in particular the onshore air quality impact of such operations. GoM region is home to some of the most precious and sensitive habitats. Several coastal areas in the northeastern Gulf of Mexico have been designated as Wildlife Refuges and National Preserves. Some of these areas are assigned Class I and II status by the U.S. Environmental Protection Agency (EPA), and are subject to the most rigorous requirements for air quality. Due to such sensitivities, confidence in air quality assessments and reducing the uncertainties in the air quality studies over the GoM region is imperative. Furthermore, in adapting sound policies for control strategies, it is crucial to assess the impact of local pollution versus transboundary air pollution, and in a region such as GoM with scarce monitoring capability over open waters represents a challenge.

Since air quality models are utilized for assessing the impacts of offshore operations, the inaccuracies in the model predictions of pollutants can significantly affect the outcome of impacts analysis. In assessing the potential onshore impact of ozone from OCS sources, one source of uncertainty in photochemical models is the specification of the background air. Errors in the specification of background concentrations of ozone and its precursors will propagate in the model and impact model predictions of ozone. Therefore, decreasing such reducible errors is of interest to BOEMRE.

Regional air quality can be impacted by larger scale atmospheric motions that carry polluted air into a region through long range transport and cause enhancements in background levels of ozone and its precursors. Therefore it is essential for regional air quality modeling studies to be able to include transboundary air pollution. The usual practice in regional modeling is to nest the region within a much larger domain so that the impact of emission sources outside the region of study is included. Given the emission sources within the larger domain are well represented, this approach can reduce the propagation of the error due to ill defined boundary concentrations for short term forecasts. However, for regions neighboring ocean like GoM region such an approach may not be as effective due to the lack of information over the water.

The GoM region is impacted by the recirculation of pollution in the southeastern United States. High pressure systems such as Bermuda high transport pollution from northeast over the waters off the east coast and recirculate it to the GoM region through southerly/southeasterly flow. If model simulations do not extend the domain far enough over the Atlantic Ocean to fully realize the impact of such recirculation, they introduce another source of uncertainty for GoM air quality assessments.

Volatile organic compounds (VOCs) and oxides of nitrogen ($NO_x$) are the main precursors of ozone in the boundary layer. They play an important role in the chemical composition of the troposphere. During the summer in the eastern United States there are two active natural sources for these compounds; i.e., hydrocarbon emissions in the boundary layer from highly vegetated landscape of the eastern U.S., and oxides of nitrogen from dense lightning activities in this region. Southeastern United States has a unique characteristic as far as air pollution is concerned. The region is highly vegetated and rich in biogenic hydrocarbons during the summer. The region is also impacted by the dominant summertime Bermuda high that creates a stagnant condition inducive to frequent afternoon convective activities with high frequency of lightning events (producing $NO_x$). All of this is complemented by anthropogenic $NO_x$/VOC emissions in the region. The abundance of natural sources of precursors together with the anthropogenic emissions creates a suitable environment for regional scale pollution that can impact the GoM region through recirculation.

## 1.2. Overview of the Current Project

Newly available satellite observations of tropospheric gases and aerosols have the potential to provide the necessary data to reduce the aforementioned uncertainties. In the current project we examined the viability of the satellite observations of ozone and aerosols for reducing the errors in the specification of background air and in improving the air quality model predictions. Such improvements will provide better estimates of ozone and aerosols for BOEMRE air quality assessments and the GoM region's state agencies.

This project originally focused on examining the ozone observations by Tropospheric Emission Spectrometer (TES) onboard Aura satellite. But soon after the start of the project it became clear that other sensors aboard Aura as well as sensors onboard other satellites like Terra (EOS AM) and Aqua (EOS PM) provide complimentary data that could be useful in providing a more comprehensive description of boundary layer and free tropospheric chemical composition. This project also took advantage of our active collaboration with the Smithsonian Astrophysical Observatory (SAO) to obtain the first available ozone profiles from Ozone Monitoring Instrument (OMI). A major challenge in using TES ozone measurements is the small footprint and poor spatial coverage. OMI on the other hand does not have those limitations but until recently it was only providing total column measurements of ozone.

UAH is currently operating an ozonesonde station at the National Space Science and Technology Center (NSSTC). UAH was also involved in the Intercontinental Chemical Transport Experiment Ozonesonde Network Study 2006 (IONS-06) campaign and was one of the ozonesonde launch sites for evaluating ozone observations from TES. In this project, we used ozonesonde data from UAH and other IONS-06 stations for evaluation of TES and OMI vertical profiles. We also used this data for model evaluation. The Fifth-Generation NCAR/Penn State Mesoscale Model (MM5) (http://www.mmm.ucar.edu/mm5) and the EPA's Community Multiscale Air Quality (CMAQ) (http://www.cmascenter.org) modeling system were used for modeling.

The key question we have addressed in this project is whether the satellite data can be utilized in air quality assessments, either for improving model performance or for evaluation. In doing so, we have (1) evaluated several satellite products, namely TES and OMI ozone profiles, and the Moderate Resolution Imaging Spectroradiometer (MODIS) aerosol products, (2) devised techniques for the utilization of satellite data in the model, and (3) performed model simulations for August 2006 and evaluated the results against ozonesonde and surface observations. In the following each of these components will be explained in detail.

## 2. APPROACH

The satellite data we have considered thus far are TES and OMI ozone data and MODIS aerosol products. We have chosen summer of 2006, focused on the month of August, as the period of study. This period coincides with IONS-06 and provides a comprehensive daily ozonesonde observation. With respect to OMI and TES ozone, first the satellite data for the continental United States were extracted and evaluated against ozonesonde observations for this period. Then, this quality assured data were mapped onto the model domain and used in model simulations by modifying daily initial and boundary conditions in the simulations. In this section the data and the techniques for their utilization in the model are explained. Then a description of the model configuration for different simulations will be presented.

### 2.1. Satellite Data

Since 2002 NASA has launched a series of satellites with sun-synchronous orbits in close proximity to each other. They all pass the equator within few minutes of each other at around 1:30 PM local time. Since their formation in some ways is analogous to a train that passes over the equator in early afternoon, the constellation of satellites is referred to as "A-Train."

**Figure** 1 illustrates the A-Train constellation with an indication of the local time of their overpass. Aqua, launched in 2002, is the leading satellite in this constellation making observations at 1:30 PM local time, and Aura, launched July 15, 2004, is the trailing satellite with 1:38 PM overpass. Other NASA satellites in this constellation are CloudSAT, CALIPSO and PARABOL (http://www.nasa.gov/missions/index.html).

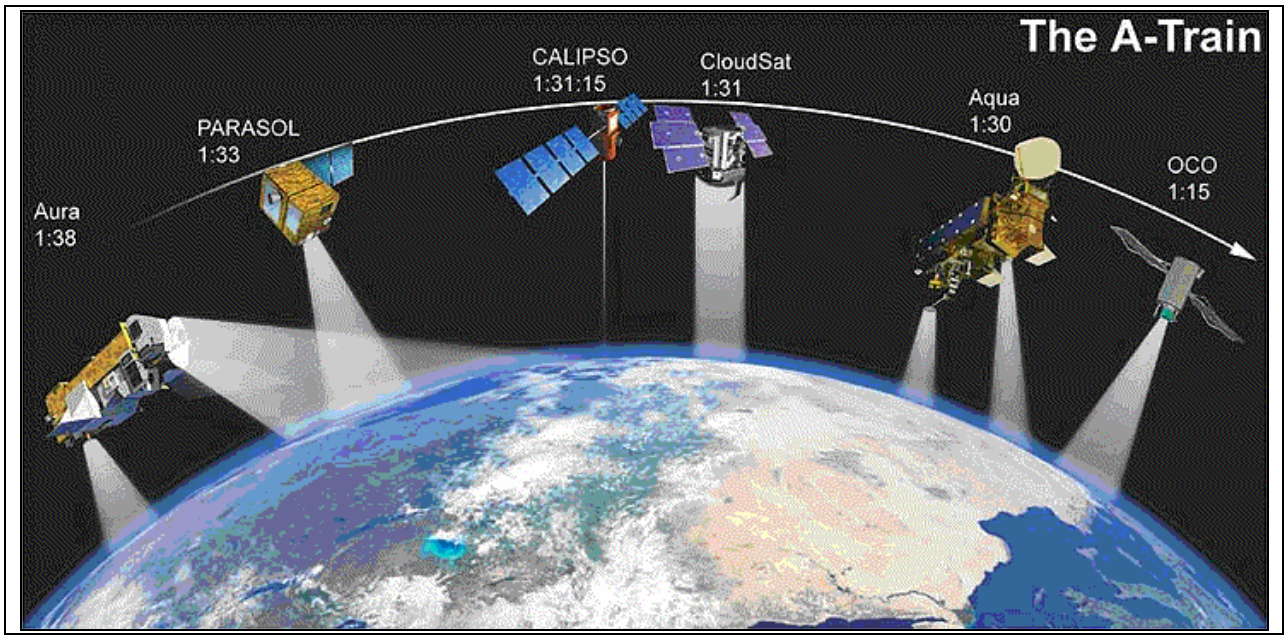


**Figure 1. A-Train constellation. The times indicated are the local solar time that the satellite passes over equator, which is also the local time for the observation of any given point in the viewing window.**

In this project we have utilized data from different sensors onboard Aqua, Aura, CALIPSO, and a morning satellite Terra. Launched in December 18, 1999, Terra is a morning sun-synchronous satellite crossing the equator at 10:30 AM. In this project we utilized the aerosol products from MODIS onboard Terra and Aqua. Use of data from both morning and afternoon observations helped increase the spatial coverage of the data. Since the MODIS instrument cannot "see" through the clouds, combining the morning and the afternoon overpasses increases the chances of having observation for locations that were cloudy only for part of the day.

### 2.1.1. AURA Satellite

Aura (Latin for breeze) mission was launched in 2004 as part of Earth Observing System (EOS) program. It was launched into an ascending-node (705-km altitude) sun-synchronous polar orbit with a 98˚ inclination with an equator-crossing time of 13:45 (about 15 minutes behind Aqua) and 16 day repeat cycle with the design life of five years (Schoeberl et al., 2006). Aura carries four instruments: the High Resolution Dynamics Limb Sounder (HIRDLS), the Microwave Limb Sounder (MLS), the Ozone Monitoring Instrument (OMI), and the Tropospheric Emission Spectrometer (TES). **Figure 2** shows the vertical range of Aura measurements for each of the instruments onboard Aura. The two sensors of interest to this study are TES and OMI. In the following sections these sensors and their measurements will be described in more detail.

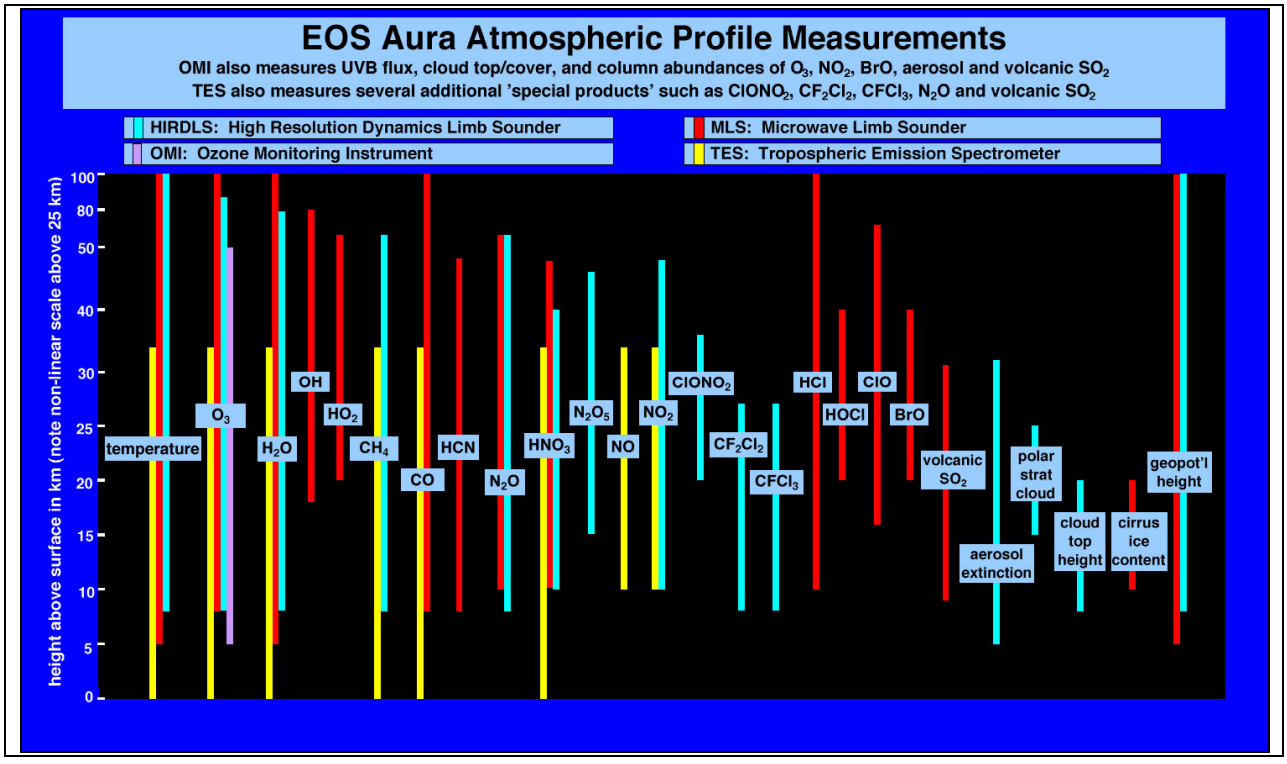


**Figure 2. Aura instrument measurements and their height range based on pre-launch design. Column measurements are indicated in the lower part of the figure. Adapted from Schoeberl et al. (2006).**

#### *2.1.1.1. Tropospheric Emission Spectrometer (TES)*

The Tropospheric Emission Spectrometer (TES) onboard the Aura satellite was designed to measure the global vertical distribution of tropospheric ozone as well as temperature and some other tropospheric species including carbon monoxide and water vapor [*Beer et al.*, 2001; *Beer*, 2006]. Initial validation of TES ozone was carried out by comparing a limited number of early measurements to ozonesondes, using the first version of TES nadir ozone data (V001) [*Worden et al.*, 2007].

TES is a Fourier transform spectrometer that measures infrared emission of Earth's atmosphere. Although TES can measure from both the nadir (directly below the sensor) and limb (side) views, nadir is presently the primary scanning geometry used. In cloud-free conditions, the nadir ozone profiles have approximately four degrees of freedom for signal, approximately two of which are in the troposphere, giving an estimated vertical resolution of about 6 km [*Bowman et al.*, 2002; *Worden et al.*, 2004; *Worden et al.*, 2007] with a 5.3 km by 8.3 km footprint.

The primary measurement mode for TES is the Global Survey (GS), from which the instrument maps the earth in 16 orbits (~26 hours). The measurements in a global survey are divided into sequences which take about 82 seconds each. Prior to May 2005, each of these sequences consisted of 3 limb scans and 2 nadir scans. The radiances from the two nadir scans (which were made of the same spot) were averaged together. Nadir measurements in successive sequences were separated by about 544 km, while measurements from the neighboring TES orbit tracks were separated by 22º longitude (about 2100 km at 30° N). In the present GS configuration, which began on 21 May 2005, a sequence consists of three nadir scans and no limb scans. In the new GS mode, each nadir scan along the track is separated by about 182 km on the ground. The radiances are not averaged [*Beer*, 2006; *Osterman et al.*, 2008] and the measurements provide more coverage.

TES also has special observation modes, the most common one being the Step and Stare (SS), where numerous repetitive measurements are made near a given target, with scans about 6 seconds apart and separated by 40-45 km along the ground track [*Beer*, 2006; *Osterman et al.*, 2008]. Another common special observation mode is transecting mode, in which repetitive scans are made where the nadir angle changes such that the footprints from subsequent scans are only about 12 km apart. Accumulating transect scans can thus create a nearly contiguous footprint spanning about 500 km.

TES ozone is retrieved from the 9.6-μm ozone absorption band using the 995-1,070-$cm^{-1}$ spectral range. The retrievals and error estimation are based on the optimal estimation approach [*Rodgers*, 2000]. TES retrievals are described in *Worden et al.* [2004] and *Bowman et al.* [2002, 2006], with error characterization described in *Kulawik et al*. [2006]. Temperature, water vapor and ozone are simultaneously retrieved in the first step of the retrieval with other species and parameters retrieved in subsequent steps. A priori profile (also used as the initial guess) and covariance matrix are derived from ozone climatology developed using the MOZART model [*Brasseur et al.*, 1998; *Park et al.*, 2004]. To facilitate use of TES data, the averaging kernel matrix and prior constraint matrix are made available with the data, which may be obtained from

the TES website (http://tes.jpl.nasa.gov). A detailed description of TES data is given in Osterman et. al. (2008) and the TES Level 2 Data User's Guide, Version 2.0 (*Osterman et al.*, 2006). The user's guide can be obtained from http://tes.jpl.nasa.gov/documents).

Nassar et al. (2008) extensively evaluated TES observations against IONS-06 and other available ozonesonde data. They reported an overall positive bias of 3-10 ppb in TES ozone measurements. **Figure 3** adapted from Nassar et al. shows the difference between TES retrievals and coincident ozonesonde measurements for different seasons in midlatitudes (35-60° N). As evident from the figure the differences both in terms of absolute difference and percentage are large. In particular, during the summer months which are of interest to the air quality community these differences are the highest in the boundary layer and in the upper troposphere. Summer of 2006 also has the highest number of samples for comparison as the IONS-06 campaign was designed for the purpose of validating TES observations. The ozonesonde launch times were coordinated to coincide with Aura's overpasses. It should be noted, however, that the ozonesonde data in these comparisons have been corrected for TES measurement sensitivity and vertical resolution by applying TES averaging kernels.

The main problem in utilizing TES observations as direct input in air quality modeling practices is not its accuracy, but is the sparseness of observations and their relatively small footprint. This presents a challenge for their use in regional modeling. **Figure 4** shows an example of TES ozone observations for the week of August 25-31, 2006, in the boundary layer. Ozone concentrations have been marked on the actual observations footprint on the map. As evident from the figure the actual footprint is so small relative to the gaps in the observations that it is hard to see the markings. Since the orbits are repeated every 16 days, averaging the data for a longer period of time will not help in filling up the gaps. This remains to be a challenge in absorbing/assimilating TES data in the photochemical models, since any correction made to the model as the result of these observations will be limited.

#### *2.1.1.2. Ozone Monitoring Instrument (OMI)*

One approach for better use of TES data would be the use of complementary information from other sensors aboard Aura. Both lower-tropospheric ozone and upper-tropospheric ozone signals are clearly apparent in UV backscatter instruments. The Global Ozone Monitoring Experiment (GOME) ozone monitoring instrument aboard the European Remote Sensing satellite (ERS-2) [*Burrows et al.*, 1999; *Chance et al.*, 1998; *Hoogen et al.*, 1999] and Total Ozone Mapping Spectrometer (TOMS) [*Chandra et al.*, 2003; *Fishman and Brackett*, 1997; *Kim and Newchurch*, 1998; *Newchurch et al.*, 2001; *Ziemke et al.*, 2000] present a rich literature of tropospheric ozone observations from space. The Ozone Monitoring Instrument (OMI) aboard Aura likewise measures tropospheric ozone. It is important to realize that one of the most important regions of ozone variation is in the boundary layer and that OMI should do at least as well as TOMS in this region and TOMS sees significant signal there [*Kim et al.*, 2001; *Newchurch et al.*, 2001].

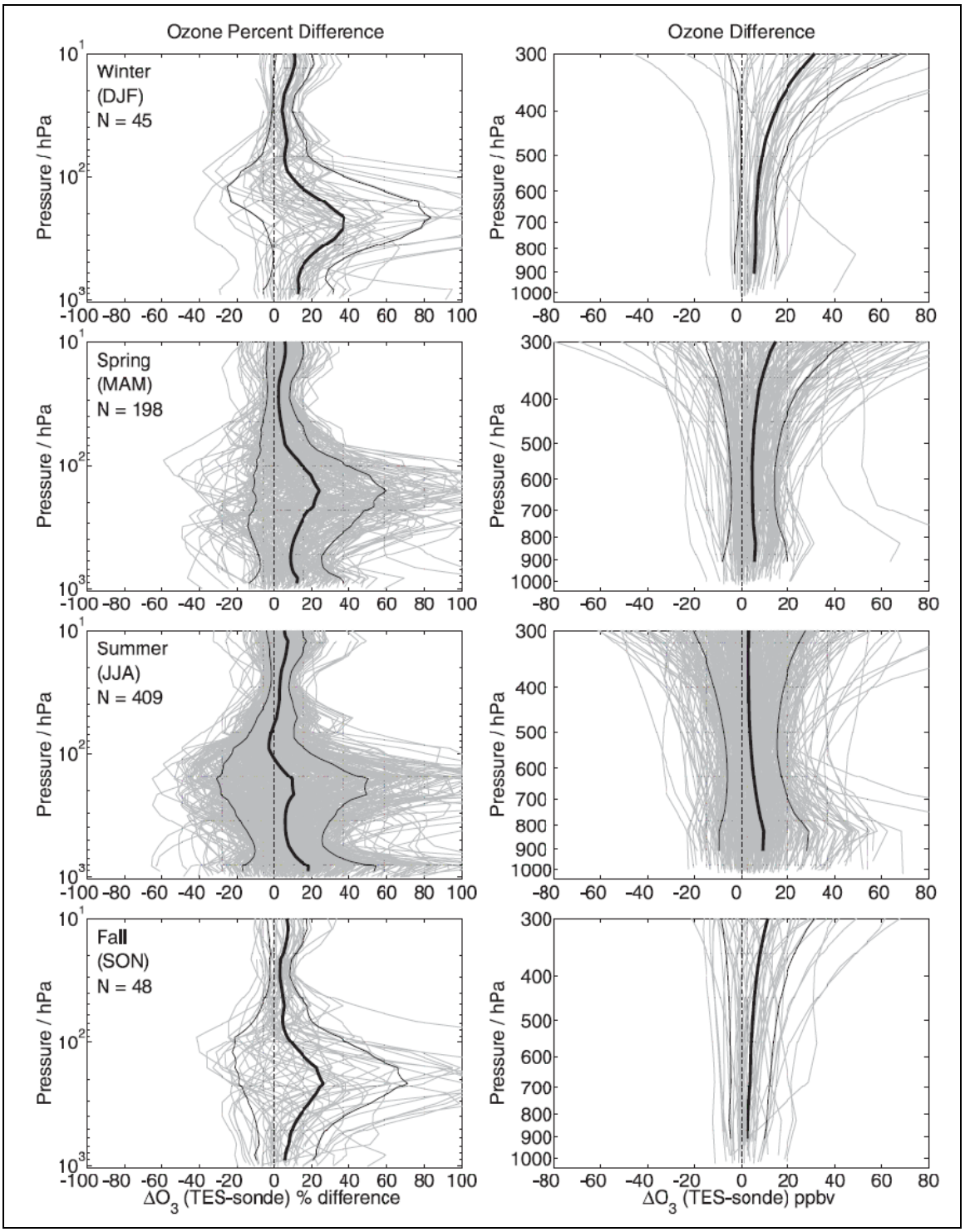


**Figure 3. Differences between TES retrievals and ozonesonde measurements for different seasons in northern midlatitudes (35-60° N). N indicates the number of coincidences used. Adapted from Nassar et al. (2008).**

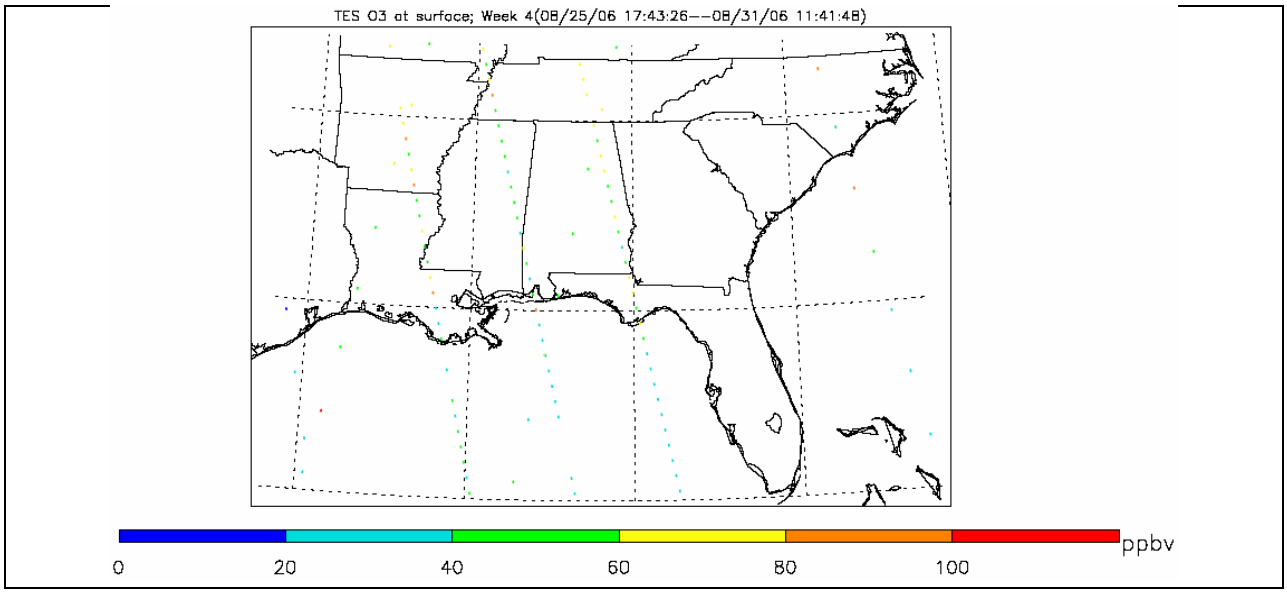


**Figure 4. Surface ozone concentrations as observed by TES for the week of August 25-31, 2006. The figure presents ALL the available observations (including both global survey (GS) and special observation (SO) modes) mapped on the actual TES observed footprint (~ 5.3x8.3 km$^2$). Adjacent tracks are separated by about 22° longitudes apart (2200km). Observations along the ground track are separated by about 544-km (old GS mode, prior to May 21, 2005), or 182-km (new GS mode, after May 21, 2005), or 40-45 km (SO mode), or 12 km in transect mode.**

OMI is a nadir-viewing near-UV/Visible charge-coupled device (CCD) spectrometer that was designed to measure the total columns of $O_3$, HCHO and $NO_2$, with a nominal ground footprint of 13x24 km$^2$ at nadir. OMI has been collecting data since August 9, 2004, and provides a complete global coverage in one day. OMI measurements cover a spectral region of 264-504 nm (nanometers) with a spectral resolution between .42 and .63 nm. OMI provides ozone column measurements for a ground footprint of 13x24 km$^2$ and ozone profiles at 13x48 km$^2$. OMI level 2 data can be obtained from http://disc.sci.gsfc.nasa.gov/data/datapool/OMI/Level2_V003.

Through our collaborations with Dr. Xiong Liu of the Harvard-Smithsonian Center for Astrophysics we were able to obtain the first ozone profiles retrieved from OMI. Dr. Liu who had already constructed ozone profiles from GOME (Global Ozone Monitoring Experiment, a sensor similar to OMI) aboard a European satellite, was about to apply his technique to OMI when this project was started (Liu et al., 2005, 2006a, 2006b). The current project helped in evaluating his product as well as assessing its efficacy for air quality studies. This product would become part of the standard OMI data products. Dr. Liu provided $O_3$ profiles retrieved from OMI measurements for the period of July-September 2006 that spans over the period of our study.

OMI $O_3$ profiles were provided on 24 fixed pressure layers in Dobson Units (DU). The partial column ozone $O_{3,i}$ (DU) can be easily converted to mean mixing ratio $O_{3,i}$ (ppbv) at each layer using the following formula (by assuming ozone is well mixed in that layer):

$$O_{3,i}\ (ppbv) = 1.251 \times O_{3,i}\ (DU) / (P_{i+1} - P_i) \times 1013.25 \times (R / (R + Z_{mid,\,i}))^2$$

Where $P_{i+1}$, $P_i$ are the pressure in mb at two levels bounding layer i, R is the radius of earth, and $Z_{mid,i}$ is the average altitude of the layer. This formula is accurate to better than 1%. Using this relationship avoids the need for temperature in the conversion (Liu, personal communication). Similarly, the tropospheric column ozone can be converted to mean mixing ratio by using tropopause and surface pressure. Using mixing ratio has certain advantages over using tropospheric column ozone by reducing the variability simply due to the tropopause and surface pressure.

Averaging kernels ( $A(i,j) = \partial x_j / \partial x_i$ ) and a priori profiles used in the retrievals are also reported as part of the data. Averaging kernels represent the sensitivity of retrieved partial column ozone (DU) at layer j to the change in ozone (DU) at layer i (from the a priori column ozone). They indicate retrieval sensitivity and the vertical resolution of retrievals. The averaging kernels are dependent on the unit used and the conversion from DU to ppbv varies with altitude (e.g. resulting from different T, P). Therefore, if used in evaluation this fact must be considered.

Averaging kernels are generally used when the satellite retrievals are compared with ozonesonde or model simulations that have higher vertical resolution. They are applied to the higher resolution data to make them compatible with satellite data. The process involves the conversion of high resolution data to partial column ozone (DU) and using convolution to construct a modified ozone field compatible with the satellite observation. The following relationship is used:

$$X'_j = X_{a,j} + \sum_{i=1}^{n} A_{(i,j)} \times (X_{o,i} - X_{a,i})$$

Where $n$ is the number of layers in the retrieval, $X_{a,.}$ is the a priori profile, $A_{(i,j)}$ is the averaging kernel, $X_{o,.}$ is the high resolution data (ozonesonde or model) converted to DU, and $X'_.$ is the modified $O_3$ fields to be used in the evaluation.

Since our objective is the direct insertion of satellite data in the model, we decided on having model vertical structure (vertical levels) as the single vertical coordinate for our exercise. Therefore, all other data (satellite and ozonesonde) are interpolated/integrated onto the model vertical layers and used for both insertion into the model and evaluation of the results.

While for this project we have examined the efficacy of OMI $O_3$ profiles in air quality studies, we are also pursuing the use of other OMI products such as formaldehyde (HCHO) and nitrogen dioxide ($NO_2$) in conjunction with carbon monoxide from The Atmospheric Infrared Sounder (AIRS) onboard Aqua. Together these products may have the potential of providing a more complete representation of regional background air.

#### *2.1.1.3. Mapping OMI* and *AIRS Observations Onto the CMAQ Model Domain*

Daily OMI $O_3$ measurements were gridded onto CMAQ 36 km by 36 km resolution by using a so-called "drop-in-the-box" method. $O_3$ retrieval for each OMI pixel is assigned to those CMAQ grids whose center points fall within this specific OMI pixel. For a CMAQ grid that receives more than one OMI $O_3$ values, a simple averaging was applied to get the daily mean. The original OMI $O_3$ data set has already filtered out some unreasonable values, and we have not applied any further filtering criteria yet. A "Nearest-Neighboring-Interpolation" (NNI) method was also used on the gridded OMI $O_3$ data in order to fill those missing values by averaging the available OMI $O_3$ values from the nearest neighboring CMAQ grids. It is assumed that if OMI data is missing due to some data contamination on a small scale, then NNI method will produce a reasonable concentration and helps in increasing the data coverage. This technique also spatially smoothes the concentration fields over the model domain and reduces unreasonable variations that may be caused from merging observations into the model. Finally, OMI $O_3$ profiles within the CMAQ domain are vertically interpolated onto the 39 sigma-P pressure layers of CMAQ model.

Our initial approach to vertical interpolation was log/linear interpolation on pressure levels. This approach, while reasonable for most of the troposphere, was problematic in areas where there is a curvature and high vertical gradient, such as boundary layer and upper troposphere. In our subsequent simulations we have used a robust combination of spline and linear interpolation to better map the low resolution OMI observations onto the high resolution model vertical layers. An example of vertical interpolation is demonstrated in **Figure 5** for Huntsville, Alabama, on August 1, 2006.

We used similar approach to grid the tropospheric columns of OMI/HCHO, OMI/$NO_2$ and AIRS/CO onto CMAQ horizontal domain. Fitting uncertainties for the HCHO slant columns typically range between 40-100%, with the lower end of this range over HCHO hot-spots. Our future plans are to also use formaldehyde and nitrogen dioxide observations from OMI. Since OMI measures HCHO and $NO_2$ columns, we plan to scale them onto CMAQ vertical layers based on the vertical distribution patterns from CMAQ control simulations.

The AIRS sensor aboard Aqua spacecraft measures humidity, temperature, cloud properties, and the amounts of greenhouse gases. We expect to utilize AIRS CO as another complementary piece of information to better describe the background characteristics of boundary layer air from remote sensing platforms. AIRS Level 2/Level 3 Version 005 CO (without Humidity Sounder for Brazil, HSB) for August 2006 is available. There is 0.5 to 1.5 degrees of freedom (number of adjustable geophysical parameters in the retrieval; indicates the amount of information in the retrieval) in the AIRS CO signal that is translated into a vertically weighted total column with the shape of the weighting varying depending on local conditions (temperature, moisture, and CO amount and true profile). Nominally, AIRS CO sensitivity peaks at 500 mb, ± 200 mb. AIRS CO does respond to polluted boundary layers, but generally it underestimates the boundary layer mixing ratio (too close to the surface). With a 45-km footprint for retrievals, AIRS mixing ratios will tend to be lower than in situ for all but the largest plumes.

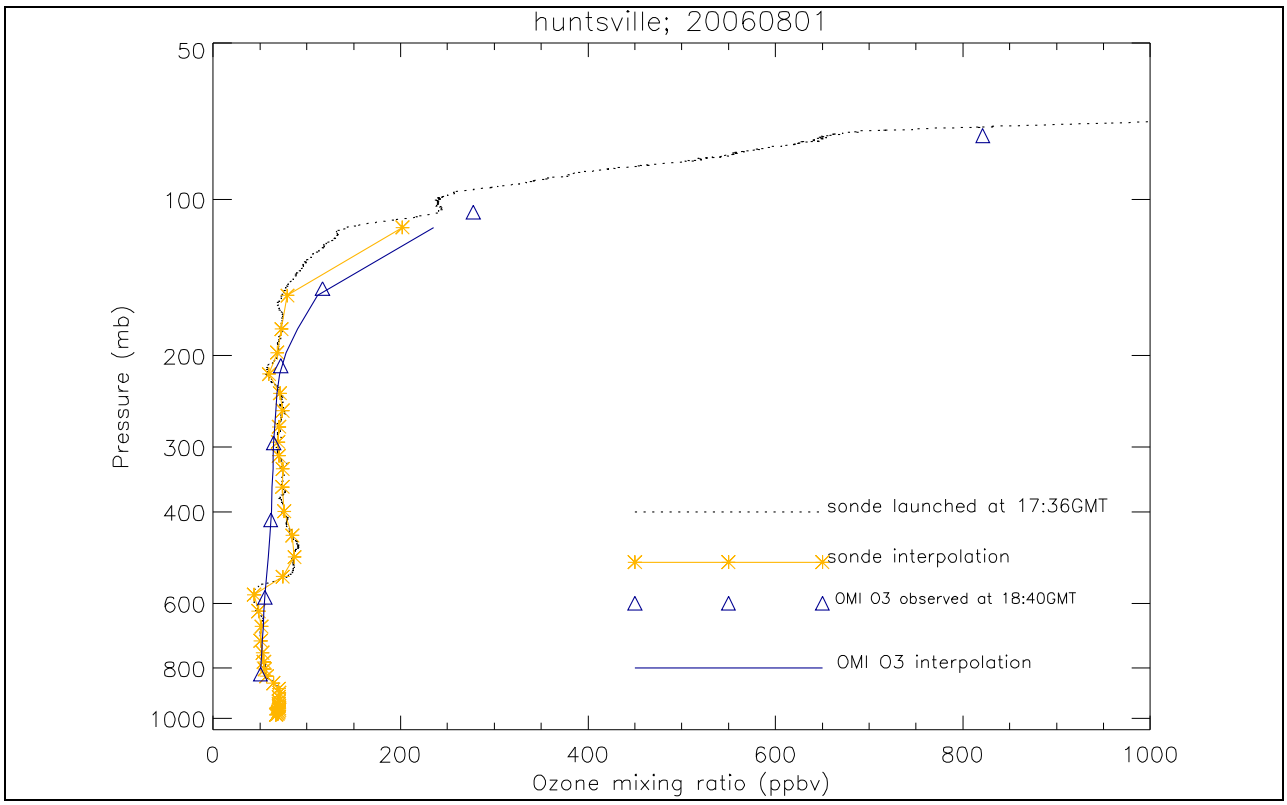


**Figure 5. Example of OMI ozone profile and ozonesonde measurements interpolated onto the CMAQ vertical grid for Huntsville, Alabama, on August 1, 2006.**

**Figure 6** shows OMI ozone observations at two pressure levels, one representing 485-700 mb and the other 700-mb surface for August 21, 2006. The left panel shows OMI ozone values on their native tracks. The pixel sizes do not represent the real footprint of the measurements and have been downsized to better show the tracks. On the right panel the concentrations after being mapped onto the 36-kmx36-km model domain are demonstrated. As evident from the figure, merging all the tracks for one day provides a complete spatial coverage over the continental United States. This is of outmost importance as the spatial extent of highs and lows (ridges and troughs) can be realized.

**Figure 7** demonstrates OMI column nitrogen dioxide ($NO_2$) and formaldehyde (HCHO) observations mapped into the 36-km model domain for the same day. One can observe the similarity of $NO_2$ spatial pattern over the southeast to the mid-tropospheric ozone. This can be just a coincidence, but it shows the potential value of utilizing complimentary information together.

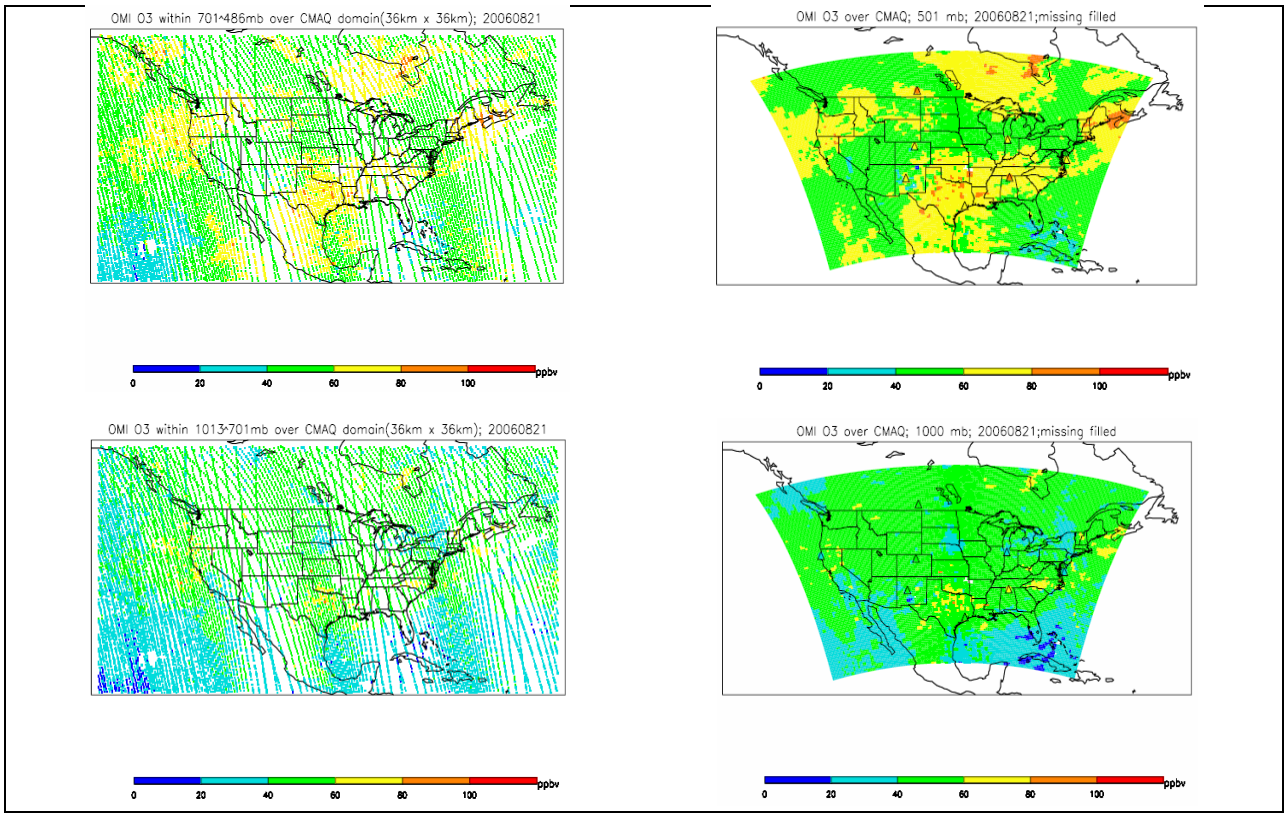


**Figure 6. Aura/OMI Level 2 $O_3$ profiles (24 layers) are mapped to CMAQ horizontal domain (36km x 36km) using a "drop-in-the-box" method. The daily-mean profiles are then interpolated to CMAQ 39 vertical layers (altitude-based). Left: OMI $O_3$ plotted with fixed pixel size (not real size) at ~500 and ~1000 mb; Right: OMI $O_3$ mapped to CMAQ 3-D domain (36kmx36km, 39 layers); ozonesondes from IONS06 plotted over OMI contours.**

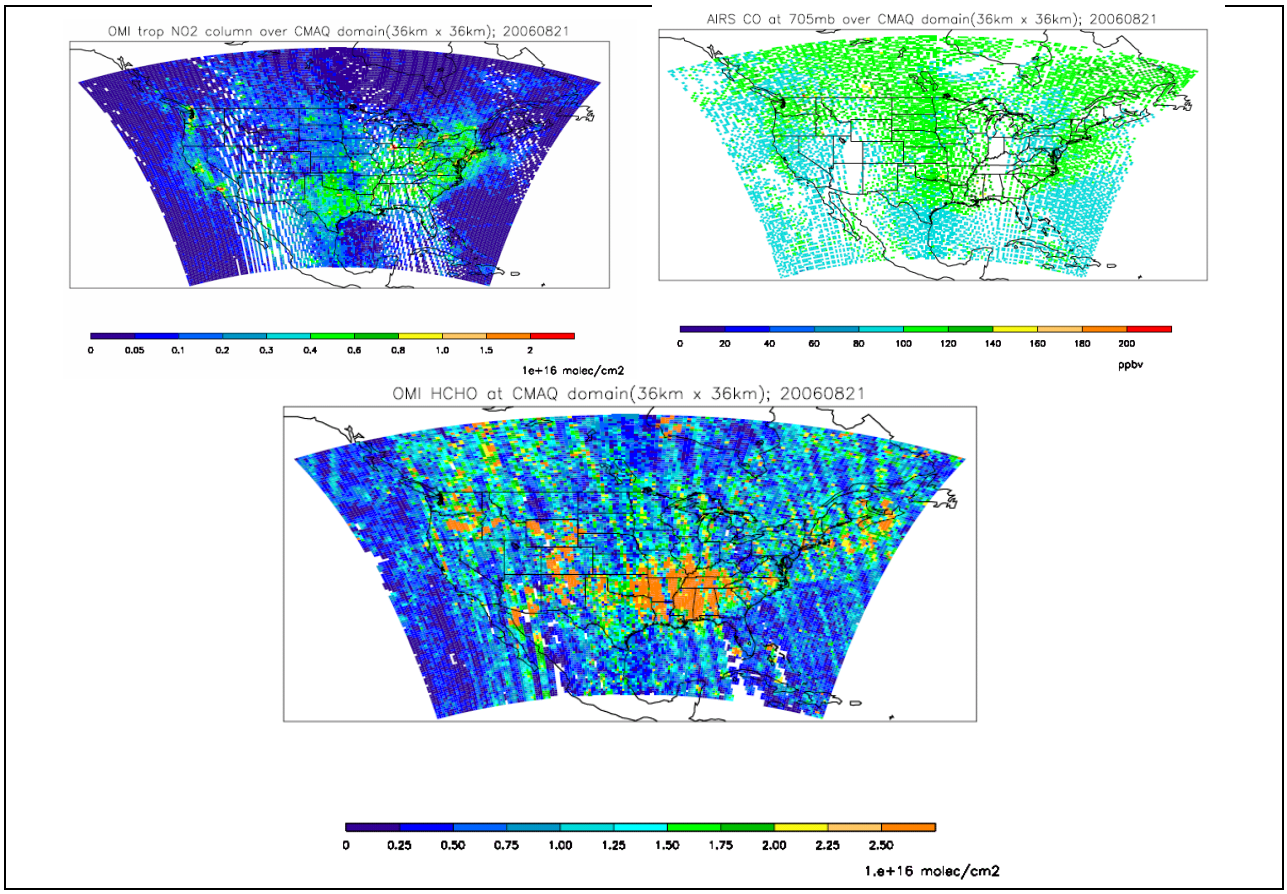


**Figure 7. Satellite-retrieved trace gases (OMI-$NO_2$, OMI-HCHO, and AIRS-CO) is gridded to CMAQ 36km x 36km domain.**

### 2.1.2. Terra and Aqua Satellites (MODIS Instrument)

Particulate Matter (PM) is one of the important aspects of air quality. Realistic representation of emission, transport, and removal of particulate matter is essential in air quality studies. Air quality models require datasets for initializing and specifying the lateral boundary conditions in the case of limited area models. Ground observations provide routine observations of PM but have limited spatial coverage. Column burden of atmospheric aerosols are readily retrieved from multi-channel satellite imagery. Satellite-retrieved aerosol optical depth (AOD) and mean particle size are available at spatial resolutions that are adequate for use in air quality models. While the total column AOD from the satellite provides the spatial distribution of aerosol burden, the vertical distribution of aerosols is also needed to utilize such data in air quality models. However, only a few satellite sensors provide vertical distribution of atmospheric aerosols on a limited spatial coverage (e.g., the Cloud-Aerosol Lidar and Infrared Pathfinder Satellite Observation, CALIPSO). In this project we examine a technique for utilizing Moderate Resolution Imaging Spectroradiometer (MODIS) retrieved aerosol optical depths in CMAQ which is a widely used air quality model. The technique uses CMAQ-predicted vertical distribution of aerosols as the template for distributing satellite-derived AOD into atmospheric columns in CMAQ. This is based on the assumption that the spatial distribution

of emission sources are reasonably defined in the model and the model performs reasonably well with respect to vertical mixing. Therefore, the discrepancy between the model AOD and the observed AOD are due to either emission source strength or the representation of aerosol chemistry/formation in the model. This project quantifies enhancement to air quality predictions derived through the use of satellite observed aerosol fields in the CMAQ model.

MODIS is an instrument aboard the Terra (EOS AM) and Aqua (EOS PM) satellites, both in a sun-synchronous orbit. Terra's orbit around the Earth is timed so that it passes from north to south across the equator in the morning (about 10:30 AM local time), while Aqua passes south to north over the equator in the afternoon (about 1:30 PM local time). MODIS views the entire Earth's surface every 1 to 2 days, acquiring data in 36 spectral bands. This project utilizes daily aerosol optical thickness (AOT, hereafter used interchangeably with AOD) retrieved from imagery captured by MODIS sensors on both platforms. The time period considered is August 2006. Since TERRA-MODIS acquires imagery during the morning (10:30 AM) and AQUA-MODIS in the afternoon (1:30 PM), combined aerosol fields retrieved from both Terra and Aqua MODIS imagery can create a more complete dataset for use in CMAQ. The rationale for combining the data are: (1) MODIS sensor takes approximately four hours to image the entire region covered by the Continental United States (CONUS), and it is not possible to obtain simultaneous aerosol observations; (2) Aerosol retrievals are not available when cloud cover is present; thus, combining aerosol retrievals from the two platforms, increase the probability of obtaining a successful retrieval at a given location. The latter is especially true in case of partly cloudy scenes and/or presence of short lived clouds.

Spatial resolution of MODIS level 2 aerosol product is 10 km by 10km at nadir, which is resampled to the 36km x 36km resolution equal area grid utilized by the CMAQ model. Note that the MODIS observed AOD, resampled to CMAQ grid, is utilized for initializing and providing lateral boundary conditions for CMAQ. In addition, this data is also used for comparing against the CMAQ-predicted aerosol fields. Since the MODIS AOD used in this project is a combination of observations from both Terra and Aqua platforms, it is compared against CMAQ simulated AOD averaged over a period (1500-2200 UTC) that is consistent with daytime observation window for Terra and Aqua platforms over CONUS region.

Even after combining aerosol fields from Terra and Aqua, one of the difficulties encountered in creating AOD fields was missing retrievals due to presence of clouds. In order to obtain a smoothed AOD field, a nearest neighbor resampling approach was devised. If a missing value of AOD is encountered in combined Terra-Aqua product (before resampling to CMAQ grid), a three pixel radius neighborhood is searched for a valid AOD observation. If valid observations are found, then the missing value is replaced by the average of neighboring pixels. Sensitivity of this process to the radius of the search neighborhood was studied and a three pixel radius was found to be adequate. **Table 1** shows the results for a case study in August 14, 2007. While going farther out from a missing pixel reduces the number of missing data, it also increases the uncertainty of the value that is assigned to the missing pixel.

The procedure fills in the majority of the missing data pixels in the region and creates a smooth AOD field. In order to examine the validity of the resampling procedure, the following experiment was conducted. Figure 8 illustrates another example of pixel extension algorithm

described above for September 7, 2006. From the original Terra-Aqua combined MODIS AOD image (**Figure 8a**), 50% of the non-zero AOD was randomly removed (
Figure 1**b**).

Then in successive attempts the coverage was extended by increasing the radius of search from 1-pixel to 3-pixels. The 1-pixel extension recovered 57% of the removed data, while 2- and 3-pixel extensions recovered 73% and 82% of the removed data respectively. The correlation coefficient between the recovered data and the original data remains relatively unchanged (.88) indicating that even going out by 3-pixels for the search does not increase the error in the recovered data significantly while it increases the number of recovered data considerably. Scatter plot between the original AOD values of the randomly removed pixels and the values obtained for the same locations after resampling procedure was applied to the modified field shows that majority of the points are clustered in along the one-to-one line. The same experiment was performed on the August 14, 2007, case and resulted in a correlation coefficient of .93 suggesting a good agreement between the original AOD field and the recovered data.

**Table 1. Percentage of Missing Pixels Within MM5 Area**

| | 08/01 | 08/02 | 08/03 |
|---|---|---|---|
| 2 pixels | 31.5% | 34% | 34% |
| 3 pixels | 18% | 20.7% | 21.8% |
| 4 pixels | 10% | 13% | 14% |

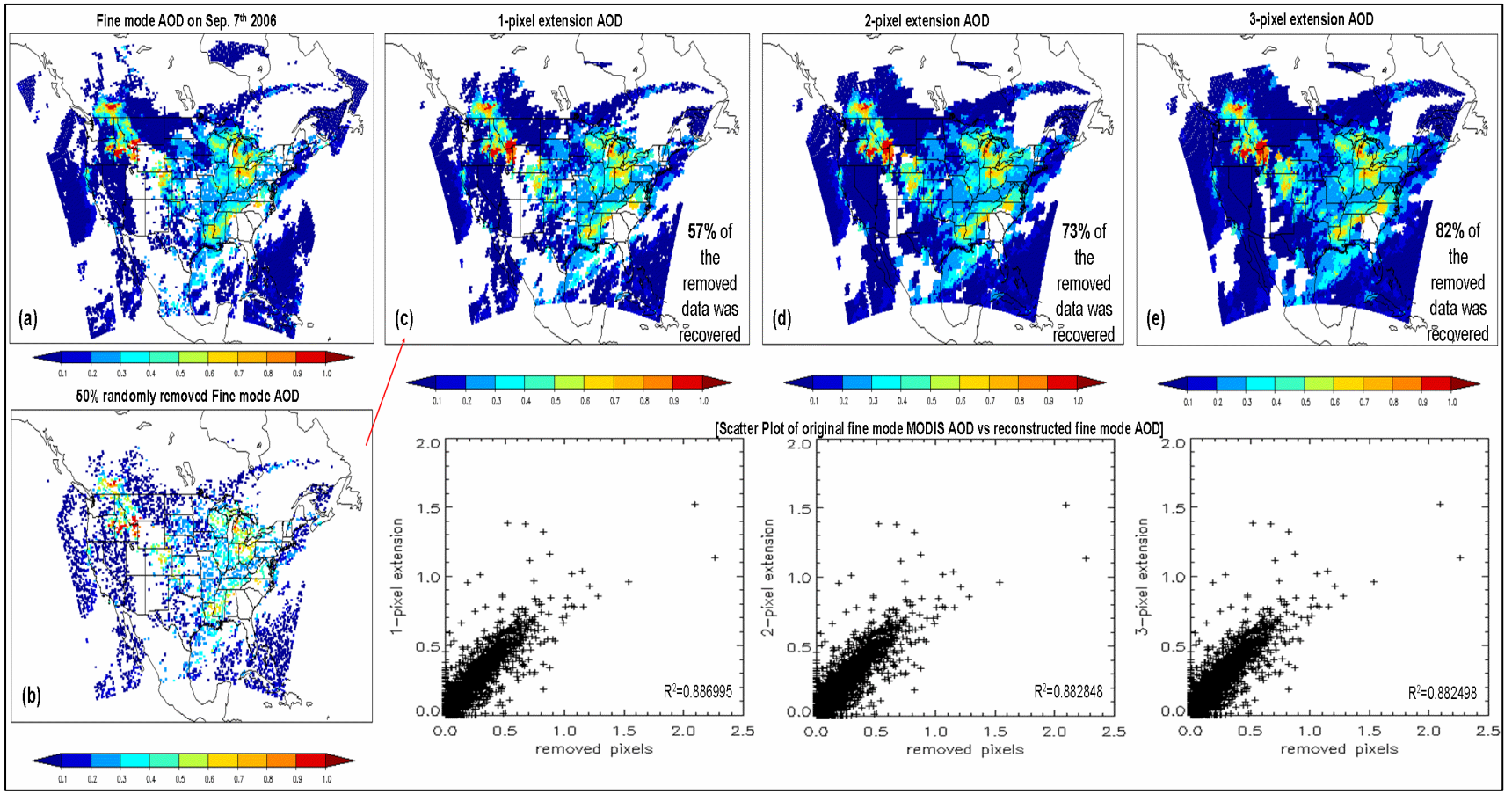


**Figure 8.** **Pixel extension algorithm (PEA) allows for increasing MODIS coverage by reconstructing missing values due to cloud contamination. (a) MODIS AOD from TERRA and AQUA on Sept. 7, 2006. (b) We randomly removed 50% pixels from original image (a). (c, d, e) Reconstructed image using 1, 2, and 3 pixel extension.**

#### *2.1.2.1. Utilization of MODIS AOD for Initialization and Specification of Lateral Boundary Conditions in CMAQ*

The combined Terra-Aqua AOD data was resampled to CMAQ domain and was utilized for initializing and also specifying the lateral boundary conditions in CMAQ. As noted previously, information regarding vertical distribution of aerosols is needed for effective use of MODIS AOD in the model. This information is obtained from CMAQ. The dependency of the technique to the information from the model implies that the aerosol module used has a decisive impact on the aerosol speciation and distribution. In this exercise we have used the standard aerosol module in CMAQ as described in Binkowski and Roselle (2003) with updates described in Bhave et al. (2004). The aerosol distribution is modeled as a superposition of three lognormal modes that nominally correspond to Aitken (particles with diameter < 0.1 μm), accumulation (particles with 0.1 < diameter < 2.5 μm), and coarse (particles with diameter > 2.5 μm) modes. In the current exercise we use two aerosol categories, fine and coarse modes. Fine mode consists of aerosols with aerodynamic diameter of less than 2.5 micro-meters ($PM_{2.5}$), while coarse mode consists of aerosols with diameter greater than 2.5 micro-meters. The model results for $PM_{2.5}$ concentrations are obtained by summing species concentrations over the Aitken and accumulation modes. CMAQ aerosol species (as represented in CMAQ aerosol module) are presented in **Table 2**. The fine mode aerosol species comprise sulfate, nitrate, ammonium, anthropogenic and biogenic organic carbon, elemental carbon, and other unspecified species originating from human activity.

**Table 2. Speciation and Variable Name Used in the CMAQ Aerosol Module**

| Species Description | Name |
|---|---|
| Aitken mode sulfate mass | ASO4I |
| Accumulation mode sulfate mass | ASO4J |
| Aitken mode ammonium mass | ANH4I |
| Accumulation mode ammonium mass | ANH4J |
| Aitken mode nitrate mass | ANO3I |
| Accumulation mode nitrate mass | ANO3J |
| Aitken mode anthropogenic secondary organic mass | AORGAI |
| Accumulation mode anthropogenic secondary organic mass | AORGAJ |
| Aitken mode primary organic mass | AORGPAI |
| Accumulation mode primary organic mass | AORGPAJ |
| Aitken mode secondary biogenic organic mass | AORGBI |
| Accumulation mode secondary biogenic organic mass | AORGBJ |
| Aitken mode elemental carbon mass | ACEI |
| Accumulation mode elemental carbon mass | ACEJ |
| Aitken mode unspecified anthropogenic mass | A25I |
| Accumulation mode unspecified anthropogenic mass | A25J |
| Aitken mode water mass | AH2OI |
| Accumulation mode water mass | AH2OJ |

MODIS level 2 data provides fine mode fraction, which is the fractional contribution of fine mode to total AOD. Fine mode fraction data is used in this project to separate out fine and coarse mode AOD. However, fractional contributions by the different aerosol species to fine and coarse mode aerosols and knowledge of vertical distribution is still needed to utilize MODIS

AOD. The following assumptions are made for closure: (1) The vertical distribution of different aerosol species is given by the CMAQ simulated profile for the corresponding time; (2) The percentage contribution of an aerosol species to the total particulate mass within a column is same as that obtained from CMAQ simulations for the corresponding time. Based on these assumptions the following ratio parameter (α) is used to scale the aerosol mass concentration in a CMAQ vertical column:

$$\alpha = \frac{\tau_{MODIS}}{\tau_{CMAQ}}$$

Where $\tau_{MODIS}$ and $\tau_{CMAQ}$ are MODIS and CMAQ aerosol optical depths (AOD) respectively. For the model $\tau_{CMAQ}$ can be calculated as:

$$\tau_{CMAQ} = \int_0^{Z_{top}} B_{ext}\, dz$$

Where $B_{ext}$ is the aerosol extinction coefficient ($km^{-1}$), and $Z$ is the height in km. To arrive at aerosol extinction coefficient we use an empirical relationship devised from long term measurements at the Interagency Monitoring of Protected Visual Environments (IMPROVE) sites (Hand and Malm, 2005), including the new revisions made based on the current information (http://vista.cira.colostate.edu/improve/Publications/GrayLit/019_RevisedIMPROVEeq/RevisedIMPROVEAlgorithm3.doc). The extinction coefficient is calculated as:

$$\begin{aligned}\beta_{ext} \approx\ & 2.2 \times f_S(rh) \times [Small\ Sulfate] + 4.8 \times f_L(rh) \times [Large\ Sulfate] \\ & + 2.4 \times f_S(rh) \times [Small\ Nitrate] + 5.1 \times f_L(rh) \times [Large\ Nitrate] \\ & + 2.8 \times [Small\ Organic\ Mass] + 6.1 \times [Large\ Organic\ Mass] \\ & + 10 \times [Elemental\ Carbon] + 1 \times [Fine\ Soil] + 1.7 \times f_{SS}(rh) \times [Sea\ Salt] \\ & + .6 \times [Coarse\ Mass] + 1 \times [Rayleigh\ Scattering\ (Site\ Specific)] + .33 \times [NO_2\ (ppb)]\end{aligned}$$

The algorithm uses three water growth adjustment terms. They are for use with the small size distribution (S) and the large size distribution (L) sulfate and nitrate compounds and for sea salt ($f_S(RH)$, $f_L(RH)$ and $f_{SS}(RH)$ respectively). Site-specific Rayleigh scattering is calculated for the elevation and annual average temperature of each of the IMPROVE monitoring sites.

Hourly modeled AOD is averaged to corresponding MODIS tracking time which is from 15 to 22 GMT to obtain the ratio α. In order to eliminate the site specific impact of Rayleigh scattering ($\int (Rayleigh\_scattering)dz$), the adjustment is only applied if the MODIS AOD ($\tau_{MODIS}$) is greater than Rayleigh scattering. Thus, when the impact of Rayleigh-scattering is greater than zero, the ratio is calculated as:

$$\alpha = \frac{\left\{\tau_{MODIS} - \int (Rayleigh\_scattering)dz\right\}}{\int (\beta_{ext} - Rayleigh\_scattering)dz}$$

If Rayleigh-scattering impact does not exist and MODIS data are available, then the ratio is simply expressed as:

$$ratio = \frac{\tau_{MODIS}}{\int \beta_{ext} dz}$$

For the time period considered in this study, the values of α is varied from $10^{-4}$ to 85, with majority of α values being less than 5. All 16 fine aerosol species in **Table 2** (I and J modes, except water) are scaled by α. Also note that while $NO_2$ is used in IMPROVE equation for calculating the aerosol extinction coefficient, it will not be scaled by α. Examples of scaled vertical profiles obtained using this procedure is shown in **Figure 9**. When the value of α is less than 1, it reduces the mass concentration throughout the vertical column, while values of α greater than 1 leads to an increase throughout the column. In cases where satellite-derived AOD is not available the scaling procedure is not applied and model concentrations are used.

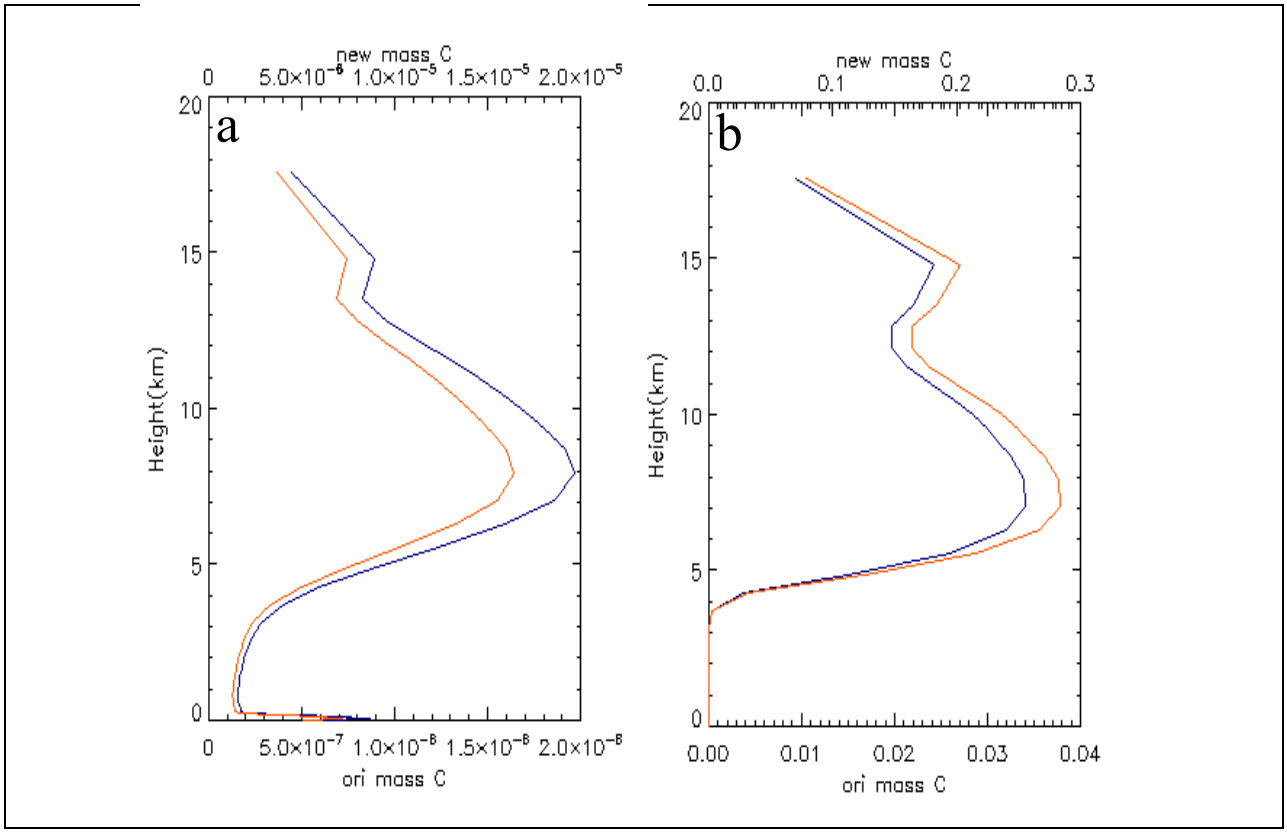


**Figure 9. Vertical profiles of CMAQ mass concentrations scaled using the scaling ratio α. (a) Black carbon and (b) anthropogenic organic mass. Blue and red lines are the original CMAQ and scaled concentrations, respectively. Note that α is less than 1.0 for the case shown in panel (a) and more than one for that shown panel (b).**

## 2.2. Ozonesonde Data

In this project we have selected August 2006 as the study period so that we can take advantage of INTEX (INtercontinental chemical Transport EXperiment) Ozonesonde Network Study (Thompson et al., 2007a, 2007b) 2006 campaign (IONS-06). The IONS-06 campaign provided ozonesonde profiles (http://croc.gsfc.nasa.gov/intexb/ions06.html) for validation of ozone observations by the Aura satellite instruments.

Tropospheric ozone varies significantly on time scales from months to hours. Our current routine ozonesonde measuring capabilities resolve tropospheric ozone variation at vertical resolution of 100m and temporal scales of usually 1 week, but occasionally 1 day or a minimum of 6 hours for short durations. Ozonesondes make in situ measurements of temperature, pressure, humidity and ozone from balloons launched from stations around the world. A typical ozonesonde measurement provides vertical profiles with a resolution of about 100 m, up to a maximum altitude of about 35 km (~7 mb). The accuracy of ozone measurements from sondes is often quoted as about ± 5% [Stratospheric Processes and their Role in Climate, International Ozone Commission, and Global Atmosphere Watch, 1998] and it depends on a number of factors. A variety of types of ozonesondes exist, but the most common type used in this work is the electrochemical concentration cell (ECC) sonde which relies on the oxidation reaction of ozone with a potassium iodide (KI) solution (Komhyr et al., 1995). ECC sondes are made by two different manufacturers and can operate with a range of KI solution strengths, buffer types and preparation procedures. Smit et al., 2007, evaluated sonde performance in a series of experiments using a small number of sonde measurements. Their work indicates a precision of better than ±(3 –5)% with an accuracy of about ±(5– 10)% up to 30-km altitude if standard operating procedures for ECC sondes are used. The study also suggests a median high bias of about 5% for ECC sondes relative to an ultraviolet (UV) photometer.

One of the main objectives of IONS-06 campaign was to validate TES observations; therefore, ozonesonde launches during the summer of 2006 were scheduled in such a way to maximize the number of concurrent measurements with Aura's overpasses. **Figure 10** Shows the location of ozonesonde launch sites in North America. In this study we use the data from a subset of these stations (18 stations) for our evaluation work. For August 2006, about 352 launches were made from these sites. Among them there are 24 profiles measured from NOAA *Ron Brown* ship over the Gulf of Mexico (referred as "*Ron Brown*" station). The locations of the vessel at the time of these launches are marked on the map in **Figure 11**. As seen in the figure, for most days the vessel is staying close to the coast or is sampling the Houston ship channel. Only on July 31, August 2 and 16 the ship is farther away from the shoreline and is sampling the air that is more representative of the background in GoM region.


**Figure 10. Ozonesonde locations for IONS-06 campaign. During IONS-06 daily ozonesondes were launched from these locations with an attempt for the launch time to coincide with Aura's overpass. In this study we have used the measurements from a subset of 18 stations within CONUS.**

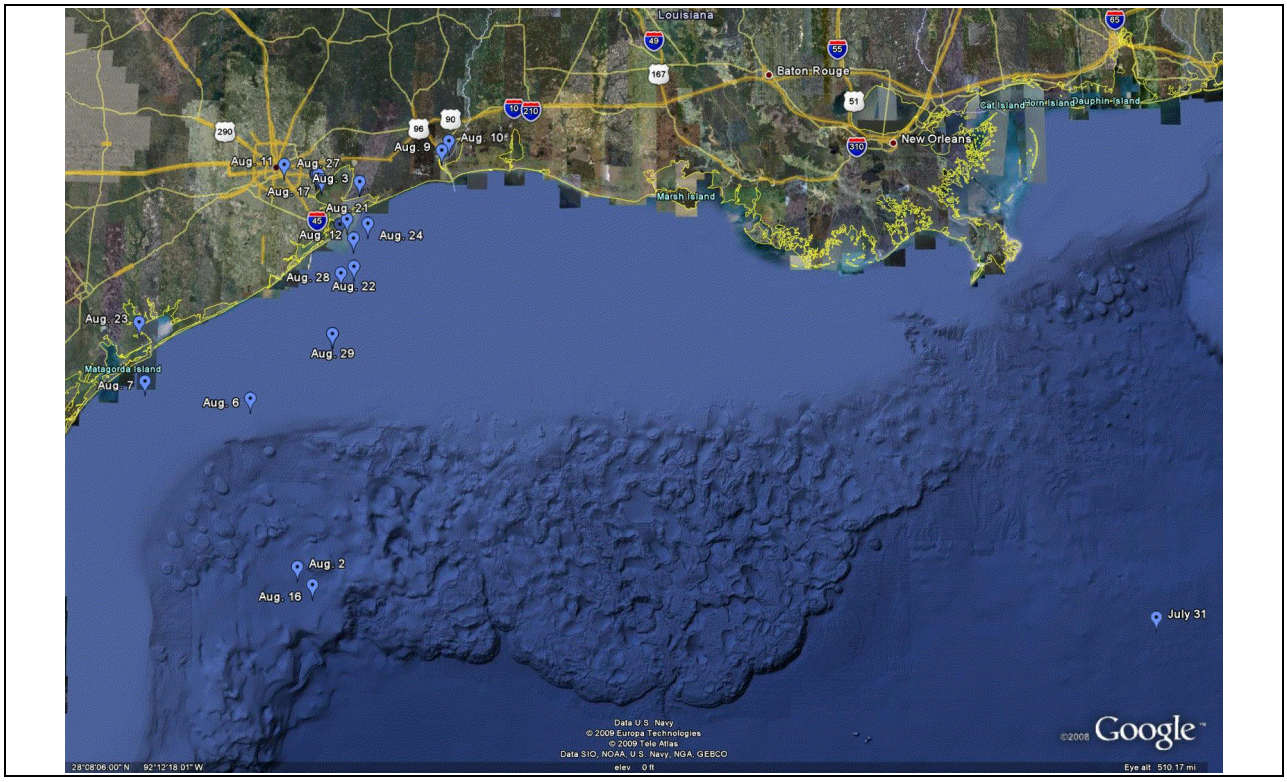


**Figure 11. Locations of NOAA *Ron Brown* vessel during August 2006. The ship participated in IONS-06 campaign and daily ozonesondes were launched from the locations marked on the map.**

## 2.3. Model Simulations

The modeling paradigm for this project is presented in **Figure 12**. The main components in this modeling exercise are meteorological modeling, emissions processing, and the photochemical modeling. MM5 is utilized to provide the meteorological fields necessary to drive CMAQ. Sparse Matrix Operator Kernel Emissions (SMOKE, http://www.smoke-model.org/index.cfm) was utilized for emissions processing. Since the objective of this study is to quantify the efficacy of satellite observations in the air quality assessment practices, it is necessary to have the best representation of the physical atmosphere as well as the best description of the emissions into the modeling domain. Thus, in our meteorological simulations we have strived to use all available analyses for our modeling episode. Also, in processing the emissions, emissions inventory were revisited and corrected several times as problems were discovered. All the sensitivity simulations were performed only after a complete and satisfactory evaluation of meteorology and emissions. In the following each of these modeling components and their configurations will be reviewed.

### 2.3.1. Meteorological Modeling

Modeling of atmospheric dynamics observed during the 90 day period (July 1 to September 30) in 2006 was conducted using the fifth-Generation Penn State/NCAR Mesoscale Model (MM5) (Dudhia, 1989; Grell *et al*., 1994). Maintained by the National Center for Atmospheric Research (NCAR), MM5 is in a series of Mesoscale models first developed at Penn State in the early 1970's (Anthes and Warner, 1978). Since that time, it has undergone many changes designed to broaden its usage. These include, (1) a multiple-nest capability; (2) non-hydrostatic dynamics that allow the model to be used at a few-kilometer scale; (3) multi-tasking capability on shared- and distributed-memory machines; (4) four-dimensional data-assimilation (FDDA) capability, and (5) multiple physics options. It has been extensively used in the development of meteorological fields for air quality modeling application.

Modeling simulations were conducted on a 36-km resolution grid that spans over the continental U.S. A Lambert Conformal map projection with origin at 40N and 97W and true latitudes at 33 and 45N were employed. The grid has 164 cells in the east-west and 128 cells in the north-south direction. The top of the modeling grid has been fixed at 50mb. It has 39 vertical layers of varying thickness. To avoid artificial numerical mixing near the top of the model, vertical layers are adjusted near tropopause by increasing the number of layers in the upper troposphere/lower stratosphere. This would be important as the ozone vertical gradient is the highest at the tropopause. **Figure 13** exhibits the horizontal extent of the modeling domain.

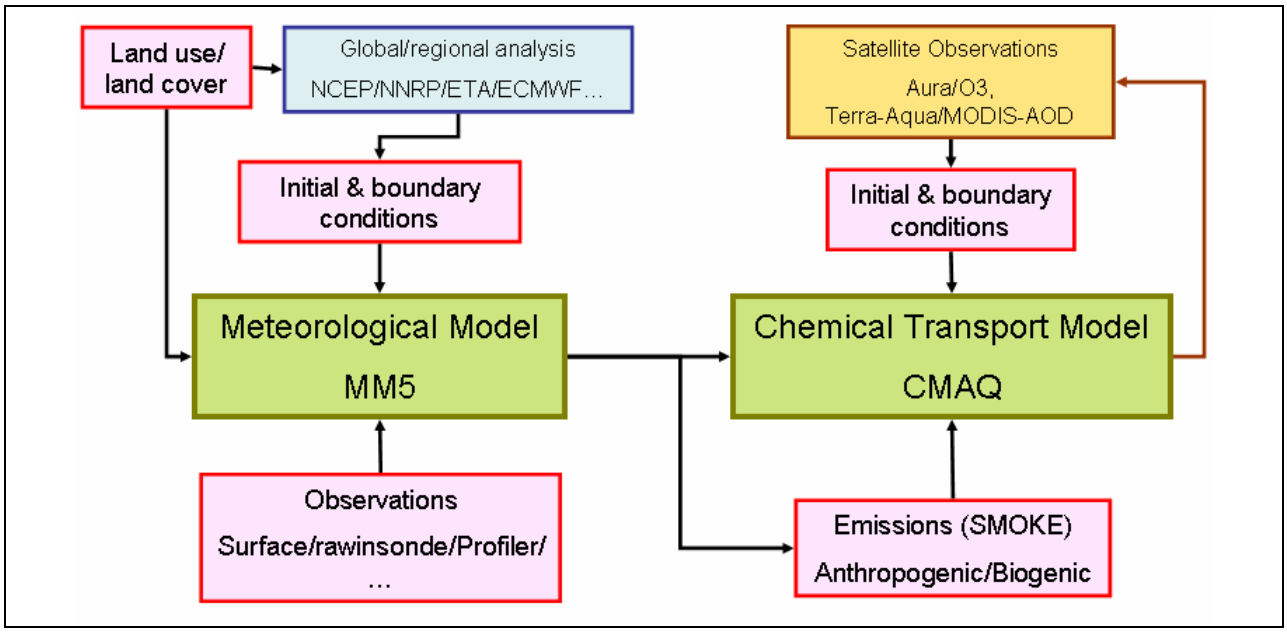


**Figure 12. Flow chart illustrating the model components. The main components are Meteorological model (MM5), emissions processor (SMOKE), and the chemical transport model (CMAQ). Satellite observations of ozone and AOD were assimilated through initial and boundary conditions in CMAQ.**

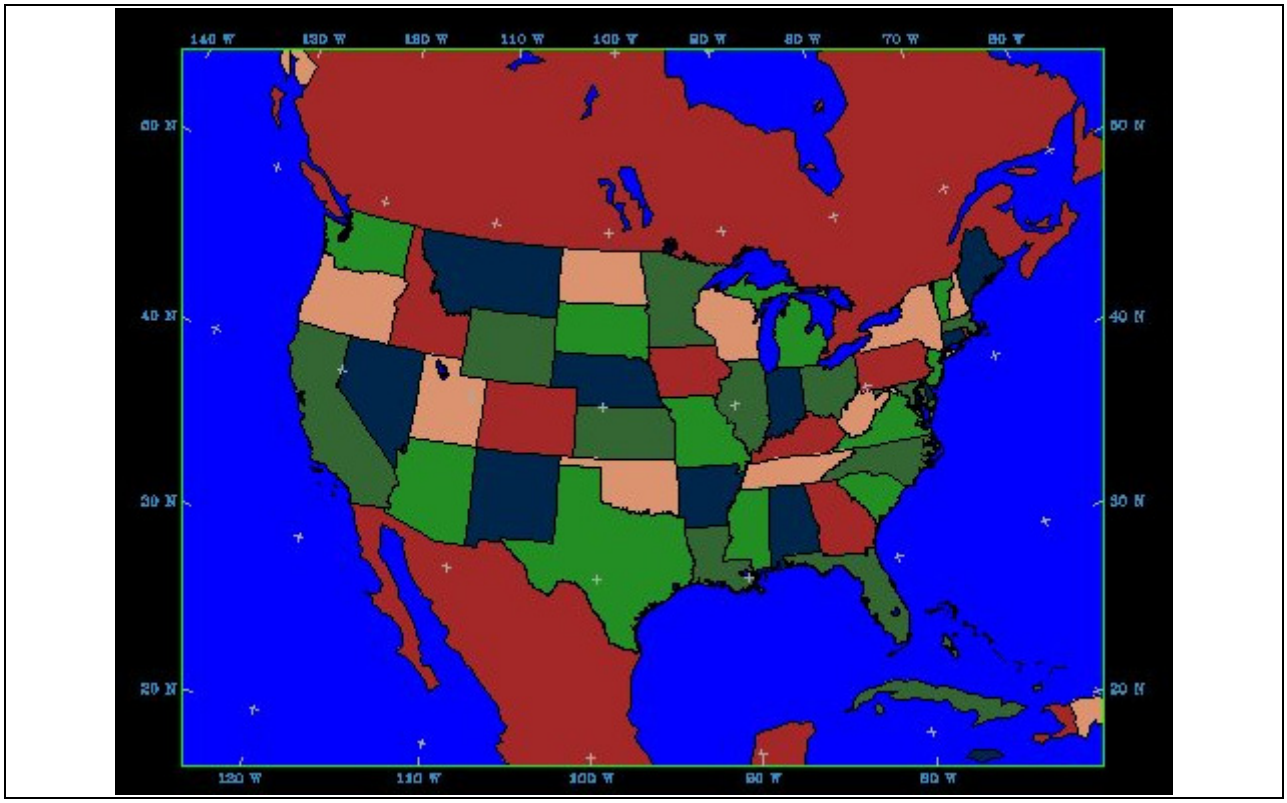

**Figure 13. 36-km modeling grid.**

Like any other prognostic meteorological model, MM5 requires a significant amount of terrestrial (i.e., topography, Land Use/Land cover) and atmospheric data (e.g., gridded analyses fields that include at a minimum sea-level pressure, wind, temperature, relative humidity, and observations that contain soundings and surface reports). In this modeling project surface elevation, Land Use/Land Cover (LULC), soil type, and other terrestrial datasets from United States Geological Survey (USGS); NCEP ETA gridded analysis data at 40-km resolution archived at 3-hour intervals available at http://dss.ucar.edu/datasets/ds609.2; surface (land and ship) and upper air observational data archived at 3 and 6-hour intervals available at http://dss.ucar.edu/datasets/ds464.0; and hourly surface observations for over 1,000 stations in U.S. and Canada available at http://dss.ucar.edu/datasets/ds472.0 were utilized.

Modeling simulations were conducted using MM5 version 3.7. Data processing was performed in six day segments beginning July 1 and ending October 3. The NCEP Eta-based 4-D Data Assimilation System (EDAS) analyses were utilized for these simulations (Eta is one of NCEP's mesoscale numerical weather prediction models and the name "Eta" derives from the model's vertical coordinate known as the "eta" or "step-mountain" coordinate). The NCEP ETA gridded analyses data was first processed through the program PREGRID and mapped onto the 36-km domain via the REGRIDDER. Surface, ship and upper air data are incorporated within the analyses fields with the help of the program LITTLE_R. Finally, INTERPF is used to interpolate pressure level fields generated by LITTLE_R onto MM5 sigma coordinates.

MM5 model configuration, presented in **Table 3**, was determined through a brief literature review (Brewer *et al.*, 2007; Kemball-Cook et al., 2005) of recent modeling projects that have been undertaken in support of air quality management activities.

The model performance was evaluated using software known as METSTAT developed by ENVIRON corporation (http://www.camx.com/files/metstat.15feb05.tar.gz). It computes surface statistics for temperature, wind speed and direction, and humidity. The metrics include: Bias Error (B), Gross Error (E) and Root Mean Square Error (RMSE), Systematic Root Mean Square Error ($RMSE_s$), Unsystematic Root Mean Square Error ($RMSE_u$) and Index Of Agreement (IOA). Mathematical formulation of these variables is provided in **Table 4**. Monthly average performance statistics for August 2006 are provided in **Table 5**. In an effort to identify model biases and error over different regions of the domain, statistics have been computed for sub-regions shown in **Figure 14** and the results presented in **Table 6**.

While reviewing these statistics, one should be cautioned that summary statistics are useful in making only a general assessment about the adequacy of meteorological fields. For example, daily-mean performance statistics are likely to conceal important hour-to-hour variations. Also, summary statistics depend upon the number of observation-prediction pairs and generally improve with larger sampling sizes and longer averaging periods. This is because the probability of statistics being affected by extreme events (outliers) is high in smaller sample sizes. These and other concerns have lead USEPA to recommend that benchmarks proposed in Emery *et al.*, (2001) should not be used in a “pass/fail” model, but only as a means of assessing general confidence in meteorological model output.

**Table 3. MM5 Model Configuration.**

| Physics Options | Option Used in the Simulation |
|---|---|
| Nesting Type | One-way |
| Numerical Time Step | 90 sec |
| Cumulus parameterization | Grell |
| PBL scheme | MRF |
| Microphysics | Reisner 1 |
| Radiation scheme | RRTM scheme |
| Land Surface scheme | Noah-LSM |
| Convection scheme | KF2 |
| Observation nudging | None |
| 3-D Grid analysis nudging | Yes |
| 3-D Grid analysis nudging time interval | 3-hour |
| 3-D Grid analysis nudging co-efficient | GU=2.5x10$^{-4}$, GV=2.5x10$^{-4}$, GT=2.5x10$^{-4}$, GQ=1.0x10$^{-5}$ |
| Surface Analysis nudging | Yes |
| Surface Analysis nudging time interval | 3-hour |
| Surface Analysis nudging co-efficient | GU=2.5x10$^{-4}$, GV=2.5x10$^{-4}$ |

**Table 4. Mathematical Formulation of Statistical Metrics Used for Evaluating Mesoscale Meteorological Model Performance.**

| Metrics | Formulation |
|---|---|
| Bias | $B = \frac{1}{IJ}\sum_{j=1}^{J}\sum_{i=1}^{I}\left(P_j^i - O_j^i\right)$ |
| Gross Error | $E = \frac{1}{IJ}\sum_{j=1}^{J}\sum_{i=1}^{I}\left\|P_j^i - O_j^i\right\|$ |
| Root Mean Square Error | $RMSE = \left[\frac{1}{IJ}\sum_{j=1}^{J}\sum_{i=1}^{I}\left(P_j^i - O_j^i\right)^2\right]^{1/2}$ |
| Systematic Root Mean Square Error | $RMSE_S = \left[\frac{1}{IJ}\sum_{j=1}^{J}\sum_{i=1}^{I}\left(\hat{P}_j^i - O_j^i\right)^2\right]^{1/2}$ |
| Unsystematic Root Mean Square Error | $RMSE_u = \left[\frac{1}{IJ}\sum_{j=1}^{J}\sum_{i=1}^{I}\left(P_j^i - \hat{P}_j^i\right)^2\right]^{1/2}$ |
| Index of Agreement | $IOA = 1 - \left[\frac{IJ.RMSE^2}{\sum_{j=1}^{J}\sum_{i=1}^{I}\left\|P_j^i - M_o\right\| + \left\|O_j^i - M_o\right\|}\right]$ |

**Table 5. Performance Statistics for Mesoscale Meteorological Models.**

| Statistical Measure | Benchmark |
|---|---|
| Wind Speed Bias (m/s) | <±0.5 |
| Wind Speed Total RMSE (m/s) | 2.0 |
| Wind Speed Index of Agreement | 0.6 |
| Wind Direction Gross Error (degree) | 30.0 |
| Wind Direction Bias (degree) | <±10.0 |
| Temperature Bias (Kelvin) | <±0.5 |
| Temperature Gross Error (degree) | 2.0 |
| Temperature Index of Agreement | 0.8 |
| Humidity Bias (g/kg) | <±1.0 |
| Humidity Gross Error (g/kg) | 2.0 |
| Humidity Index of Agreement | 0.6 |

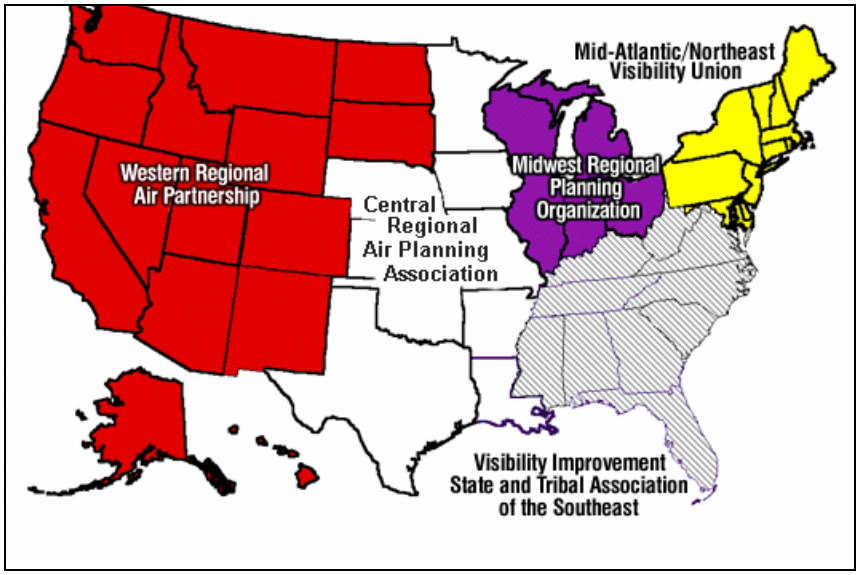


**Figure 14. Subregions used in performance evaluation.**

**Table 6. Monthly Meteorological Performance Statistics for Each of the SubRegions in Figure 14.**

| Meteorological Variable | | | CENRAP | MANEVU | MWRPO | VISTAS | WRAP |
|---|---|---|---|---|---|---|---|
| Wind Speed | Mean OBS | (m/s) | 2.97 | 2.70 | 2.49 | 2.05 | 3.24 |
| Wind Speed | Mean PRD | (m/s) | 2.47 | 2.35 | 2.41 | 1.94 | 2.43 |
| Wind Speed | Bias | (m/s) | -0.50 | -0.35 | -0.09 | -0.11 | -0.81 |
| Wind Speed | Gross Error | (m/s) | 1.26 | 1.48 | 1.17 | 1.21 | 1.64 |
| Wind Speed | RMSE | (m/s) | 1.65 | 2.03 | 1.50 | 1.54 | 2.11 |
| Wind Speed | Sys RMSE | (m/s) | 1.35 | 1.67 | 1.14 | 1.24 | 1.81 |
| Wind Speed | Unsys RMSE | (m/s) | 0.94 | 1.13 | 0.97 | 0.91 | 1.09 |
| Wind Speed | IOA | | 0.73 | 0.59 | 0.70 | 0.68 | 0.66 |
| Wind Direction | Mean OBS | (deg) | 149.90 | 189.95 | 167.60 | 160.32 | 255.55 |
| Wind Direction | Mean PRD | (deg) | 151.30 | 203.67 | 171.11 | 164.80 | 246.42 |
| Wind Direction | Bias | (deg) | 2.77 | 4.91 | 4.53 | 4.84 | 6.16 |
| Wind Direction | Gross Error | (deg) | 25.72 | 27.81 | 24.58 | 33.14 | 43.26 |
| Temperature | Mean OBS | (K) | 298.38 | 294.37 | 294.96 | 299.75 | 294.38 |
| Temperature | Mean PRD | (K) | 298.61 | 293.58 | 294.47 | 300.10 | 294.01 |
| Temperature | Bias | (K) | 0.23 | -0.79 | -0.50 | 0.35 | -0.38 |
| Temperature | Gross Error | (K) | 2.08 | 2.09 | 2.08 | 2.11 | 2.99 |
| Temperature | RMSE | (K) | 2.81 | 2.70 | 2.68 | 2.85 | 3.87 |
| Temperature | Sys RMSE | (K) | 1.02 | 0.85 | 0.82 | 0.99 | 0.54 |
| Temperature | Unsys RMSE | (K) | 2.60 | 2.53 | 2.53 | 2.66 | 3.82 |
| Temperature | IOA | | 0.95 | 0.92 | 0.91 | 0.90 | 0.93 |
| Humdity | Mean OBS | (g/kg) | 14.38 | 11.54 | 12.71 | 16.37 | 8.13 |
| Humdity | Mean PRD | (g/kg) | 13.24 | 11.21 | 11.91 | 15.23 | 7.21 |
| Humdity | Bias | (g/kg) | -1.13 | -0.33 | -0.81 | -1.14 | -0.92 |
| Humdity | Gross Error | (g/kg) | 1.64 | 1.12 | 1.42 | 1.71 | 1.53 |
| Humdity | RMSE | (g/kg) | 2.08 | 1.44 | 1.77 | 2.17 | 2.03 |
| Humdity | Sys RMSE | (g/kg) | 1.23 | 0.69 | 1.10 | 1.28 | 1.32 |
| Humdity | Unsys RMSE | (g/kg) | 1.64 | 1.23 | 1.35 | 1.73 | 1.53 |
| Humdity | IOA | | 0.86 | 0.84 | 0.79 | 0.76 | 0.86 |

In order to examine the overall model performance with respect to realization of weather patterns, we also made comparisons with weather charts for the period of July 15 through September 6. Generally, the model performed reasonably well with respect to the predictions of surface temperature and winds. In the following a few examples for selected cases of interest will be presented.

The general weather pattern for July 15 was similar to July 28. This was important as we intend to recycle CMAQ results in order to start the model simulation with a reasonable initial condition. To do this, we needed to run CMAQ (starting on July 15, with the standard IC) until a weather pattern similar to July 15 is reached. This would allow for the emissions to build-up over the domain of study and the atmospheric chemical composition in the model to be more representative of the real atmosphere.

**Figure 15** shows the weather charts for July 15 and July 28, alongside MM5 results for these days. As illustrated in the figure, the general wind pattern over the domain shows a reasonable agreement between the model and observations for these days. The overall temperature patterns

are also in reasonable agreement. August 21-23 mark the stationary front experiment over Dallas Fort Worth, Texas. During this period a lingering stationary front extended through north Texas, through the southeast to the east coast. The stationary front was associated with high ozone events and sporadic cloudiness in the region. **Figure 16** shows the weather charts for August 21-22 against model results for these days. Again model has been able to simulate this large scale event reasonably well as it captures the surface temperature gradient and low winds to the north and south of the front.

The statistics together with weather chart comparisons demonstrate that the meteorological fields being used in emissions processing and air quality modeling are a reasonable representation of the physical atmosphere for the period of interest. The errors in the wind speed and direction, however, will be affecting our sensitivity simulations as it impacts the transport of observed satellite trace gas and particulate matter that we impose on the model.

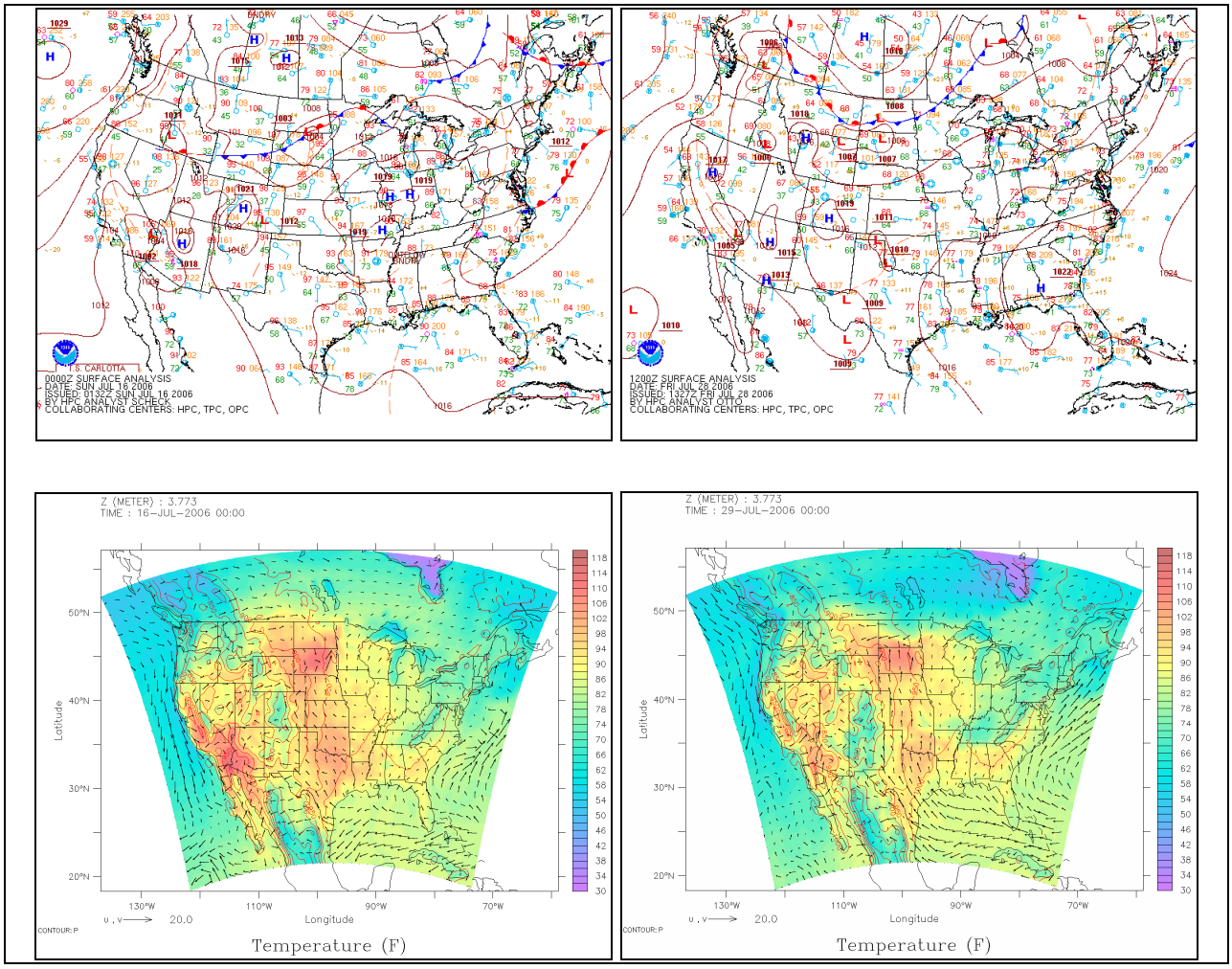


**Figure 15. Weather charts versus MM5 results for July 15 and 28.**

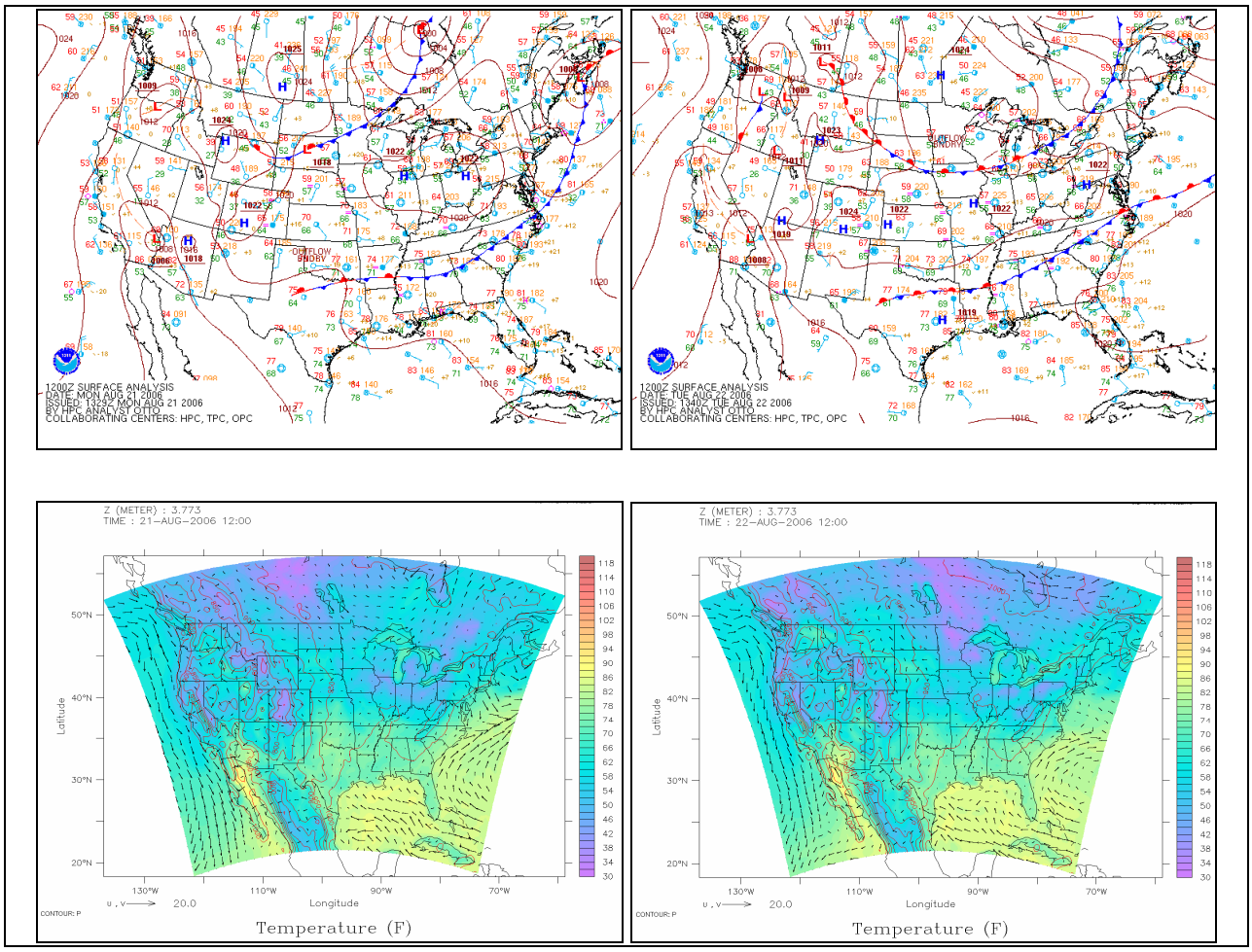


**Figure 16. Weather charts versus MM5 results for August 21 and 22.**

## 2.3.2. Emissions Processing

Emission inventories are typically available with an annual or daily total emissions value for individual emissions sources or source categories. Since air quality models require emissions data on an hourly basis, for each model grid cell and species, emission processors are needed to convert the available emissions data into a form that the air quality model can ingest. The Sparse Matrix Operator Kernel Emissions (SMOKE) processor (Coats, 1996; Houyoux *et al.*, 2000) is one such tool, and was used for creating gridded, temporalized and speciated emission files for this project. SMOKE is capable of generating temperature sensitive mobile source emission factors using EPA's MOBILE6 emission factors model. It is also capable of generating biogenic emissions for this research work with the help of Biogenic Emissions Inventory System (BEIS) version 3.09 (Guenther *et al.*, 2000; Pierce *et al.*, 1998). In addition to large amounts of source-specific data, certain aspects of emissions processing require meteorological variables. These are provided by the MM5 meteorological model and include daily surface temperature for calculating mobile source emission factors; temperature and radiation fields for calculating

biogenic emissions; and Planetary Boundary Layer (PBL) height, surface heat flux, wind speed, and temperature for estimating plume rise for point sources.

In the absence of any consolidated annual emissions inventory for 2006, we are using the 2002 annual emission inventory developed by Regional Planning Organizations (RPOs) in response to regulatory requirements established under the Regional Haze Rule (RHR). We are accounting for on-road mobile source emissions reductions that will likely result due to fleet turnover. We are also using the 2006 Continuous Emissions Monitoring (CEM) data for Electricity Generating Units (EGUs) compiled by EPA's Clean Air Markets Division (CAMD). Given the overall uncertainty in emission estimates, accounting for emission reduction in two major source categories will provide us with a reasonable estimate of emissions for this research work. SMOKE derived daily average emission totals and spatial plots of $NO_x$, VOC, CO, $SO_2$, $NH_3$, anthropogenic (AVOC) and isoprene are provided in **Table 7** and **Figure 17**.

**Table 7. Domain-wide Daily Emission Totals in Tons per Day.**

| Emission Source | $NO_x$ | VOC | Carbon | $SO_2$ | $NH_3$ | CO |
|---|---|---|---|---|---|---|
| Area | 3308.18 | 12604.77 | 1212.27 | 2550.13 | 6933.41 | 12066.45 |
| EGU | 10387.81 | 147.68 | 78.99 | 30651.54 | 46.21 | 2095.20 |
| Mobile | 14935.43 | 8801.20 | 214.07 | 329.87 | 0.00 | 99360.72 |
| Non-EGU | 12904.17 | 3100.11 | 347.01 | 18215.97 | 633.57 | 10320.65 |
| Non-Road | 12242.84 | 9819.18 | 919.69 | 1248.35 | 12.38 | 87420.60 |

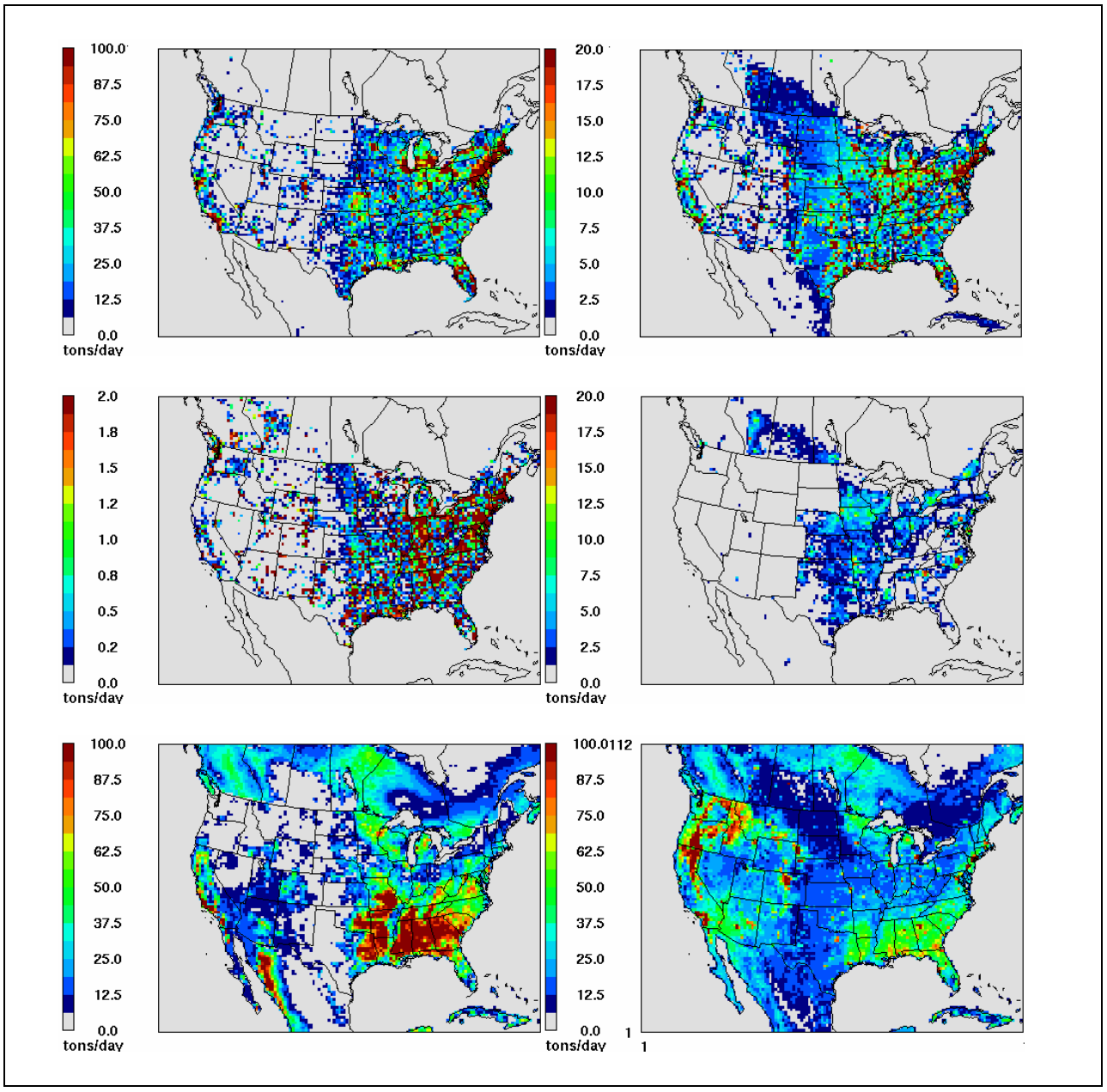


**Figure 17. Daily emissions totals (tons per day) for CO, $NO_x$, $SO_2$, $NH_3$, Isoprene, and anthropogenic VOC.**

### 2.3.3. Photochemical Modeling

Air quality modeling simulations were conducted using EPA's Community Multiscale Air Quality Chemistry Transport Model (CMAQ-CTM) or Models-3 (EPA, 1999; Dennis et al., 1996; Byun and Schere, 2006). The modeling system contains state-of-the-science parameterization of atmospheric processes affecting transport, transformation, and deposition of such pollutants as ozone, particulate matter, airborne toxics, and acidic and nutrient pollutant species. CMAQ-CTM incorporates output fields from the meteorological (e.g., MM5) and

emissions (e.g., SMOKE) modeling systems and several other data sources through special processors. The meteorological data is processed using Meteorology Chemistry Interface Processor (MCIP), initial and boundary conditions through ICON and BCON and clear sky photolysis rate using JPROC (Otte et al., 2004, 2005). Initial and boundary condition processors allow the use of a gridded concentration field as well as the species concentration profiles that are available with the installation. JPROC generates the photolysis rate lookup table under clear sky conditions.

MCIP version 3.3 was used to create meteorological input files for CMAQ-CTM. Most meteorological variables are passed through directly from the MM5 output fields. Others, such as dry deposition velocities, were computed by MCIP. Initial and boundary conditions for the 36-km domain are generated from a set of predefined vertical profiles available with the CMAQ software. The photolysis rates processor JPROC was used to generate clear sky photolysis rates. The processing is similar to that of the Regional Acid Deposition Model (RADM) (Chang et al., 1987, 1990) which uses modified extraterrestrial radiation data from the World Meteorological Organization (WMO) and $O_2$ and $O_3$ absorption cross-section data from NASA (DeMore et al., 1994). CMAQ provides several scientific options for the most important atmospheric processes (e.g., gas-phase chemistry, advection). The configuration used in this project is listed in **Table 8**. This configuration is based on our past modeling practices and is similar to commonly used configuration in regulatory applications.

**Table 8. CMAQ Configuration Used in Simulations for This Project.**

.

| Physical Process | Reference |
|---|---|
| Horizontal and vertical advection | YAMO |
| Horizontal diffusion | MULTISCALE |
| Vertical diffusion | ACM2 |
| Gas-phase chemistry and solver | EBI_CB4 |
| Gas and aqueous phase mechanism | CB4_AE3_AQ |
| Aerosol chemistry | AERO3 |
| Dry deposition | AERO_DEPV2 |
| Cloud dynamics | CLOUD_ACM |

The main objective of this project is to investigate the impact of initial and boundary conditions (IC/BC) on model predictions of ozone and to examine the usefulness of satellite observations in providing such critical information. Thus, a series of simulations were devised to achieve these objectives. Since these sensitivity simulations entirely depend on model input data, model configuration listed in **Table 8** remains unchanged throughout these simulations. The results from four simulations will be discussed in this report. These are (1) control simulation in which CMAQ is initialized only once at the beginning of the simulation and continuously runs for the entire simulation period using the standard boundary condition (CNTRL); (2) A simulation similar to the control but a continuous BC is constructed from Real-time Air Quality Modeling System (RAQMS) global model (RAQMS_BC); (3) A simulation similar to control except that BC was constructed by merging satellite observations and model

fields (SAT_BC); (4) A simulation similar to SAT_BC but re-initializing the model every 24 hours by assimilating satellite observations into the model fields (SAT_ICBC). The details about each simulation is explained in the following.

#### *2.3.3.1. Control Simulation (Base Case, CNTRL Simulation)*

To establish a base case scenario as a reference point in evaluating the model performance, a simulation was performed using CMAQ in its standard configuration and utilizing the default approach for providing boundary condition (BC). The default approach constructs a vertical profile of key atmospheric tracers for the lateral boundaries of the study domain based on climatology. The default BC is particularly unrealistic in the mid/upper troposphere as it provides low ozone concentrations for altitudes that are exposed to stratospheric ozone incursion and may experience much higher ozone concentrations.

The standard application of CMAQ, also constructs an initial condition (IC) that reflects clean atmosphere. While this approach works for long simulations, it is problematic for short term predictions. It will take the model several days to realize the impact of emissions within the modeling domain. The emissions will accumulate in the boundary layer while undergoing transport and transformation. The accumulated emissions and secondary products will be transported throughout the modeling domain and into the free troposphere by weather systems. The weather fronts that usually move from west to east over United States tend to push away the accumulated pollution and create a cleaner atmosphere behind the front. These processes create a non-homogeneous atmosphere that is very different from the homogeneous clean background atmosphere that the standard application of CMAQ provides as IC.

To make the control simulation more realistic, we first run the model (with clean atmosphere IC) for several days until a comparable weather pattern is observed over the modeling domain (continental U.S. in this case). The concentration field at the end of such simulation then is used as the initial condition for the long simulation. This allows for the realization of the impact of emissions and provides a more realistic atmosphere for model initialization. It greatly impacts the short term model predictions. In the current exercise we allowed a 13 day spin-up time. The model was started on July 15, 2006, at 0 GMT and was continuously run through July 28. The results from July 28 were recycled as the initial condition on July 15 in all subsequent simulations including the control simulation.

#### *2.3.3.2. Boundary Condition Provided by Global Model (RAQMS_BC Simulation)*

Another approach for providing IC and BC for CMAQ simulations would be the use of a global model that extends far beyond the regional modeling domain and potentially can realize the impact of long range transport and recirculation outside the regional boundary. To establish a secondary reference point for evaluating the impact of direct use of satellite observations in this project, we constructed a continuous BC record from RAQMS global model predictions. Our collaborator in this project, Dr. Daewon Byun (formerly at University of Houston and currently with NOAA/ARL) provided the BCs for these simulations (Song et al., 2008).

RAQMS data at 2 degree by 2 degree resolution were produced through the data assimilation of OMI ozone column with NOAA GFS Global meteorology and the satellite fire detection data from MODIS Rapid Response System (http://rapidfire.sci.gsfc.nasa.gov/). The details on model configuration and emissions data used for the RAQMS simulations are summarized in Al-Saadi et al. (2008). It used emissions of CO, $NO_x$, and hydrocarbons estimated from the gridded carbon fuel consumption databases, satellite fire detections, and meteorology-based estimates of fire weather severity to estimate the amount of carbon released from active fires and ecosystem-dependent emission ratios.

Since previous spin-up simulations were used as the CMAQ IC inputs, no special IC files for CMAQ simulations were prepared from RAQMS outputs. To construct the BC files, RAQMS2CMAQ conversion code developed at the University of Houston, Institute for Multidimensional Air Quality Studies (IMAQS) was used. The code was initially developed to process RAQMS data for the 1999 simulations. The original code used for the 1999 RAQMS data processing required daily METCRO3D files for providing the pressure height information used in the vertical interpolation. But for this project we utilized a reference pressure-height coordinate instead. Additionally, since the recent version of MCIP did not provide all the necessary inputs for the conversion code, the code was modified to accommodate the limited information. A one-day BC file from control simulation was used to set up exactly the same species list in the BC file. The results of the new code were verified with those from the original code for one day. The interpolation with the fixed pressure levels may potentially be less precise than the dynamic pressure levels provided by MM5. On the other hand, interpolating with the fixed pressure levels may be more robust than utilizing the MM5 pressure levels, which are affected by the synoptic and local scale pressure perturbations.

After the code modification was completed, a BC file was produced and verified. The results were compared with the University of Houston's 23 layer MM5 simulation case. Surprisingly, the ozone concentrations at the top level ($39^{th}$ layer) for the current case was substantially lower than those from the UH's top level ($23^{rd}$ layer) ozone. This could be due to the vertical resolution of the current model configuration in which the top layer is too thick to represent the stratospheric-tropospheric exchange processes. In the current model configuration the top layer is very thick in order to have high vertical resolution around 10 km altitude. This has been done in order to minimize the artificial numerical mixing of high stratospheric ozone into the upper troposphere (through numerical diffusion).

#### *2.3.3.3. Initial and Boundary Condition Provided from Satellite Observations (SAT_BC and SAT_ICBC Simulations)*

The final sets of simulations are designed to investigate the efficacy of using satellite observations of ozone and aerosols to provide IC and BC for regional air quality simulations. It comprises two sets of simulations. The first sets of simulations, called SAT_BC, are similar to control except for the BC data they use. In SAT_BC simulations, OMI ozone profiles and MODIS AOD are merged with model predictions to construct daily BC files. The simulations are performed in 24 hour segments, starting at 0 Greenwich Mean Time (GMT), but they are continuous as each new segment is initialized with the output from the previous segment. In

SAT_ICBC simulations, both BC and IC for each segment is provided by merging the satellite data with model predictions.

In preparing BC for these simulations satellite observations for the current day are used in conjunction with the current day simulation. This is necessary due to the time offset between the observations and the model predictions. A complete spatial coverage over continental U.S. (CONUS) from the satellite observation is obtained by combining the data from all the tracks within a day which span over several hours, while representing the same local time (about 1:30 PM) for any location. Furthermore, we are assuming that this single measurement can explain ozone and aerosol burden at lateral boundaries for a 24 hour simulation. Since each segment starts at 0:00 GMT, the current day observations would be a better representation of the air outside the boundary. It should be noted however that this technique is only applicable to retrospective modeling, such as regulatory air quality applications, where the observations for the simulation day are available.

BC only impacts the interior of the domain if the flow field is transporting air from outside the domain into the interior. Thus, the technique used in these simulations is not adequate for the situations where there is an observed transient event at the boundary in conjunction with a strong flow field toward the domain. Since a constant BC is applied for a 24-hour segment, such an event can exaggerate the impact of transboundary transport. This shortcoming will be addressed in future refinements to our technique as we plan to introduce diurnal variation for BC by projecting the observations outside the boundary to arrive at the boundary conditions for each given time.

In preparing IC files, satellite observations from the previous day are being utilized as they are closer to the model initialization time of 0:00 GMT. The techniques used for creating IC were described in Section 2.1. BC is simply constructed by extracting concentrations from IC files at model grids that reside at the boundary.

**Figures 18-23** show the BC plots for ozone ($O_3$), peroxy acetyl nitrate (PAN), formaldehyde (HCHO), nitrogen oxides ($NO_x$), carbon monoxide (CO) and sulfate aerosol for south, east, north and western boundaries for August 1, 2006. In each panel BC for control, RAQMS_BC, SAT_BC and SAT_ICBC are represented. The boundary conditions for SAT_BC and SAT_ICBC are identical due to the technique applied for these cases. They are presented for completeness and to emphasize the similarity. In **Figure 18** one can observe that both RAQMS_BC and SAT_BC ozone concentrations are significantly different from the control. Also, both the satellite observation and RAQMS are generally in agreement while OMI profiles indicate more stratospheric $O_3$ incursion into the mid-troposphere. Also of interest is the disagreement between the two in the western boundary where RAQMS indicate elevated $O_3$ concentration in mid-troposphere that is missing in the satellite observations. The figures also point to another limitation for the satellite data within the daytime boundary layer (below 1-km). The sharp vertical gradient around 1-km is due to the fact that when OMI data is not available we revert back to the model value. Thus, the sharp gradient is demonstrating the contrast between higher OMI concentrations above 1-km and lower model values below this elevation.

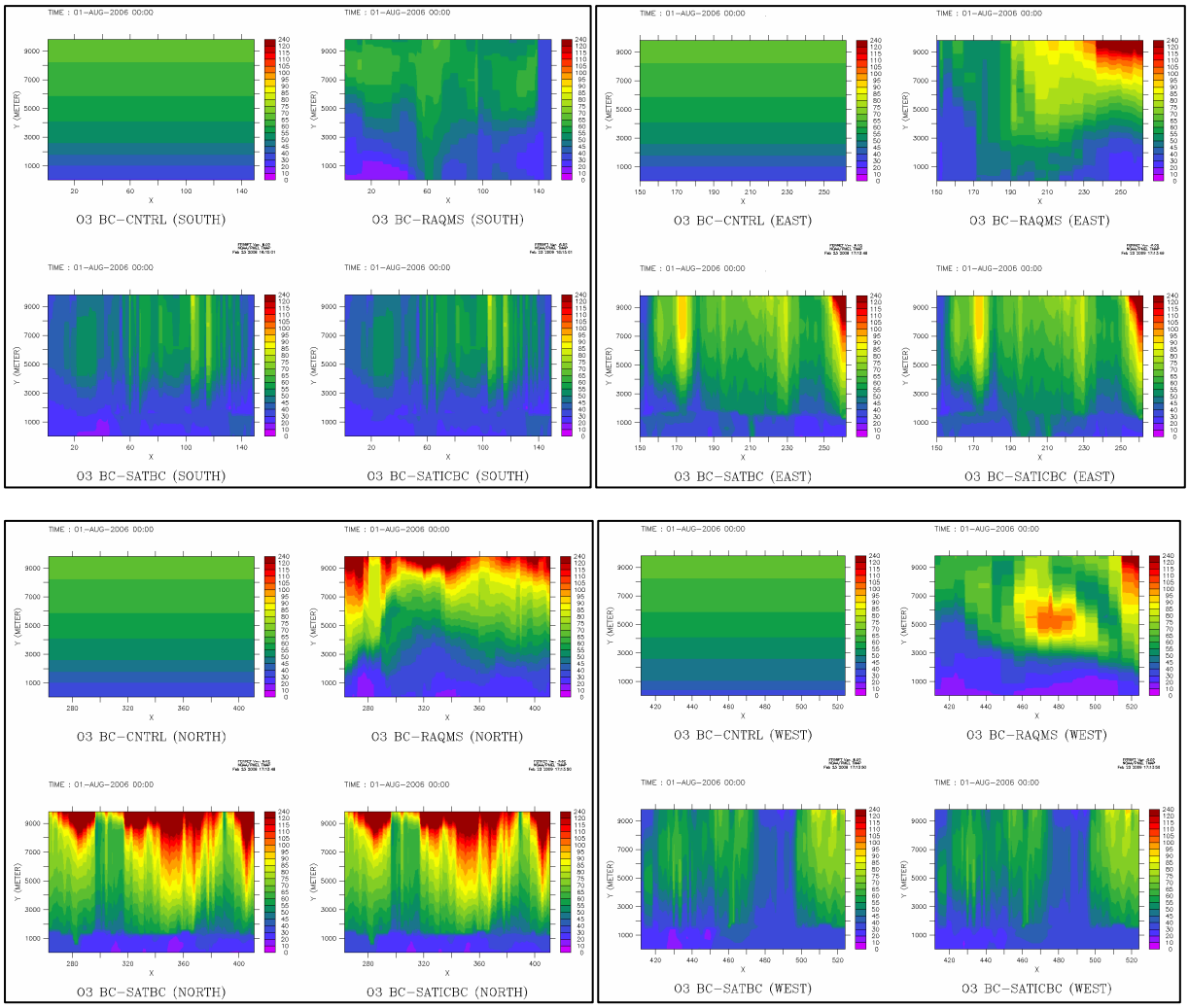


**Figure 18. Ozone (ppb) BC for south, east, north and west boundaries. In each panel BC for control (top left, standard CMAQ BC), RAQMS_BC (top right, BC from RAQMS global model), SAT_BC (lower left, BC from satellite observations) and SAT_ICBC (lower right) simulations for August 1, 2006, are presented. Notice that BC for SAT_BC and SAT_ICBC are identical. They are both included for completeness.**

**Figure 19** shows similar plots for peroxyacetyl nitrate (PAN). Our technique extracts the BC from a modified IC file. The IC file is obtained from CMAQ output at the end of the run for the previous 24-hour segment. Therefore, IC and consequently BC are impacted by the emissions and the dynamics of the previous day. This explains the difference between BC for control and SAT_BC simulations. Interestingly, vertical distribution of PAN for SAT_BC shows remarkable agreement with RAQMS_BC. To a lesser degree, this resemblance in pattern is also manifested in formaldehyde distribution in **Figure 20**, meaning that the chemical evolution within the domain of study is mainly responsible for the overall characteristics of the air mass at the boundary as the regional model produces a similar distribution in PAN and formaldehyde as the global model predicts. Such general agreement for $NO_x$ is only seen on the eastern boundary as evident in **Figure 21** while carbon monoxide does not exhibit good agreement (**Figure 22**).

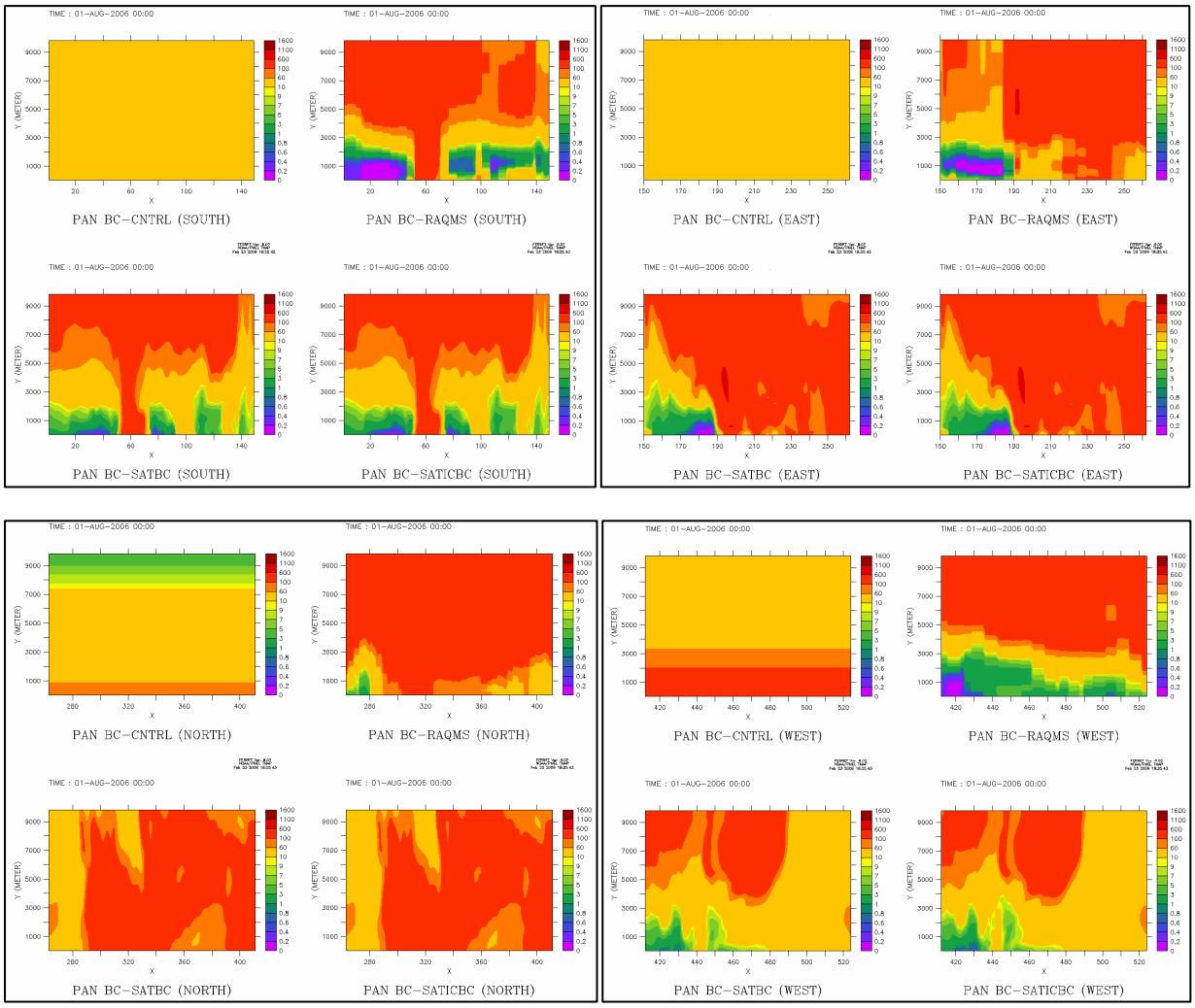


**Figure 19. PAN (ppt) BC for south, east, north and west boundaries. In each panel BC for control (top left, standard CMAQ BC), RAQMS_BC (top right, BC from RAQMS global model), SAT_BC (lower left, BC from model) and SAT_ICBC (lower right) simulations for August 1, 2006, are presented. Notice that BC for SAT_BC and SAT_ICBC are identical. They are both included for completeness.**

BC for sulfate aerosol ($ASO_4$) is shown in **Figure 23**. This information was not extracted from RAQMS and as evident from the figure, BC for RAQMS_BC is identical to the control simulation. However, since SAT_BC simulation extracts this information from the interior of the domain, the southern and eastern boundary experience the impact of $ASO_4$ loading.

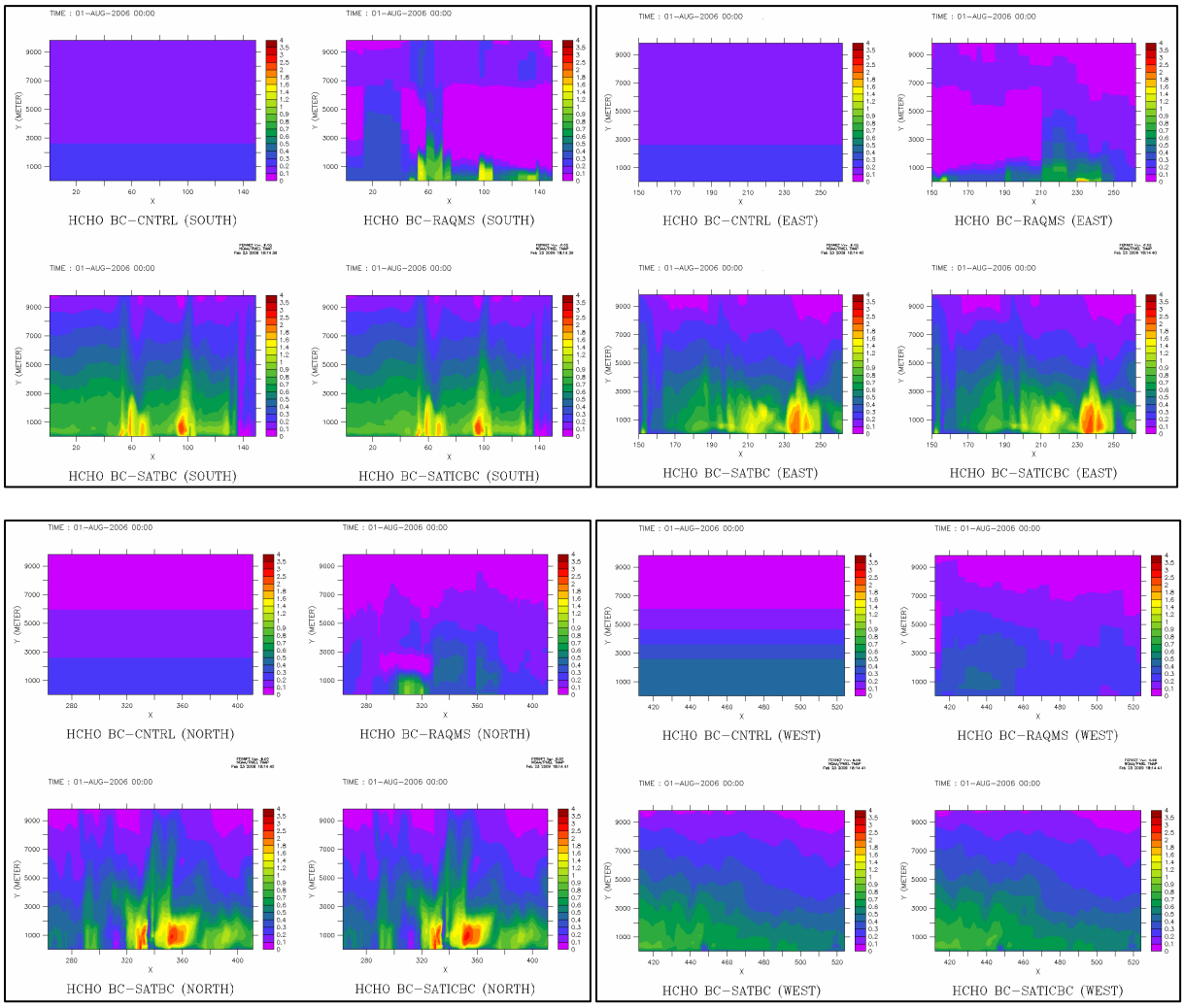


**Figure 20. Formaldehyde (ppb) BC for south, east, north and west boundaries. In each panel BC for control (top left, standard CMAQ BC), RAQMS_BC (top right, BC from RAQMS global model), SAT_BC (lower left, BC from model) and SAT_ICBC (lower right) simulations for August 1, 2006, are presented. Notice that BC for SAT_BC and SAT_ICBC are identical. They are both included for completeness.**

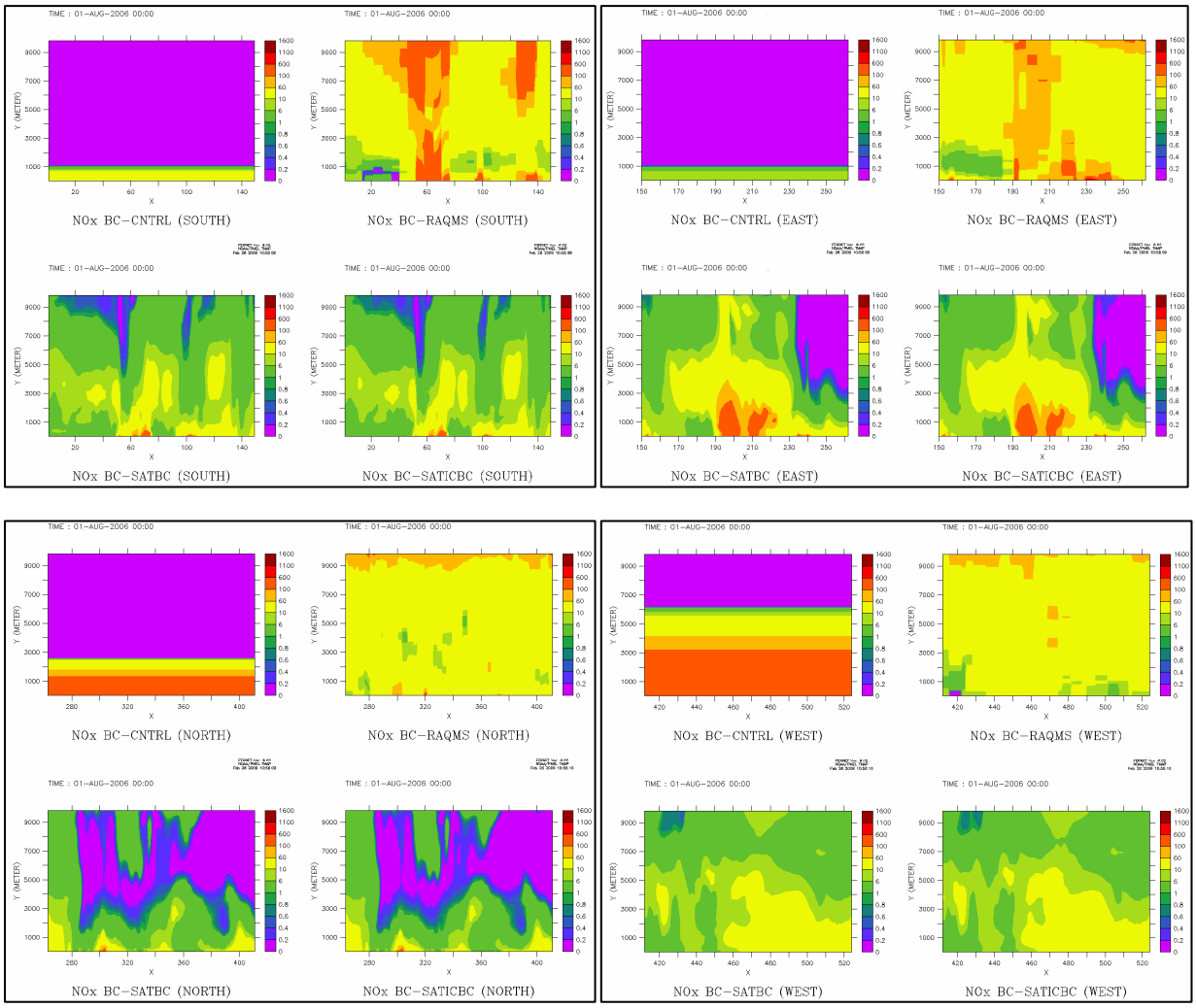


**Figure 21. $NO_x$ (ppt) BC for south, east, north and west boundaries. In each panel BC for control (top left, standard CMAQ BC), RAQMS_BC (top right, BC from RAQMS global model), SAT_BC (lower left, BC from model) and SAT_ICBC (lower right) simulations for August 1, 2006, are presented. Notice that BC for SAT_BC and SAT_ICBC are identical. They are both included for completeness.**

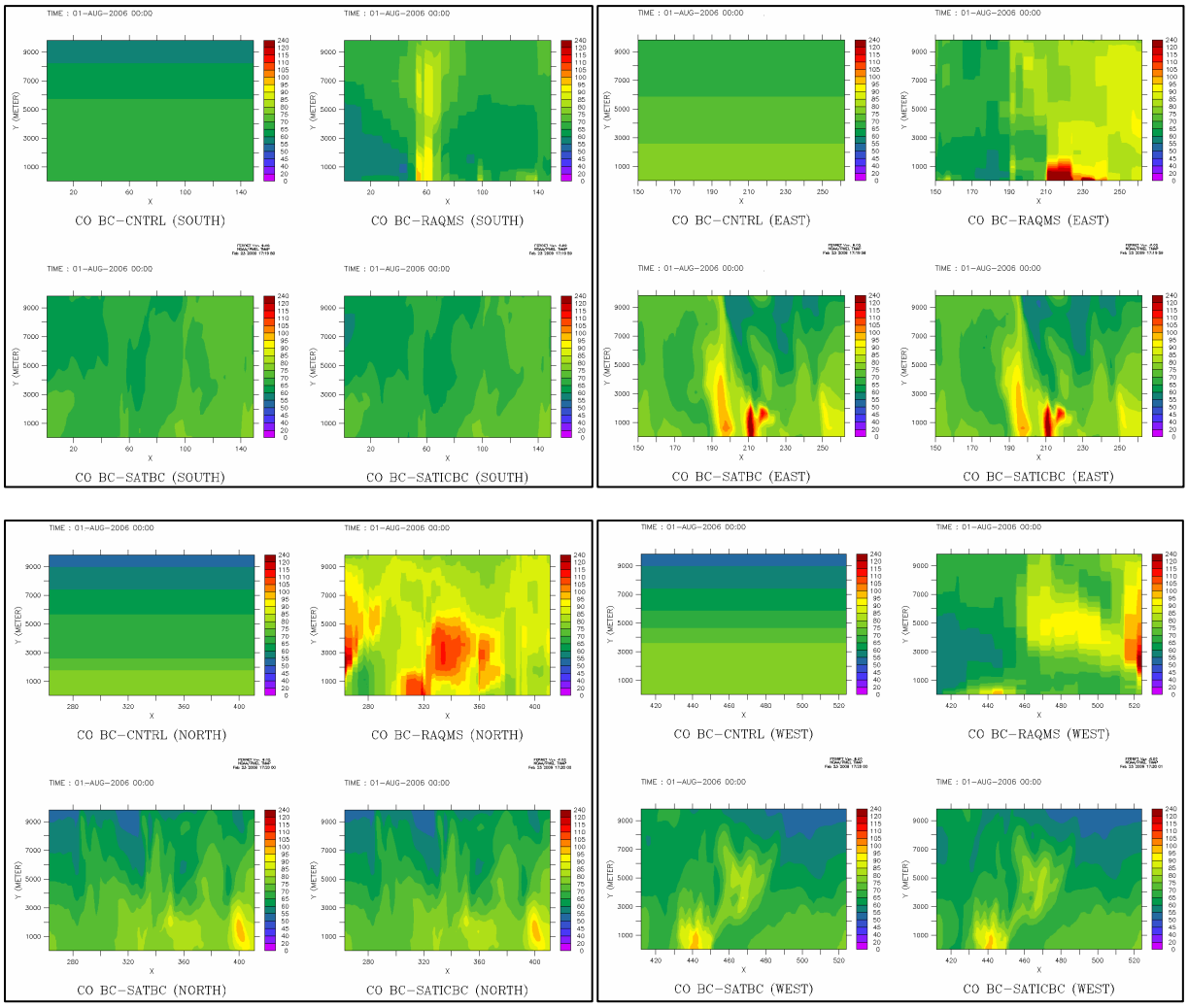


**Figure 22. Carbon monoxide (ppb) BC for south, east, north and west boundaries. In each panel BC for control (top left, standard CMAQ BC), RAQMS_BC (top right, BC from RAQMS global model), SAT_BC (lower left, BC from model) and SAT_ICBC (lower right) simulations for August 1, 2006, are presented. Notice that BC for SAT_BC and SAT_ICBC are identical. They are both included for completeness.**

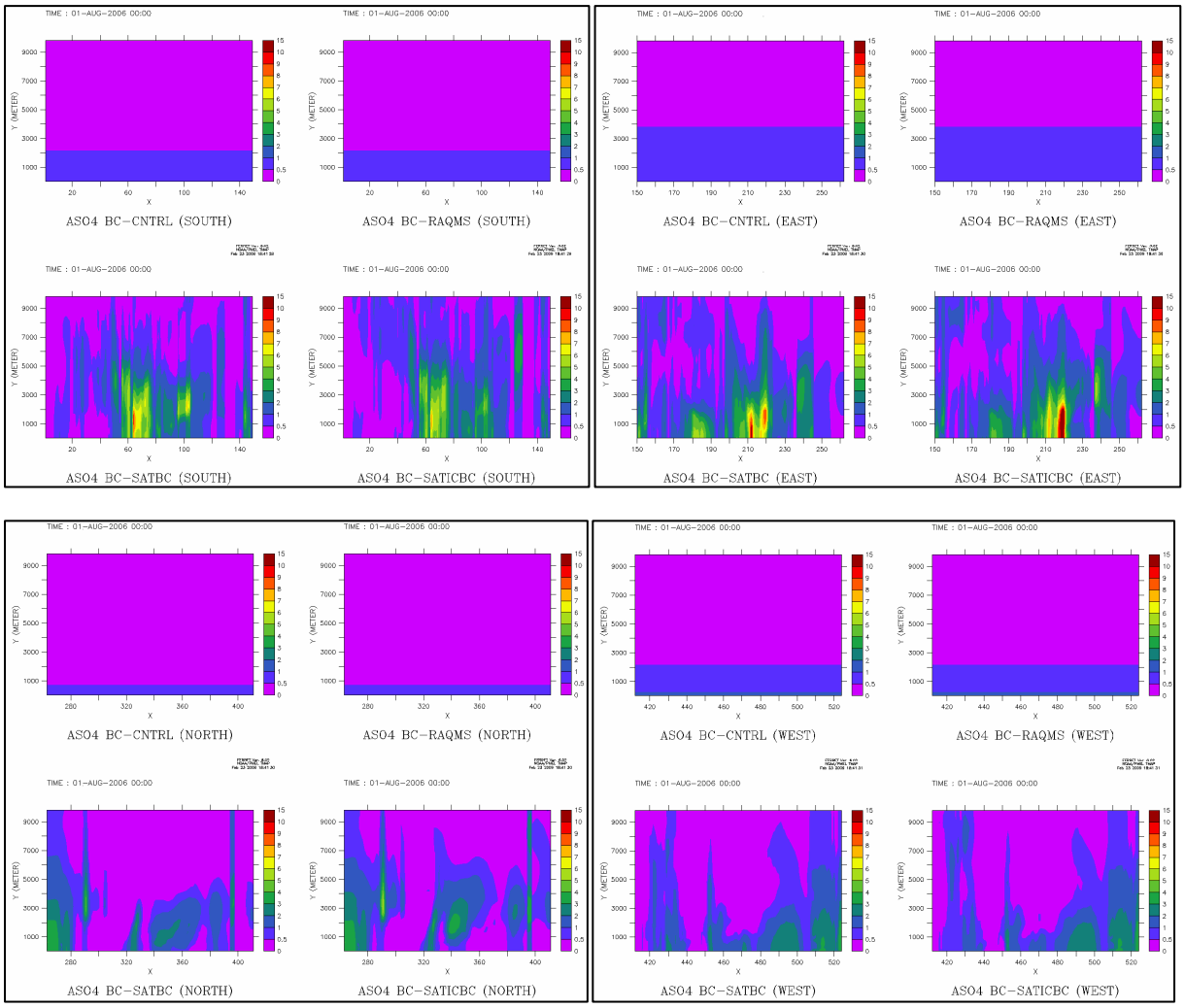


**Figure 23. Sulfate aerosol (μg/m^3) BC for south, east, north and west boundaries. In each panel BC for control (top left, standard CMAQ BC), RAQMS_BC (top right, BC from RAQMS global model), SAT_BC (lower left, BC from model) and SAT_ICBC (lower right) simulations for August 1, 2006, are presented. Notice that BC for control, RAQMS_BC, and for SAT_BC and SAT_ICBC are identical. They are included for completeness. Aerosol species from RAQMS were not mapped into CMAQ and therefore the standard CMAQ concentrations are used.**

# 3. RESULTS AND DISCUSSION

The results were evaluated in several ways in order to address some key questions in this project. As mentioned earlier, shortly after the start of this project we realized that TES observations were not adequate to provide IC/BC. On the other hand, the newly available OMI profiles could provide the necessary spatial coverage. But, OMI ozone profiles were untested and needed to be evaluated. Therefore, we were faced with the following questions: (1) what is the uncertainty of OMI $O_3$ profiles over continental U.S.; (2) can OMI $O_3$ profiles be used to provide IC/BC for air quality modeling practices over U.S.; (3) what is the impact of utilizing OMI $O_3$ for IC/BC on CMAQ performance in the free troposphere; (4) what would be the impact on surface $O_3$ predictions? In addition to addressing these questions, we also investigated the impact of utilizing MODIS AOD products on model aerosol predictions.

Ozonesonde data from IONS-06 campaign were used for evaluating OMI $O_3$ profiles and also to evaluate CMAQ performance in the free troposphere. EPA surface observations were utilized for evaluating OMI $O_3$ observations within the boundary layer and also for evaluating model performance in the boundary layer. We also used MODIS observations to evaluate model prediction of aerosols. The results of these evaluations are discussed in detail below.

## 3.1. Evaluation of OMI Ozone Profiles

OMI ozone profiles were evaluated against IONS-06 ozonesonde measurements. We also evaluated the available OMI observations within the boundary layer against EPA surface observations. 341 ozonesonde profiles for August 2006 from 18 stations that participated in the IONS-06 campaign were collected. Among them there are 23 profiles measured from the *Ronald H. Brown* ship over the Gulf of Mexico (referred as "*Ron Brown*" station). The locations for the stations are illustrated in **Figure 10** and the data is described in Section 2.2.

CMAQ vertical coordinate was used as the single vertical coordinate system for evaluation. OMI ozone profiles were mapped onto CMAQ vertical grid structure as described in Section 2.1.1.3. Ozonesonde data were also either interpolated (where model vertical spacing was less than 100 m, which is ozonesonde vertical resolution) or averaged (where model vertical spacing was more than 100 m). Direct comparison between TES, OMI and ozonesonde measurements at several sites were also performed. An example of such comparison is presented in **Figure 24**.

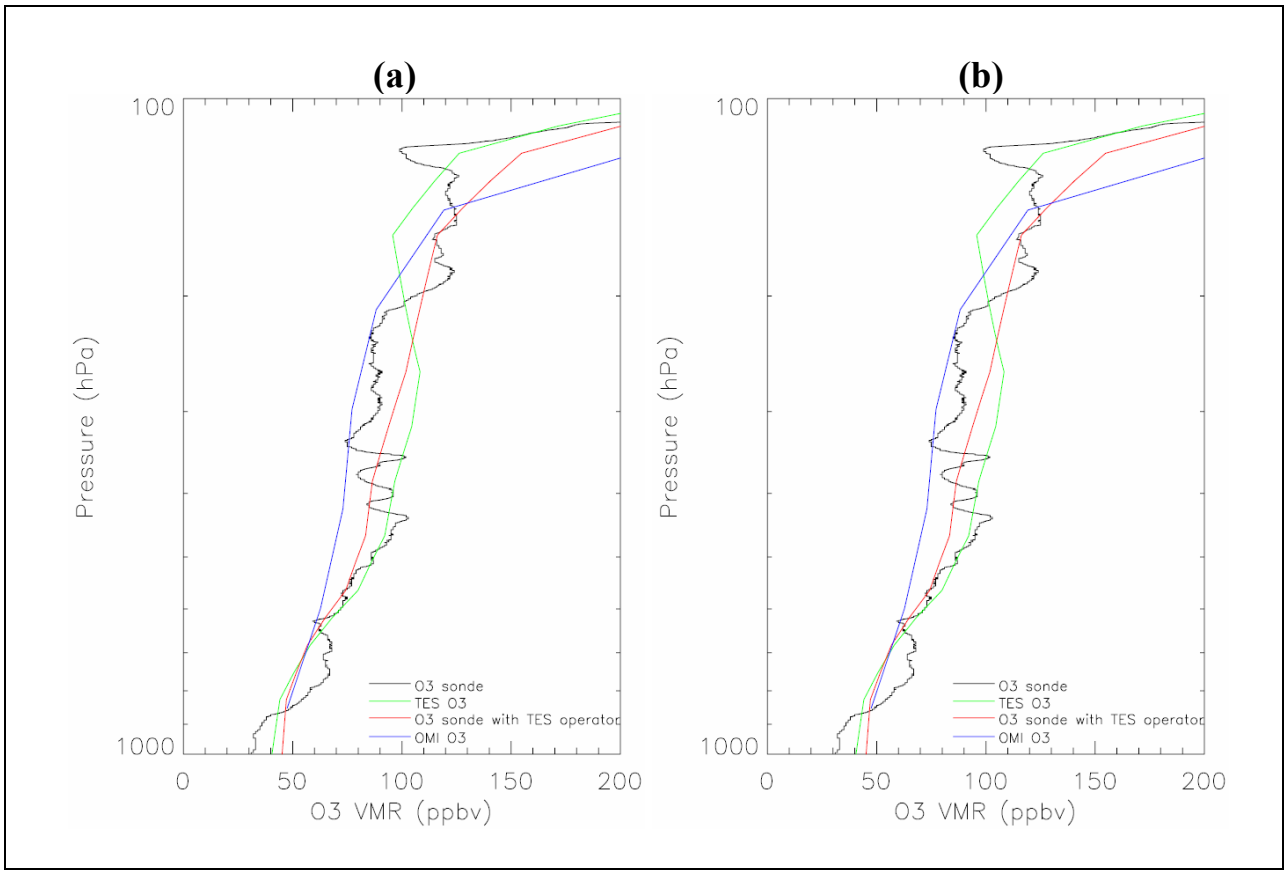


**Figure 24. An example of OMI, TES, ozonesonde comparison. (a) Measurements for 8/21/2006, *Ron Brown* ozonesonde launched at (94.73W, 29.35N), 18:50 UTC, OMI $O_3$ measured at (94.8W, 29.18N), 19:54 UTC, distance from sonde = 20.08 km, TES $O_3$ measured at (97.03W, 29.15N), 19:53UTC, distance from sonde = 224.21 km; (b) Measurements for 8/30/2006, *Ron Brown* ozonesonde launched at (94.83W, 28.5N), 17:58 UTC, OMI $O_3$ measured at (94.7W, 28.72N), 19:47 UTC, distance from sonde = 27.55 km, TES $O_3$ measured at (95.21W, 28.06N), 19:47UTC, distance from sonde = 61.46 km. The red lines in the figures are ozonesonde convolved with TES averaging kernel, which is a reconstruction of an ozonesonde profile for TES vertical resolution.**

The figure shows ozonesonde measurements for *Ron Brown* vessel on August 21 and August 30, 2006, alongside the closest OMI and TES observations. The satellite observations are about 1-2 hours behind the ozonesonde observations. TES footprint is 224-km and 61-km away from the sonde locations on August 21 and August 30 respectively. The distance from OMI footprint to sonde location is about 20-27-km on both days. As it can be seen from the figures, both TES and OMI can explain the general vertical variation of ozone. Ozonesonde measurements indicate some fine scale vertical structure and inhomogeneity that is absent in the satellite observation. This is understandable as satellite observations sample a thicker layer of the atmosphere and are not able to explain the fine scale variations. To obtain a more comparable representation of ozonesonde, the sonde profile is convolved with the TES averaging kernel A (defined as the sensitivity of the retrieval $\hat{x}$ to the true state $x$) and the *a priori* profile ($x_a$) of the satellite observation, according to the equation $\hat{x} = x_a + A(x - x_a) + \varepsilon$ [Worden et al., 2007; Rodgers and Connor, 2003; Rodgers, 2000], where $\varepsilon$ is the measurement error (set to zero here). If $x$ is

replaced by the sonde observation, then $\hat{x}$ gives the retrieved sonde profile, which is smoothed in the same way as if it would have been observed by TES, and can therefore be compared to the actual retrieved ozone profile. Both original and convolved sondes are used in the inter-comparison with the OMI profiles (**Figure 24**). A noticeable observation is the limitation of OMI in observing the boundary layer ozone. OMI observation for the lowest layer usually represents the average concentration for a thick layer extending from surdface to a hight of about 800 mb (about 2-km). This means that what is considered as the OMI boundary layer observation for the GoM region, in actuality covers both the boundary layer and part of the lower free troposphere. As evident from figure 24, the lower ozone concentration (about 30 ppb) is confined within the marine planetary boundary layer (PBL, about 500 m) and it increases above the PBL to about 50 ppb at 2 km. Both OMI and TES observations are about 40 ppb which is close to the convolved sonde concentration.

For a more comprehensive evaluation of OMI observations over the continental United States all the available ozonesonde observations were utilized. **Figure 25** shows the mean bias ($\frac{1}{N}\sum_{i=1}^{N}(O_{3_i}^{OMI} - O_{3_i}^{ozonesonde})$) and mean normalized bias ($\frac{1}{N}\sum_{i=1}^{N}\frac{(O_{3_i}^{OMI} - O_{3_i}^{ozonesonde})}{O_{3_i}^{ozonesonde}}$) for 244 pair of observations. The statistics below 800 mb (from surface to about 2-km, which covers model layers 1-17) are not reliable as the sample sizes for these layers are particularly small. **Table 9** shows the number of OMI/Sonde pairs used for each vertical layer. The number of pairs drastically jumps from 87 in layer 15 (about 1.5 km at 840 mb) to 226 in layer 16 (about 1.8 km at 810 mb). As evident from **Figure 25**, the bias decreases as the number of pairs (sample size) increase from surface to about 800 mb. OMI shows a reasonable agreement with ozonesonde in the lower- to mid-troposphere. In the upper troposphere, while the bias increases, the normalized bias does not show much variation and remains below 10%. This is due to higher ozone concentration in the upper troposphere caused by stratospheric incursion. Therefore, a 20 ppb difference in ozone concentration in the upper troposphere is still relatively small.

**Table 9. Number of OMI/Sonde Pairs Used in the Evaluation of OMI Profiles for August 2006 for Each Model Layer.**

| Layer Number | Number of OMI/Sonde Pairs | Approximate Height (km) |
|---|---|---|
| 39 | 243 | 20 |
| 38 | 244 | 16.5 |
| … | … | … |
| 21 | 244 | 4.0 |
| 20 | 243 | 3.5 |
| 19 | 242 | 3 |
| 18 | 243 | 2.5 |
| 17 | 242 | 2.1 |
| 16 | 226 | 1.8 |
| 15 | 87 | 1.5 |
| 14 | 47 | 1.2 |
| 13 | 31 | 1.0 |
| 12 | 22 | 0.87 |
| 11 | 10 | 0.69 |
| 10 | 8 | 0.51 |
| 9 | 7 | 0.43 |
| 8 | 3 | 0.34 |
| … | … | … |
| 6 | 3 | 0.17 |
| 5 | 1 | 0.13 |
| 4 | 0 | 0.084 |
| … | … | … |
| 1 | 0 | 0.008 |

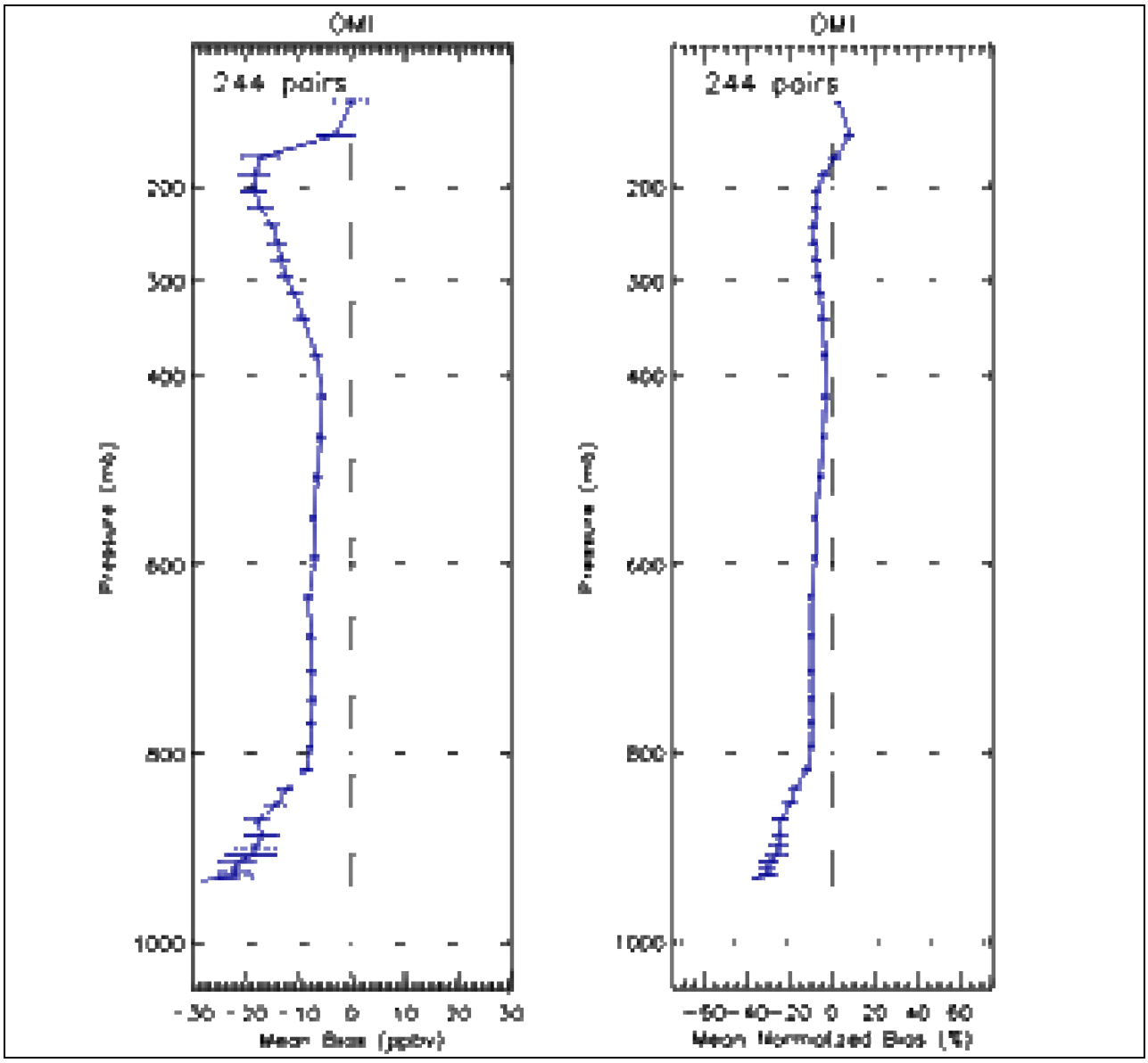


**Figure 25. OMI/ozonesonde comparison over United States for August 2006 during IONS-06 campaign. Mean bias** $(\frac{1}{N}\sum_{i=1}^{N}(O_{3_i}^{OMI} - O_{3_i}^{ozonesonde}))$ **and mean normalized bias** $(\frac{1}{N}\sum_{i=1}^{N}\frac{(O_{3_i}^{OMI} - O_{3_i}^{ozonesonde})}{O_{3_i}^{ozonesonde}})$ **from 244 pair of observations are presented. For many of the observations OMI did not extend below 800 mb, thus the statistics below 800 mb (about 2-km, model layers 1-17) is not reliable as they represent a small sample. For example the number of pairs for model layers 5 through 11 is 1, 3, 3, 3, 7, 8, and 10 respectively.**

OMI overpass time is about 1:30 PM local time. It is safe to assume that **over land** during August, at 1:30 PM the boundary layer is well mixed, and therefore, OMI measurements at the

lowest layer is representative of the boundary layer (BL) ozone concentrations and can be compared to EPA's surface observations over the continental United States. It should be acknowledged that OMI observations are representing a volume averaged quantity for a relatively large volume of air, while surface observations are point measurements. Furthermore, a substantial number of surface monitors are impacted by local emissions and there is a large spatial variability even for stations that are only separated by a few kilometers. Therefore, one expects to see a large scatter when surface/OMI observation pairs are compared. However, one also expects to see higher ozone concentrations for OMI observations when a cluster of surface monitors observe elevated ozone concentrations. Based on this reasoning, we constructed observational pairs of OMI ozone observations in the boundary layer vs. observations from EPA's surface monitors for July 15 through September 7, 2006. The pairs are constructed by extracting daily surface observations at 14:00 local time and pairing them with OMI observations.

**Figure 26** shows a scatter plot illustrating these observational pairs. The figure indicates that neither the elevated surface concentrations nor the large variations experienced by the surface monitors is explained by OMI. The correlation coefficient is 0.14, indicating a relatively low correlation between the two observations. For OMI, the mean and standard deviation are 48.2 and 7.9 respectively, while for surface monitors, the mean and standard deviation are 48.9 and 16.7 respectively. The mean for OMI and surface monitors are close indicating that OMI explain the mean observed concentration. But the relatively small standard deviation for OMI compared to that of surface monitors indicate that OMI is not able to explain extreme events.

Since the scatter plot indicated that OMI O3 measurements for the boundary layer do not explain the large variations seen at the surface monitors, we examined OMI spatial patterns against the surface observations to establish their ability in realizing high/low regions. This was done to see whether OMI is able to explain spatial patterns of high versus low ozone or not. **Figure 27** shows the spatial plots for OMI and surface monitors for August 3, 21, and 31, 2006. These days have been chosen to represent different scenarios in the observations. On August 3 and 21, there is a general agreement between OMI observations and that of the surface monitors. While OMI underestimates elevated ozone concentrations, it is able to explain the larger scale spatial variation seen in the surface monitors. But on August 31, there is a substantial disagreement between OMI and surface monitors and OMI totally misses the surface observations. As mentioned above, OMI's first layer can represent boundary layer and part of the lower free troposphere (surface to about 800 mb). In these comparisons it is assumed that the first layer in OMI observations represents boundary layer. It could be that in cases such as August 31, OMI observation represents the higher concentration above the boundary layer. Based on these preliminary results, a more rigorous examination of OMI retrievals within the boundary layer is needed to explain the cause of such significant disagreements with the surface observations. Nevertheless, on days where there is a general agreement in the spatial patterns, there is a possibility of scalling OMI observations to be more representative of the boundary layer. It should be noted that this analysis pertains to the OMI measurements over land (where EPA surface monitors are located) and does not apply to the observations over GoM.

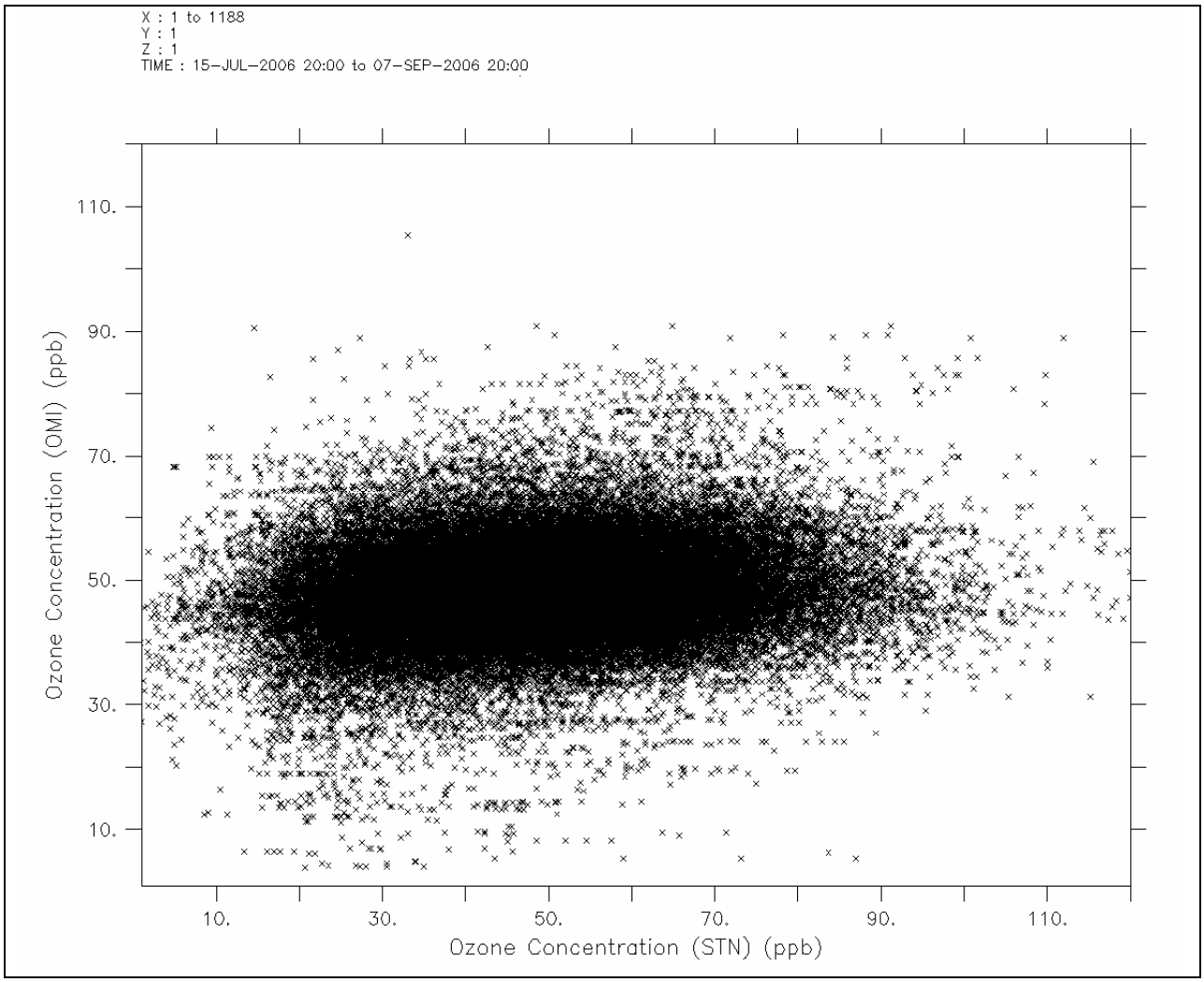


**Figure 26. Scatter plot showing OMI ozone observations in the boundary layer vs. observations from EPA's surface monitors for July 15 through September 7, 2006. The pairs are constructed by extracting daily surface observations at 14:00 local time and pairing them with OMI observations. The figure indicates that OMI is not able to neither explain elevated surface concentrations nor the large variations experienced by the surface monitors. The correlation coefficient is 0.14, while the mean and standard deviation for OMI are 48.2 and 7.9 respectively, and for surface monitors are 48.9 and 16.7 respectively.**

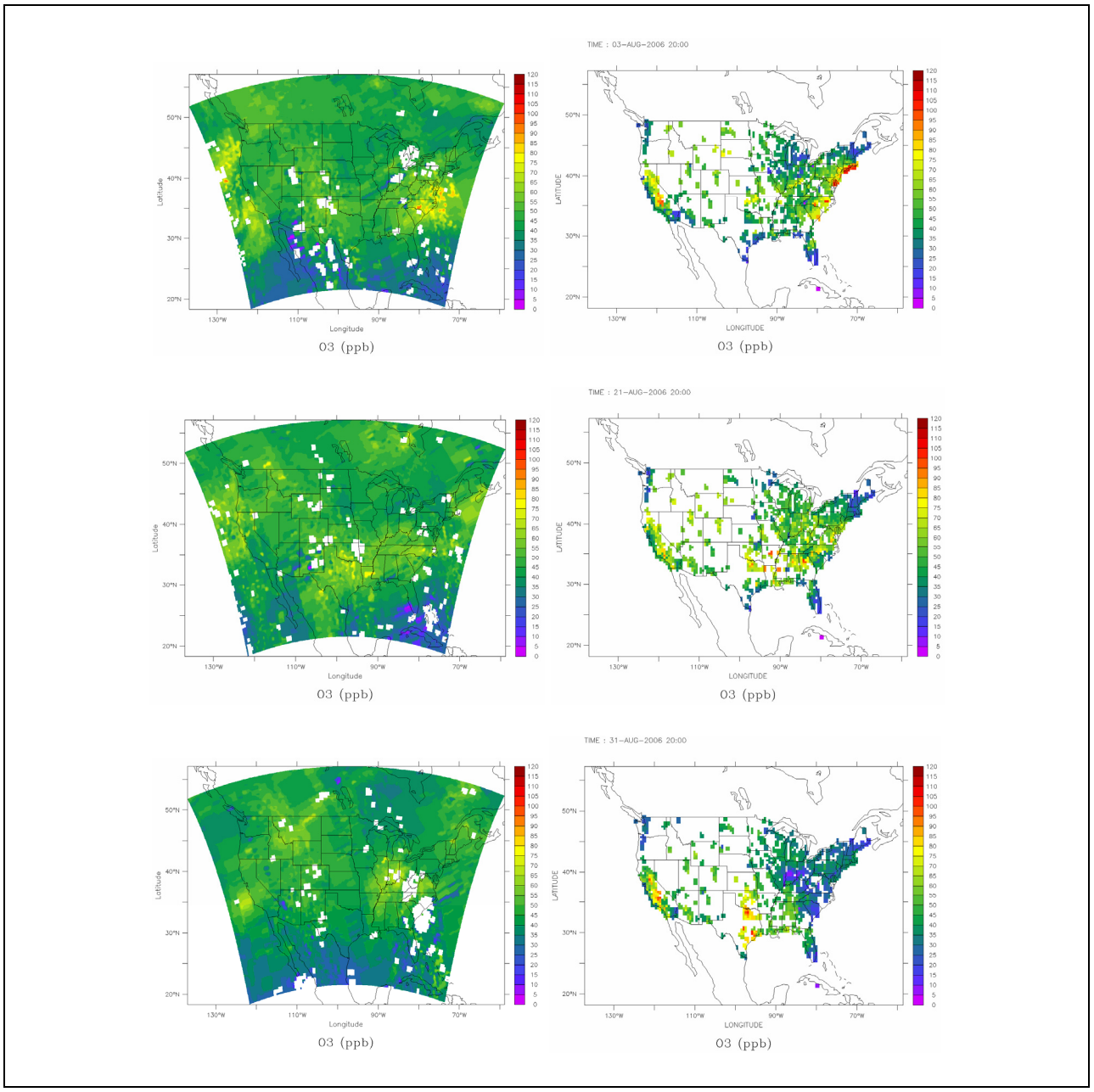


**Figure 27. OMI ozone observations (left panel) versus observations by surface monitors (right panel) for August 3, 21, and 31, 2006. While on August 3 and 21 there is a better agreement between the spatial patterns, on August 31, OMI observations are not representative of the boundary layer.**

To examine the OMI observations in the marine boundary layer and over the GoM region, the limited number of ozonesonde observations from *Ron Brown* vessel were utilized. Unfortunately, most of the time the vessel stayed very close to the coast and on days that the ship is farther away (e.g., August 2 and 16) the ozonesonde data is not available. **Table 10** presents the location and time for *Ron Brown* surface observations versus OMI first layer retrieval and the

time of satellite overpass. These data are presented in **Figure 28,** which shows a scatterplot depicting *Ron Brown* surface ozone observations versus OMI first layer retrievals. While the sample size is small, the pattern is very similar to what is observed in **Figure 26** which shows OMI observations versus surface stations. It seems that OMI is not able to explain the lower ozone concentrations within the boundary layer and tends to conform to a narrow range about the maean concentration.

**Table 10. OMI/*Rown Brown* Vessel Surface Ozone Measurements for August 2006. (Missing values are marked as -999)**

| DAY August | LAT | LON | *Ron Brown* time | OMI time | *Ron Brown* O3 | OMI O3 |
|---|---|---|---|---|---|---|
| 2 | 26.76 | -95.09 | 19 | 19 | -999. | 36.18 |
| 3 | 29.63 | -94.63 | 17 | 20 | 16.50 | 42.76 |
| 4 | 29.68 | -95.01 | 18 | 19 | 45.00 | 47.67 |
| 6 | 28.00 | -95.52 | 18 | 18 | 24.50 | 47.34 |
| 7 | 28.11 | -96.44 | 18 | 19 | 28.00 | 34.36 |
| 9 | 29.87 | -93.93 | 18 | 19 | 53.50 | 43.60 |
| 11 | 29.75 | -95.29 | 18 | 19 | 29.00 | 47.17 |
| 12 | 29.21 | -94.67 | 18 | 19 | -999. | 42.16 |
| 13 | 29.68 | -95.01 | 18 | 19 | 15.00 | 34.51 |
| 15 | 29.68 | -95.01 | 18 | 18 | 39.00 | 36.93 |
| 16 | 26.63 | -94.96 | 18 | 19 | -999. | 41.07 |
| 17 | 29.64 | -94.96 | 19 | 20 | 91.00 | 49.35 |
| 18 | 29.31 | -94.79 | 18 | 19 | 18.00 | 44.44 |
| 21 | 29.35 | -94.73 | 18 | 19 | -999. | 47.50 |
| 22 | 29.00 | -94.66 | 17 | 18 | 32.50 | 43.89 |
| 23 | 28.55 | -96.51 | 19 | 19 | 33.00 | 35.69 |
| 24 | 29.32 | -94.55 | 18 | 18 | 30.00 | 46.51 |
| 26 | 29.68 | -95.01 | 19 | 20 | 25.00 | 36.04 |
| 27 | 29.68 | -94.99 | 18 | 00 | 20.00 | -999. |
| 28 | 28.95 | -94.77 | 19 | 19 | 11.00 | 35.95 |
| 29 | 28.50 | -94.83 | 17 | 19 | 15.00 | 36.61 |
| 30 | 28.50 | -94.83 | 17 | 19 | 41.50 | 39.52 |
| 31 | 28.50 | -94.83 | 18 | 18 | -999. | 35.51 |


**Figure 28. Scatter plot showing ozone concentrations for *Ron Brown* ozonesonde observations at the surface versus OMI first layer observations.**

## 3.2. Model Performance in the Free Troposphere

Ozonesonde measurements from IONS-06 campaign (as described in Section 2.2) are used to evaluate model performance in the free troposphere. For each day during August 2006, ozonesonde measurements within 1500~2300 UTC are compared with ozone mixing ratios at 1900 UTC simulated by four CMAQ runs (CNTRL, RAQMS_BC, SAT_BC, and SAT_ICBC as described in Section 2.3). The control simulation significantly underestimates ozone concentrations in the upper troposphere; while ozone concentrations from all other simulations are closer to those measured by ozonesondes (**Figure 29**). The bias in terms of concentration is the largest in the upper troposphere. However, when the bias is presented as the percent difference, only the control simulation shows large deviations from Ozonesonde measurements from 5 to 13 km. Further improvement has been made in the interior region by applying satellite data as IC (SAT_ICBC) for each 24-hour segment. As evident in the figure, the best performance in the free troposphere is achieved by SAT_ICBC run. While SAT_ICBC simulation performs much better in most of the free troposphere, it overestimates ozone at upper layers in the model (average elevation above 12 km). This could be due to artificial diffusion at the model top layers. In these simulations we tried to minimize the numerical diffusion and

artificial incursion of stratospheric air into the mid-troposphere by reducing the vertical grid spacing between 8 and 12 km. As evident from the results for RAQMS_BC, SAT_BC, and SAT_ICBC it seems that this approach has worked. The results from all of these simulations indicate that the higher ozone concentrations at the top of the model do not penetrate to lower layers and the mean normalized bias at 8- to 12-km elevation is relatively low.

**Figure 30** presents the same plots as **Figure 29** alongside bias plots for OMI ozone profiles. This is to show that while for OMI the top two layers are very close to Ozonesonde measurements, for SAT_ICBC run, the model is underestimating the top layer and overestimating the layers below the top layer which is indicative of excessive mixing in the model top layer. In these simulations the top two layers were about 3.5 and 1.5 km thick compared to about 0.5-0.8 km spacing in the other layers. Since $O_3$ vertical gradient at the top layer is the highest and ozone concentrations can go from less than 100 pbb to 800 ppb (**Figure 5**), even a small artificial incursion from the top layer can have large impact on the lower layers. For our future simulations we have added two more layers at the top to keep the grid spacing to a maximum of 1 km. We think that this change in grid configuration will minimize the excessive mixing seen in the current results.

While the overall statistics are useful in evaluating the model performance as a whole, it does not offer an insight into the model performance at specific regions. Examining the model results for each individual site offer a better understanding of the processes involved. Both RAQMS_BC and SAT_BC simulations show substantial improvements in the column distribution of ozone when compared to Ozonesonde measurements that are close to the lateral boundary of the domain. Over sonde stations such as Kelowna (northwest), Bratt's Lake (north), Egbert and Paradox (northeast), Trinidad Heas, Table Mountain, and Holtville (west, sowthwest) the impact of the boundary condition in improving model performance is more noticeable (stations are marked on the map in **Figure 10**). However, over the sonde stations in the interior of the domain, such as Huntsville, Houston, Socorro, and Boulder, the improvements in the model is limited to very top layers.

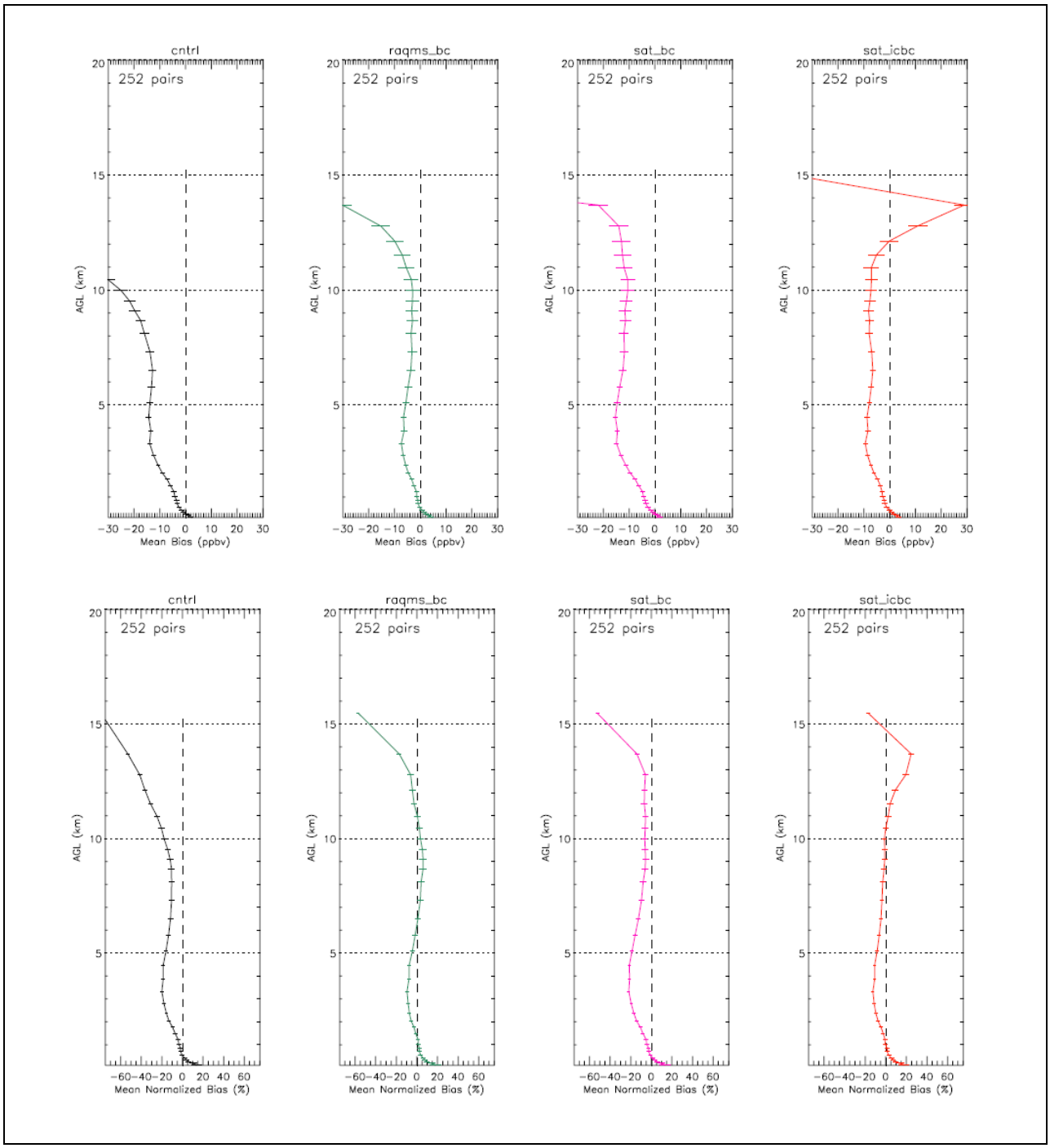


**Figure 29. Model performance evaluated against ozonesonde measurements for August 2006. The upper panel shows the bias in ppb, while the lower panel expresses the bias as the percentage for four simulations: control, BC provided from RAQMS, BC provided from satellite observations, BC provided from satellite observations and ozone in IC replaced by satellite observations every 24 hours.**

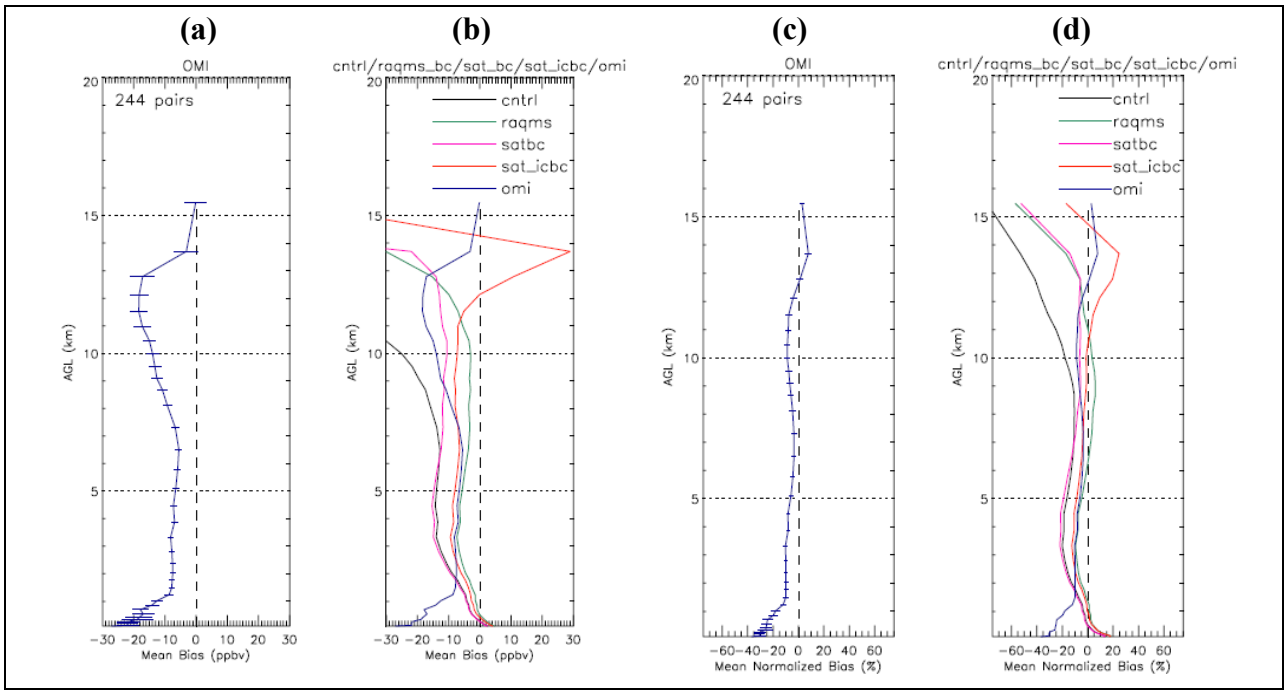


**Figure 30. OMI $O_3$ profiles and model results evaluated against ozonesonde measurements for August 2006. Also plotted in this figure is the bias for OMI $O_3$ profiles. (a) and (b) show the bias in ppb, while (c) and (d) express the bias as the percentage for four simulations: control, BC provided from RAQMS, BC provided from satellite observations, BC provided from satellite observations and ozone in IC replaced by satellite observations every 24 hours.**

**Figures 31-33** show the curtain plots for several selected sites. **Figure 31** shows the results from CNTRL simulation, while **Figure 32** and **Figure 33** show the results from SAT_BC and SAT_ICBC respectively. Ozonesonde measurements are mapped to the model vertical structure and plotted over curtain plots. Therefore, when the Ozonesonde measurements are visible on top of the model results, it means that there is a large disagreement between the model and the observations. As evident from **Figure 31,** the CNTRL simulation is greatly underestimating ozone concentration for all the stations. The underestimation is more pronounced at the stations to the north. This is due to the lower tropopause height for the northern latitudes and consequently higher ozone concentrations at lower altitudes which is absent in the CNTRL simulation. The results from SAT_BC show a significant improvement over CNTRL simulation. The improvements are more pronounced over Kelowna (northwest) and Egbert (north/northeast) stations and are reasonable for Holtville (west/southwest). But for the interior stations, Huntsville and Houston, the improvements are marginal. For these stations while some of the higher ozone values for the upper layer are reproduced by the model, in the mid to upper troposphere ozone is still underestimated. Much of this underestimation is corrected in SAT_ICBC simulation as evident from **Figure 32.** The Ozonesondes are hardly visible in this figure, meaning that there is a good agreement between the model and the observations. One also notices the higher ozone concentration for the top layer in agreement with Ozonesonde observations.

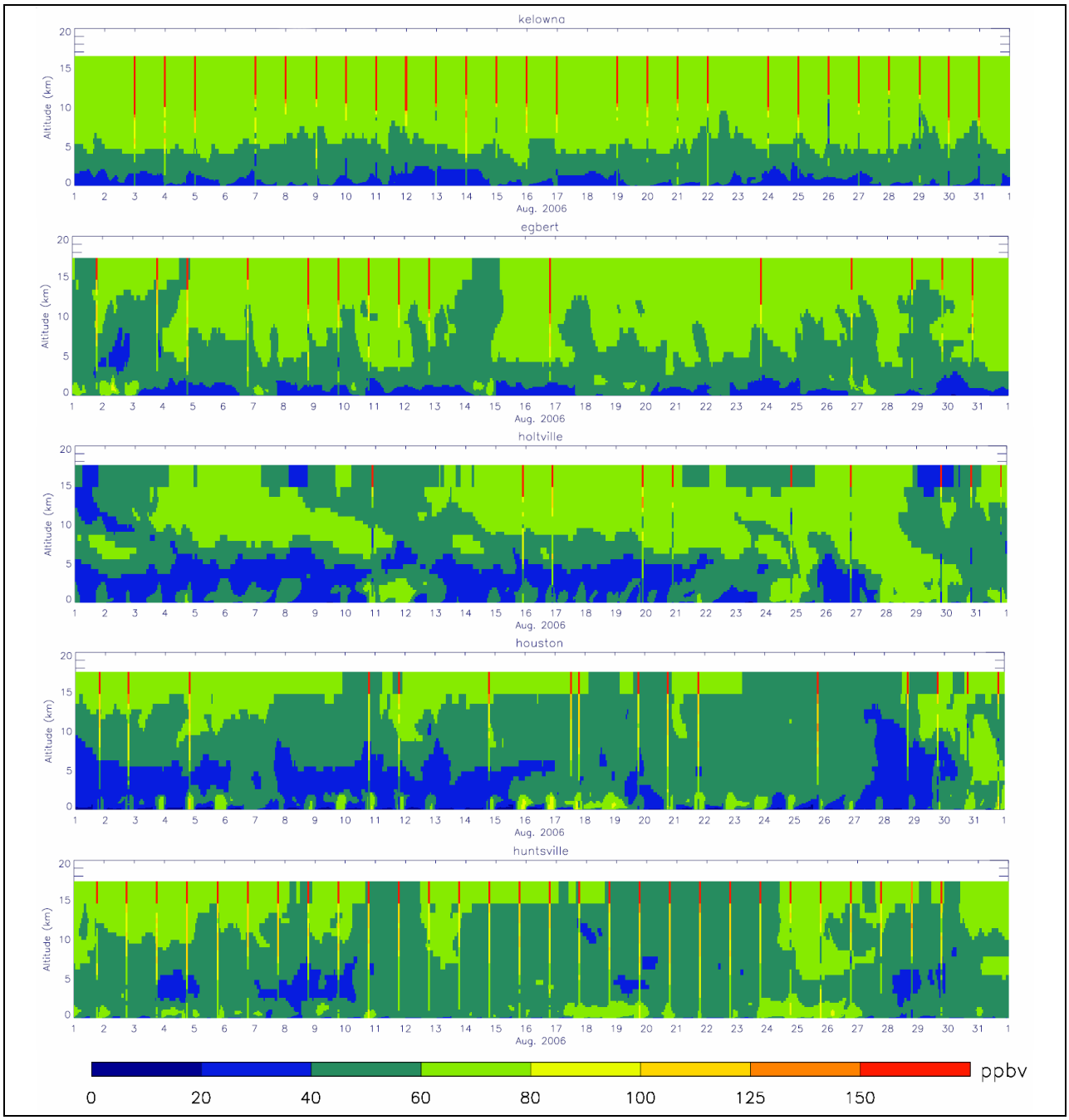


**Figure 31. Curtain plots showing CMAQ simulated ozone concentrations from CNTRL simulation versus ozonesonde measurements for the month of August 2006. Ozonesonde observations are re-sampled onto the model vertical grid structure and plotted over model predictions. Stations are marked on the map in Figure 10.**

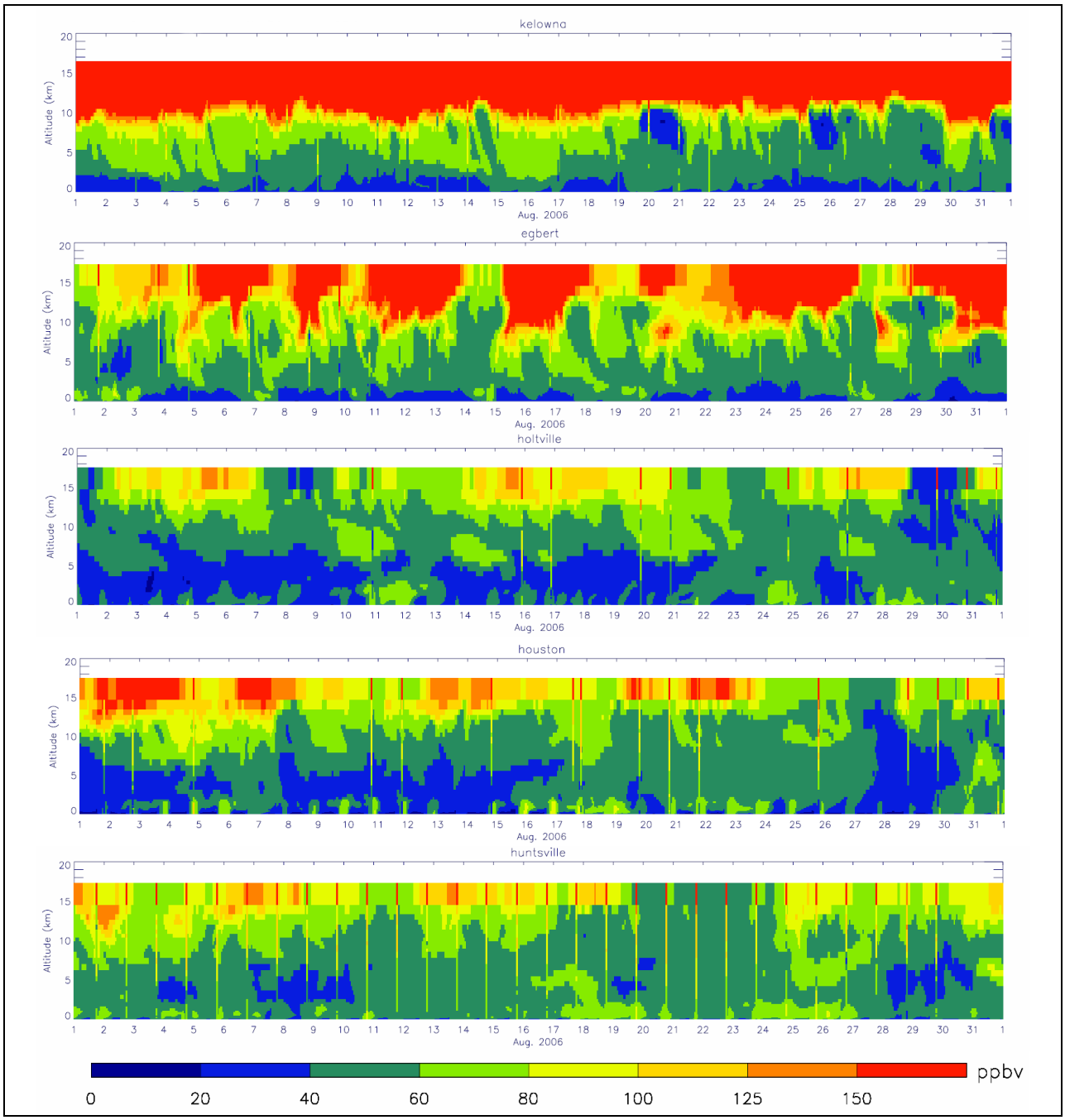


**Figure 32. Curtain plots showing CMAQ simulated ozone concentrations from SAT_BC simulation versus ozonesonde measurements for the month of August 2006. Ozonesonde observations are re-sampled onto the model vertical grid structure and plotted over model predictions. Stations are marked on the map in Figure 10.**

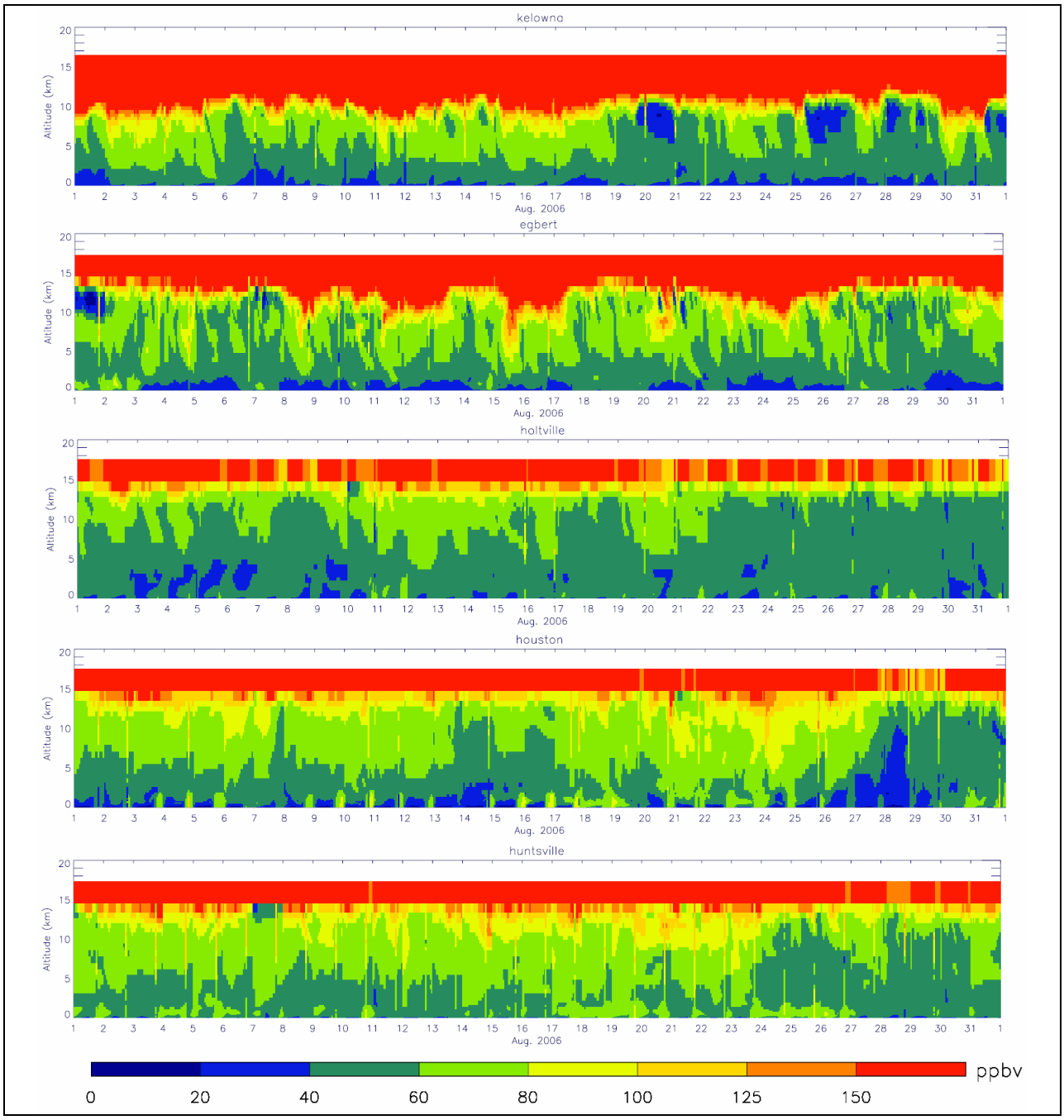


**Figure 33. Curtain plots showing CMAQ simulated ozone concentrations from SAT_ICBC simulation versus ozonesonde measurements for the month of August 2006. Ozonesonde observations are re-sampled onto the model vertical grid structure and plotted over model predictions. Stations are marked on the map in Figure 10.**

These simulations also demonstrated that in the free troposphere, and in particular the upper troposphere, the transport is the dominant process in determining ozone concentration. Therefore, if the lateral boundary condition is correctly specified, the horizontal transport replenishes ozone at the top model layers within few days even when the top boundary condition in the model is poorly specified. This implies that the correct specification of lateral BC is able to explain some of the stratospheric/tropospheric exchange (STE). Tang et al. (2007) investigated the sensitivity of a regional chemical transport model (CTM) to the top boundary condition that was provided by three different global CTMs. The regional model predictions above 4-km were strongly impacted by the top boundary condition. But, there are several practical problems in specifying the top boundary from global models. First, is the mapping of vertical layers if the vertical coordinate systems between the global model and the regional model are not the same? Since the ozone vertical gradient is the largest at the top of the regional model, such mapping introduces large interpolation errors. Second, in most cases the dynamics between the two models are not similar and an STE event in the global model may not agree in the extent, location, and timing with the regional model.

**Figure 34** presents ozone spatial plots from four CMAQ simulations at 212 and 500 mb for August 21, 2006, 19:00 GMT. Plotted over CMAQ fields are Ozonesonde measurements launched between 15:00 and 23:00 GMT. At 212 mb, layer 33 in the 39 layer CMAQ domain, it can be seen that model predictions progressively are improving from CNTRL to SAT_ICBC simulation. What is interesting is the similarity between RAQMS_BC and SAT_BC runs. Both simulations indicate improvements in the northern and southern part of the domain over the control simulation. However, Ozonesonde measurements over Huntsville and Socorro stand out as they indicate higher concentrations than the model is predicting. SAT_ICBC exhibits the best agreement with the observation, indicating the advantage of using OMI measurements for initializing each modeling segment. At 500 mb, while the model predictions are somewhat improved, they are still under-predicting the observed values. One of the inadequacies in our technique in specifying the BC from OMI observations has been the use of a constant profile for a 24 hour simulation segment. This is evident as both SAT_BC and SAT_ICBC simulations miss the higher ozone concentrations to the north (at 500 mb), while RAQMS_BC is able to explain it. Interpolating between two daily profiles and scaling it to a diurnal pattern can serve as a solution and will be pursued in the future.

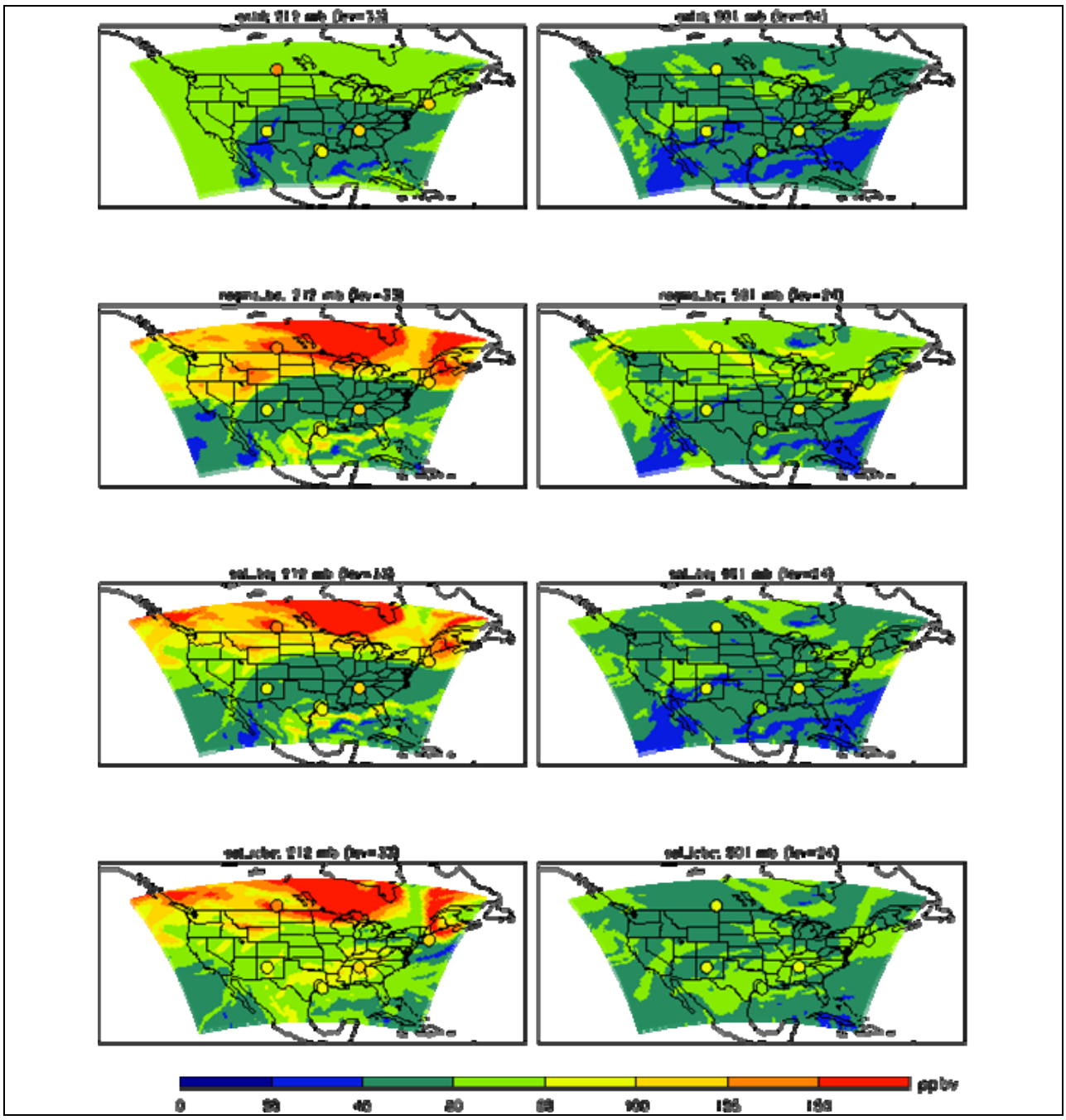


**Figure 34. $O_3$ (ppbv) spatial plots at 1900 UTC, August 21, 2006, simulated by 4 CMAQ runs; plotted over model fields are 6 ozonesondes measurements launched between 1500~2300 UTC. Left panels represent CMAQ level 33 (212 hPa). Right panels represent level 24 (501 hPa).**

## 3.3. Model Performance in the Boundary Layer

### 3.3.1. Ozone

The performance of the model was evaluated at EPA monitoring stations. The statistical measures include the Mean Bias (MB), Mean Error (ME), Mean Normalized Bias (MNB), Mean Normalized Error (MNE), Mean Fractional Bias (MFB), and Mean Fractional Error (MFE) in hourly averaged concentrations predicted at these stations. Mathematical formulation of these metrics is provided in **Table 11**. Since the normalized quantities can become large when observations are small, a cut-off value of 60, 10, and 120 ppb for $O_3$, $SO_2$, and CO respectively is used while computing MNB and MNE statistics. Thus, whenever the observation is smaller than the cut-off value, the prediction-observation pair is excluded from the calculation. The hourly normalized bias and error metrics are presented as daily averages over all monitoring stations.

**Table 11. Statistical Metrics for Air Quality Model Performance Evaluation.**

| Metrics | Formulation | Notes |
|---|---|---|
| Mean Bias (MB) | $\frac{1}{N}\sum_{i=1}^{N}\left(C_i^s - C_i^o\right)\times 100\%$ | Computed when observation is greater than 0.0 |
| Mean Error (ME) | $\frac{1}{N}\sum_{i=1}^{N}\left\|C_i^s - C_i^o\right\|\times 100\%$ | Same as MB |
| Mean Normalized Bias (MNB) | $\frac{1}{N}\sum_{i=1}^{N}\frac{\left(C_i^s - C_i^o\right)}{C_i^o}\times 100\%$ | Computed when observation is greater than the cut-off value which is set at 0.06, 0.01, and 0.120 ppmv for $O_3$, $SO_2$ and CO. |
| Mean Normalized Error (MNE) | $\frac{1}{N}\sum_{i=1}^{N}\frac{\left\|C_i^s - C_i^o\right\|}{C_i^o}\times 100\%$ | Same as MNB |
| Mean Fraction Bias (MFB) | $\frac{1}{N}\sum_{i=1}^{N}\frac{\left(C_i^s - C_i^o\right)}{\frac{C_i^s + C_i^o}{2}}\times 100\%$ | Computed when observation is greater than the cut-off value which is set at 0.06, 0.01, and 0.120 ppmv for $O_3$, $SO_2$ and CO. |
| Mean Fraction Error (MFE) | $\frac{1}{N}\sum_{i=1}^{N}\frac{\left\|C_i^s - C_i^o\right\|}{\frac{C_i^s + C_i^o}{2}}\times 100\%$ | Same as MFB |

The statistical analysis was followed by visual inspection of predicted concentrations fields and the observations were plotted over the concentration fields. This helped in identifying dynamics of pollutant plumes in the region, and helped interpreting the performance issues related to individual monitors. For example, poor model performance at a monitoring station

might be related to displacement of a plume due to error in wind direction. Finally, time series plots of predicted and observed hourly concentrations provided a stringent test of how well the model replicates the observed hourly concentration at the same time and location as the observed value. Problems with diurnal variation in predicted concentrations were readily apparent in the time series plot. Since in this study the CNTRL simulation served as the reference point to be compared to other simulations, it was thoroughly evaluated.

**Table 12** presents the statistics from CNTRL run for the five sub-regions shown in **Figure 14**. Bias for all sub-regions is about 6 ppb with the normalized bias being -7% for the Midwest region. The positive bias is caused by the systematic over-prediction of ozone at night in CMAQ. CMAQ over-predicts ozone at night and under-predicts it during the daytime peaks. Since MNB does not include the lower values at night, it shows an under-prediction of 7-12% for different sub-regions. The under-prediction is the lowest in the Midwest region at 7%, followed by 9% in the Mid-Atlantic/Northeast region, 10% in the Central region, 11% in the Southeast region and 12% in the Western region.

Comparing the other simulations to the control offers a mixed result. Some metrics show improvements, while the others indicate deterioration. However, the overall picture is consistent and indicates an overall increase in ozone concentration in RAQMS_BC, SAT_BC and SAT_ICBC simulations. That is, the nighttime over-prediction is exacerbated, but the daytime under-prediction is improved. **Figure 35** shows the mean observed concentration for each sub-region (and also the overall) versus model predictions for August 2006. RAQMS_BC over-predicts ozone in all regions while SAT_BC and SAT_ICBC exhibit a better agreement with the average observations for MANEVU and CENRAP regions. The average concentrations represent daytime, as well as nighttime observation/prediction pairs. As mentioned before, much of the over-prediction is due to the nighttime over-prediction. This point is better illustrated in

**Figure 36** which shows Mean Normalized Bias (MNB) for different simulations. Since data pairs where observed ozone is less than 60 ppb are not included in the MNB calculation, this metric is an indicator of model performance with respect to daytime ozone prediction (or peak ozone prediction). Therefore by eliminating the low nighttime values,

**Figure 36** shows that the model is under-predicting peak ozone. RAQMS_BC simulation which has the highest Mean Bias (MB), as illustrated in **Figure 35**, has the best overall performance during the day as evident from MNB (with the best performance in the Midwest region). SAT_BC and SAT_ICBC simulations overall perform better than the control simulation but cannot outperform RAQMS_BC. Judging from these statistics it seems that the satellite derived boundary condition for the western boundary is much higher than what the surface observations indicate. Then, the predominant west-east flow is transporting the higher ozone to the east and its impact diminishes as the flow reaches the eastern part of the domain. In fact, both SAT_BC and SAT_ICBC simulations perform poor in the west (WRAP) and outperform RAQMS_BC in the southeast region (VISTAS) with respect to daytime ozone predictions. This region is predominantly affected by the BC in the southeastern part of the domain and the daytime satellite profile has been able to explain the impact of transboundary flow to this region.

**Figure 37** is a snapshot of the difference in ozone concentration in the boundary layer (1 km altitude) between SAT_BC and the CNTRL simulations for August 16, 2006. The plot clearly shows the role of transport in advecting ozone from the lateral boundaries into the interior of the

domain. It also shows higher ozone concentrations entering the interior of the domain from the northwestern boundary while the Southeast is more affected by the easterlies. This could partly explain the statistics discussed above. A closer look at the role of transport and the impact of the boundary conditions reveals that the southeast region and the GoM area is more impacted by these easterlies that at times carry the remnants of the northeast pollution through re-circulation.

**Table 12. Performance Statistics for CNTRL Simulation.**
**(August 1-31, 2006 at 36-km grid resolution)**

| Pollutant | CENRAP | MANEVU | MWRPO | VISTAS | WRAP |
|---|---|---|---|---|---|
| Ozone Mean OBS (ppb) | 33 | 33 | 29 | 34 | 34 |
| Ozone Mean PRD (ppb) | 39 | 39 | 37 | 39 | 39 |
| Ozone Bias (ppb) | 6 | 6 | 7 | 6 | 6 |
| Ozone Gross Error (ppb) | 12 | 12 | 13 | 12 | 12 |
| Ozone Normalized Bias (percent) | -10 | -9 | -7 | -11 | -12 |
| Ozone Normalized Error (percent) | 19 | 18 | 19 | 19 | 19 |
| Ozone Fractional Bias (percent) | 24 | 24 | 27 | 23 | 23 |
| Ozone Fractional Error (percent) | 42 | 44 | 49 | 43 | 43 |
| Carbon monoxide Mean OBS ppb | 43 | 40 | 48 | 37 | 45 |
| Carbon monoxide Mean PRD (ppb) | 25 | 24 | 21 | 27 | 25 |
| Carbon monoxide Bias (ppb) | -18 | -17 | -28 | -11 | -20 |
| Carbon monoxide Gross Error (ppb) | 24 | 23 | 35 | 21 | 27 |
| Carbon monoxide Normalized Bias (percent) | -34 | -34 | -43 | -24 | -34 |
| Carbon monoxide Normalized Error (percent) | 50 | 51 | 67 | 51 | 52 |
| Carbon monoxide Fractional Bias (percent) | -44 | -38 | -71 | -30 | -45 |
| Carbon monoxide Fractional Error (percent) | 67 | 69 | 87 | 62 | 69 |
| Sulfur dioxide Mean OBS (ppb) | 4 | 4 | 3 | 3 | 4 |
| Sulfur dioxide Mean PRD (ppb) | 4 | 5 | 4 | 4 | 4 |
| Sulfur dioxide Bias (ppb) | 0 | 1 | 1 | 0 | 0 |
| Sulfur dioxide Gross Error (ppb) | 4 | 4 | 3 | 3 | 4 |
| Sulfur dioxide Normalized Bias (percent) | -57 | -56 | -61 | -54 | -61 |
| Sulfur dioxide Normalized Error (percent) | 68 | 63 | 67 | 62 | 67 |
| Sulfur dioxide Fractional Bias (percent) | 17 | 17 | 34 | 1 | 5 |
| Sulfur dioxide Fractional Error (percent) | 86 | 85 | 80 | 82 | 80 |

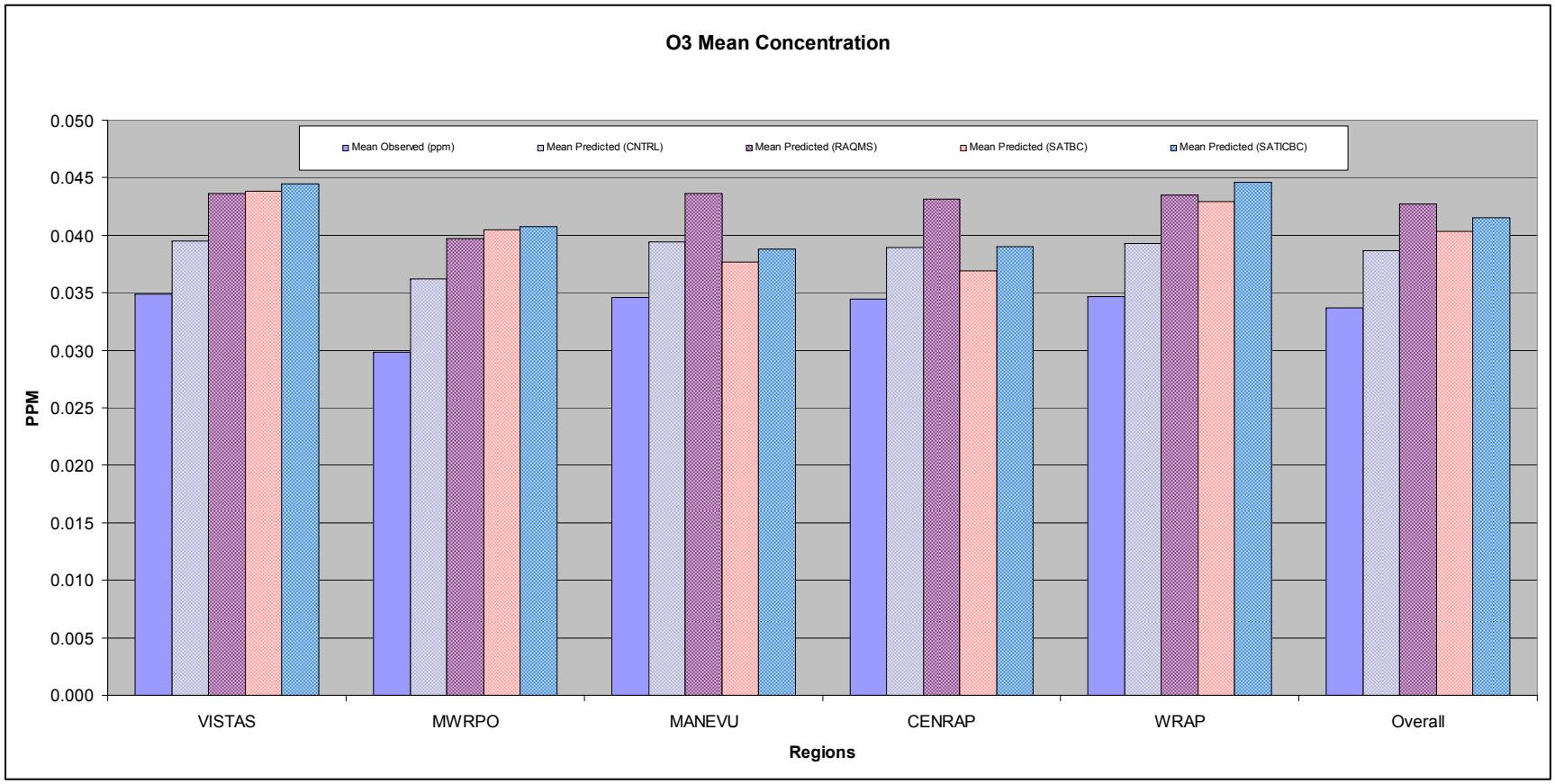


**Figure 35. Mean observed ozone versus model predictions for CNTRL, RAQMS_BC, SAT_BC, and SAT_ICBC simulations for August 2006. The sub-regions are marked on the map in Figure 14.**

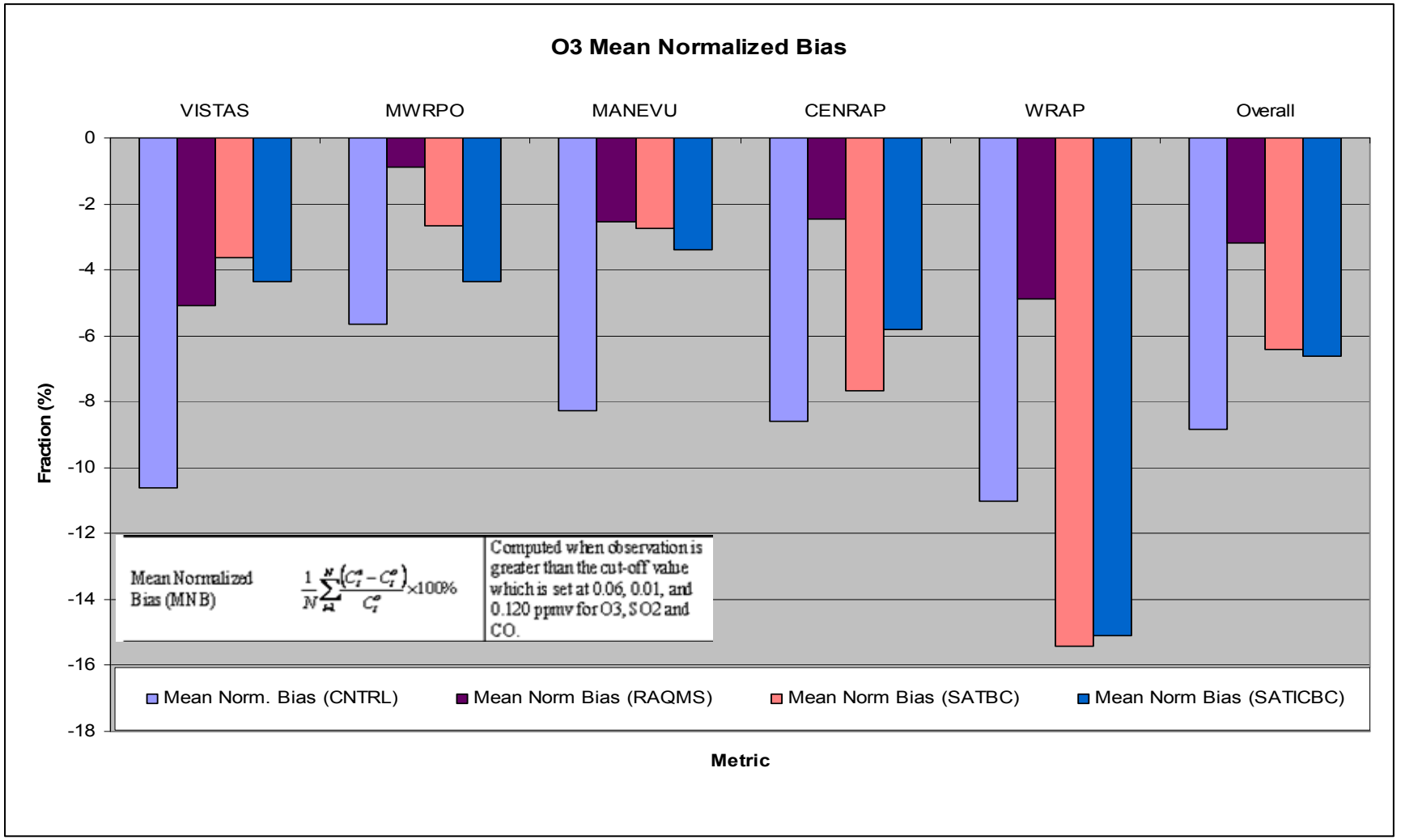


**Figure 36. Mean normalized bias (MNB) for ozone predictions from CNTRL, RAQMS_BC, SAT_BC, and SAT_ICBC simulations. Paired data points where observed ozone is less than 60 ppb are not included (meaning that most of the nighttime and early morning pairs are omitted).**

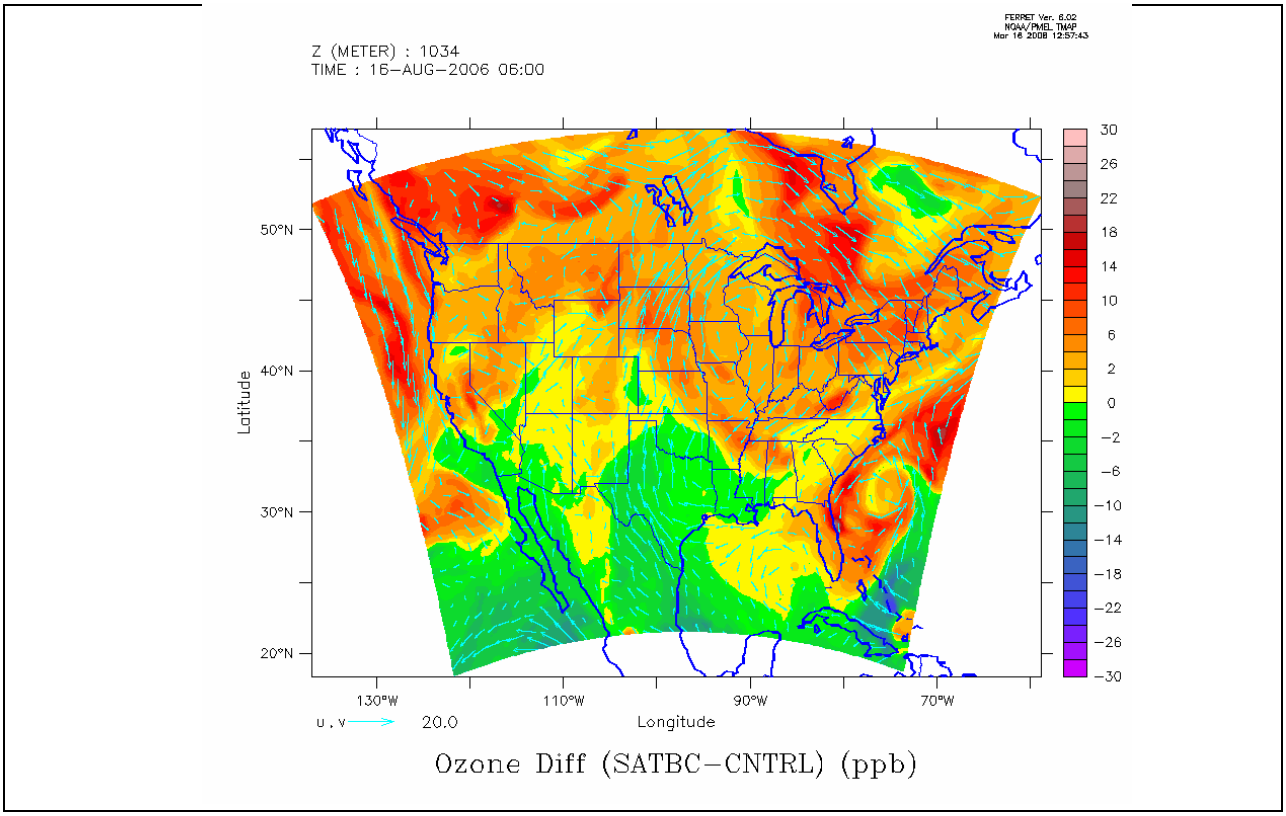


**Figure 37. Difference in ozone concentrations between SAT_BC and CNTRL simulations in the boundary layer for August 16, 2006. The plot clearly shows the role of transport in advecting ozone from the lateral boundaries**

### 3.3.2. $PM_{2.5}$

The results fro SAT_BC and SAT_ICBC also demonstrate the impact of utilizing MODIS AOD products to scale model $PM_{2.5}$ species. As discussed in Section 2.1.2 MODIS AOD products were utilized to scale model $PM_{2.5}$ species to conform to satellite observations. The overall evaluation of the results indicates that the model performance with respect to the prediction of $PM_{2.5}$ total mass has been greatly improved. But since the scaling is based on the assumption that the model partitioning and distribution of $PM_{2.5}$ species is reasonable and the error is due to the magnitude of emissions/transformation, in cases where the partitioning was inaccurate, the inaccuracy was exacerbated. Our future research in this area will try to utilize the data from surface monitors to complement satellite observations and attempt to correct the $PM_{2.5}$ partitioning as well as scaling.

**Figure 38** shows the mean observed mass concentration of $PM_{2.5}$ for different regions versus model predictions from CNTRL and SAT_ICBC simulations. SAT_ICBC simulation shows a marked improvement over CNTRL in predicting $PM_{2.5}$ in all regions and in particular in the Mid-Atlantic/Northeast region where the bias is practically negligible. The overall mean bias

and error shown in **Figure 39** demonstrates that while the use of satellite observations for BC marginally improves model performance, readjusting $PM_{2.5}$ every 24 hours can significantly enhance model predictions of $PM_{2.5}$. This is expected as correcting BC greatly impacts the regions closer to the lateral boundaries of the domain, but initializing the model simulation with a satellite derived field corrects the total mass in the entire domain. By removing the smaller concentrations, the improvements are even more significant as shown in **Figure 40**. As the figure shows, MFB is reduced by about 30%.

A more detailed analysis of the results shows that episodically the satellite derived BC also significantly impact $PM_{2.5}$ over a large region and is able to explain the impact of large scale transport. **Figure 41** shows one such event where there is a large influx of $PM_{2.5}$ from the southeastern boundary impacting the Gulf of Mexico, Louisiana, Texas, Oklahoma, Arkansas and extending into Kansas and Missouri.

Events showing the impact of $PM_{2.5}$ transport are not uncommon. But since in such events the transport is the dominant factor, the accuracy of model predictions of $PM_{2.5}$ is dependent on the ability of the meteorological model in explaining the flow field. One such event is shown in **Figure 42** where a weak cold front approaches the Southeast and gradually passes over the southeastern States. The figure shows MODIS daily AOD product mapped onto the CMAQ grid versus model AOD obtained from CMAQ aerosol predictions. Surface weather charts illustrating the location of the front for each day of August 18-22, 2006 are also presented in the figure. The correlation coefficient, Mean Normalized Bias (MNB) and Variance for model predictions of $PM_{2.5}$ versus MODIS observations for this event is presented in **Table 13**. For August 18 and 19 the model prediction of the front is reasonable and SAT_ICBC simulation shows a reasonable agreement with MODIS observation. The correlation coefficients for these days are .8 for August 18 and .85 for August 19, an improvement over CNTRL simulation with correlation coefficients of .73 and .8 respectively. The spatial plots in **Figure 42** also show a good agreement between the model predictions and observations. The weather charts indicate that on August 20-22, the cold front slowly moves toward the south/southeast. MODIS AOD plots also show a very good agreement with the weather charts as the front is marked with a high AOD spatial gradient. The plots indicate high AOD values to the north of the front as the pollution accumulates and low AOD values to the south of the front. The model also shows the high spatial gradient and also is in agreement with the peak AOD values and their spatial extent as observed by MODIS. However, the front is misplaced by the model as it shows the front much further to the south than the observations indicate. The front in the model is moving to the south/southeast much faster than the observation and therefore by missing the location of the front model is not able to correctly explain the location of observed $PM_{2.5}$ peak. Consequently, the correlation coefficients for August 20-22 for SAT_ICBC simulation are not very different from CNTRL. MNB however goes from negative in CNTRL simulation to positive in SAT_ICBC, indicating that the under-prediction of $PM_{2.5}$ has been corrected but the location is wrong. **Figure 43** shows observed diurnal variation of $PM_{2.5}$ mass concentration from several sites in Alabama and Mississippi against model predictions for the period of August 18-22, 2006. There is a reasonable agreement in the model predicted diurnal pattern, especially for August 18-20, for some of the sites. SAT_ICBC simulation also shows an improvement in predicting $PM_{2.5}$ concentration for August 18-20, but over-predicts $PM_{2.5}$ in the latter part of this period enforcing the previous statements.

Evaluation of model results for individual stations indicated that SAT_ICBC was able to better explain elevated $PM_{2.5}$ episodes.

**Figure 44** shows observed $PM_{2.5}$ concentrations against model predictions over several sites in Alabama for the month of August 2006. While the model perhaps exaggerates the extent of diurnal variation (for some days), it is able to realize gradual increase in $PM_{2.5}$ over the State. In particular, both CNTRL and SAT_ICBC simulations show an increase in $PM_{2.5}$ during August 23-27, 2006, but SAT_ICBC shows a better agreement with the observations.

**Table 13. Correlation Coefficient (R), Mean Normalized Bias (MNB), and Variance for Model $PM_{2.5}$ Predictions (CNTRL and SAT_ICBC simulations) Versus MODIS Observations for the Frontal Event of August 18-22, 2006.**

| Day | 18 | | 19 | | 20 | | 21 | | 22 | |
|---|---|---|---|---|---|---|---|---|---|---|
| | CNTRL | SAT_ICBC | CNTRL | SAT_ICBC. | CNTRL | SAT_ICBC. | CNTRL | SAT_ICBC. | CNTRL | SAT_ICBC. |
| R | 0.732 | 0.80 | 0.798 | 0.850 | 0.619 | 0.644 | 0.623 | 0.769 | 0.609 | 0.661 |
| MNB | -0.433 | -0.064 | -0.302 | 0.133 | -0.109 | 0.299 | -0.114 | 0.264 | -0.168 | 0.140 |
| Variance | 0.041 | 0.019 | 0.037 | 0.017 | 0.045 | 0.045 | 0.055 | 0.034 | 0.046 | 0.039 |

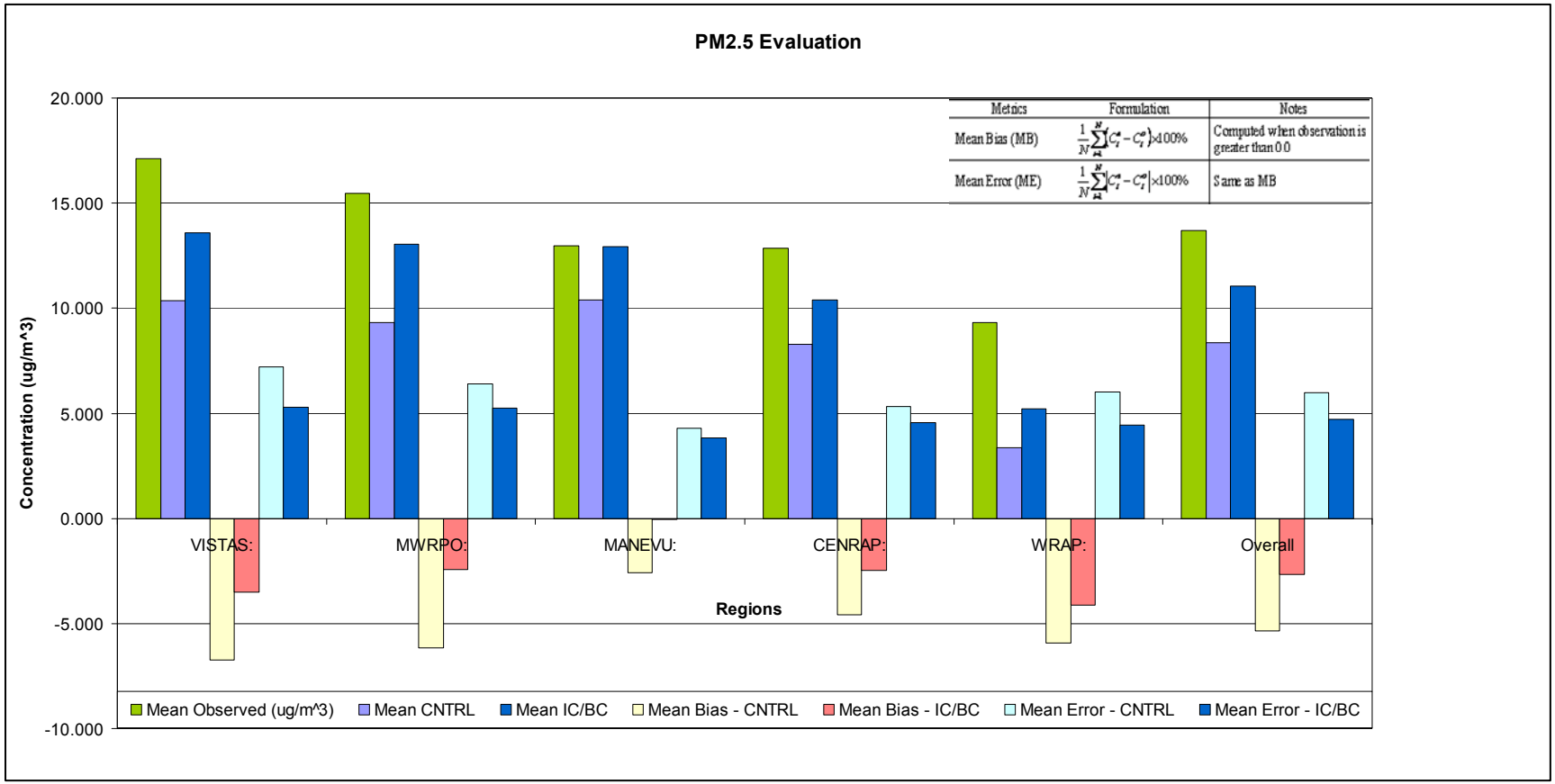


**Figure 38. Observed $PM_{2.5}$ mass concentration ($\mu g/m^3$) for different regions versus model predictions from CNTRL and SAT_ICBC simulations. Also shown in the figure are mean bias and error in model predictions.**

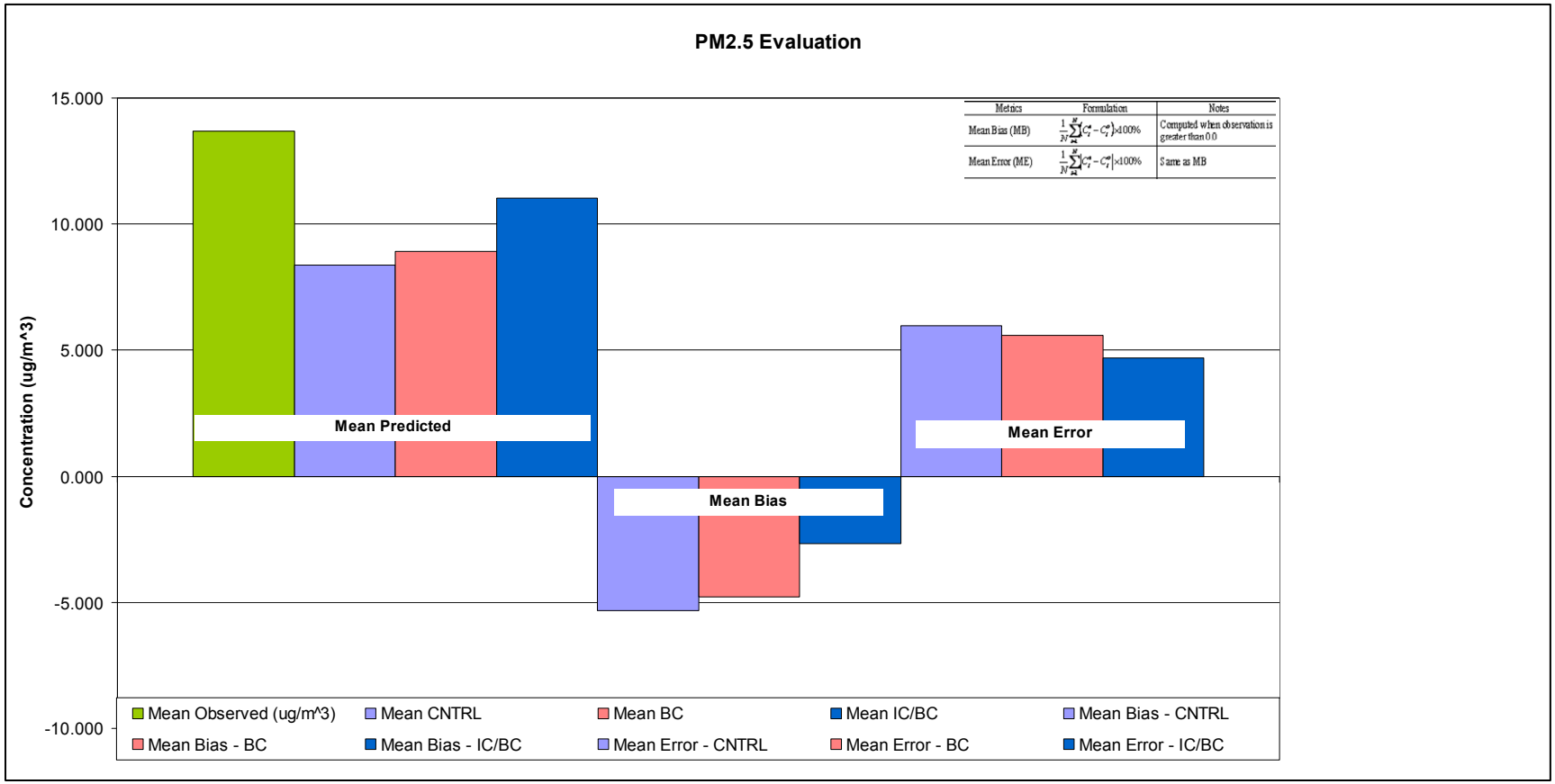


**Figure 39. Mean observed $PM_{2.5}$ mass concentration ($\mu g/m^3$) for August 2006 over the continental U.S. versus model predictions from CNTRL, SAT_BC and SAT_ICBC simulations.**

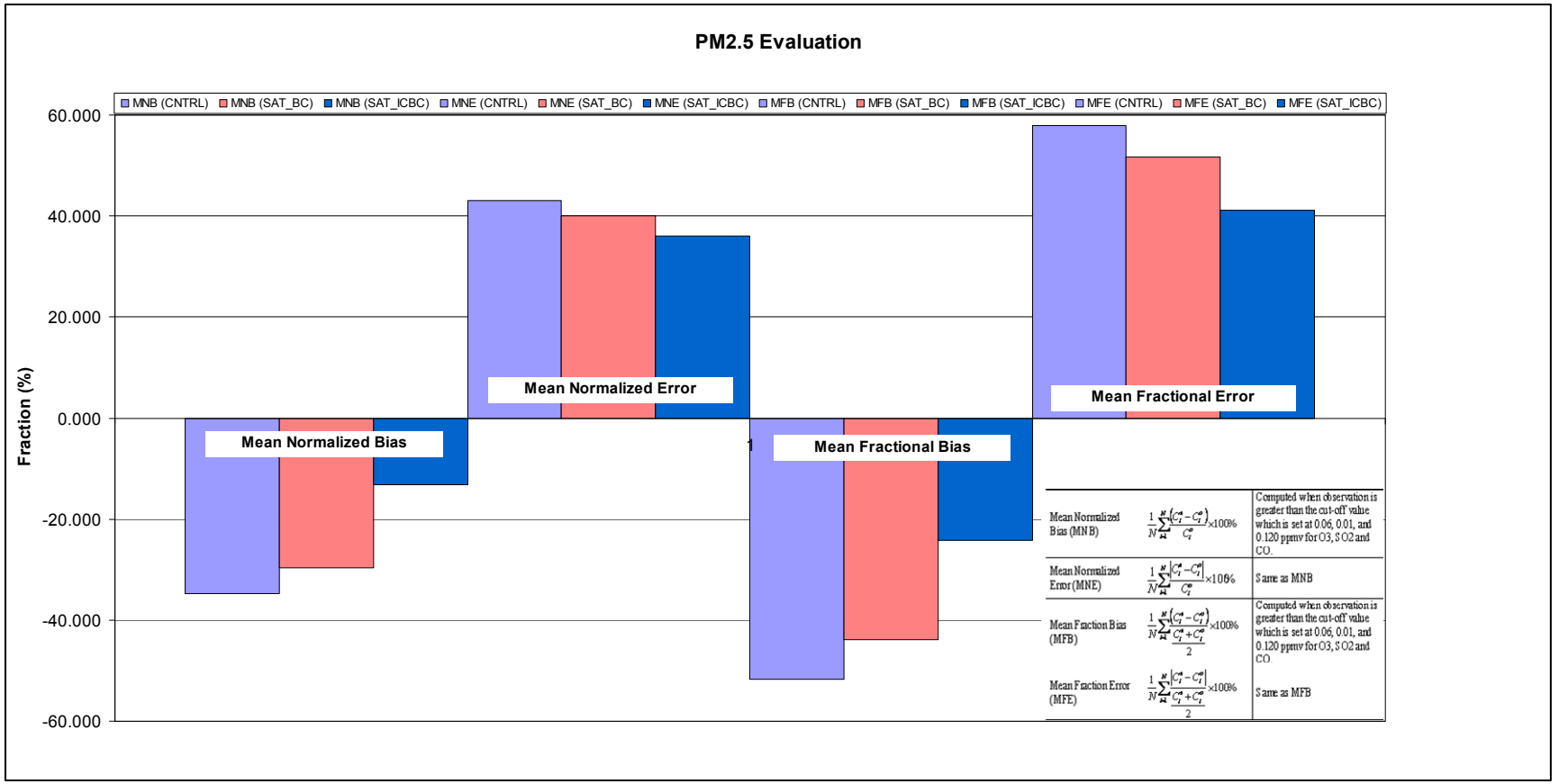


**Figure 40. Mean normalized and fractional bias and error (MNB, MNE, MFB, MFE) for CNTRL, SAT_BC and SAT_ICBC simulations.**

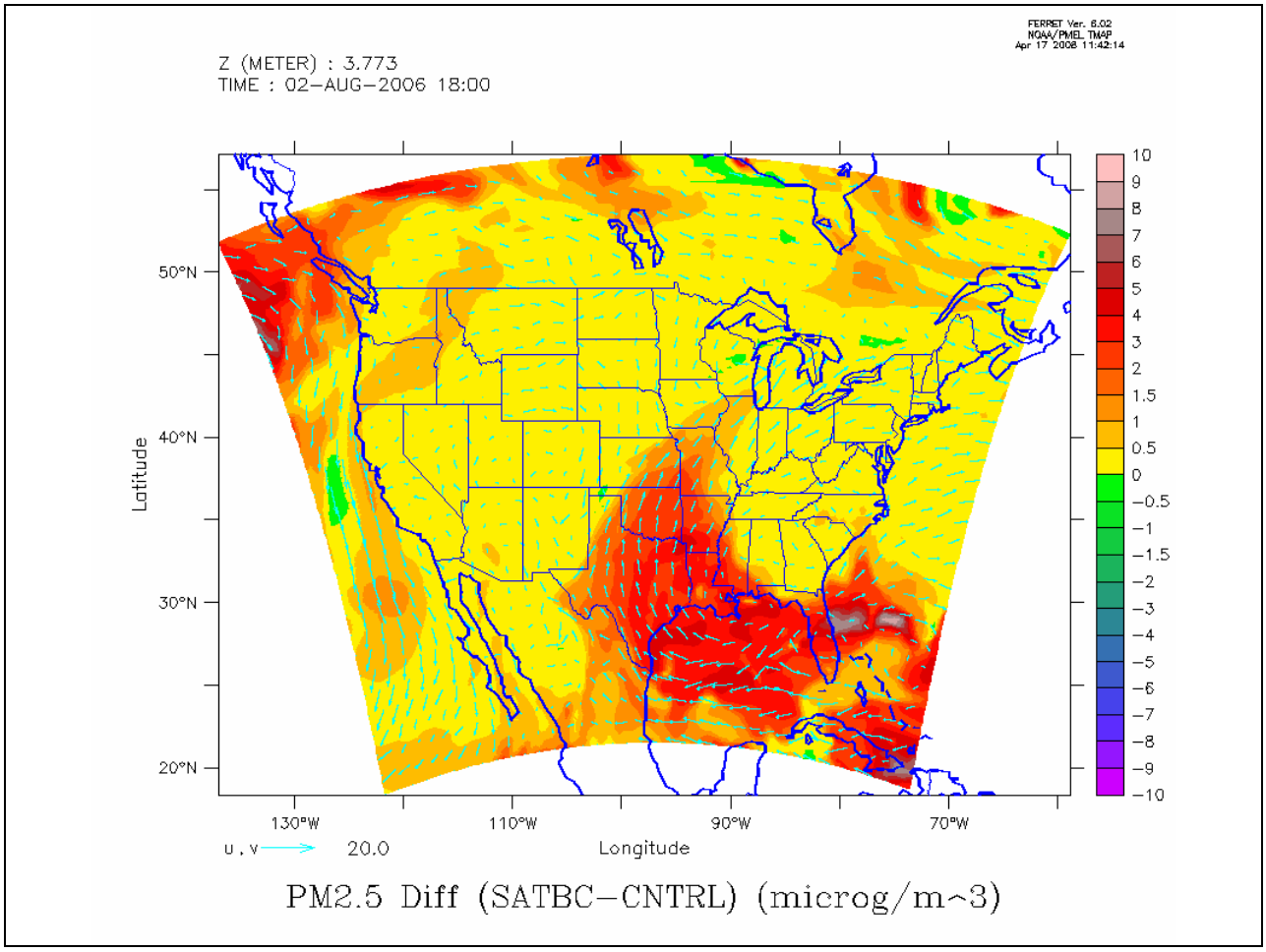


**Figure 41. Difference in surface $PM_{2.5}$ mass concentration ($\mu g/m^3$) between CNTRL and SAT_BC simulations for August 2, 2006, 18:00 GMT.**

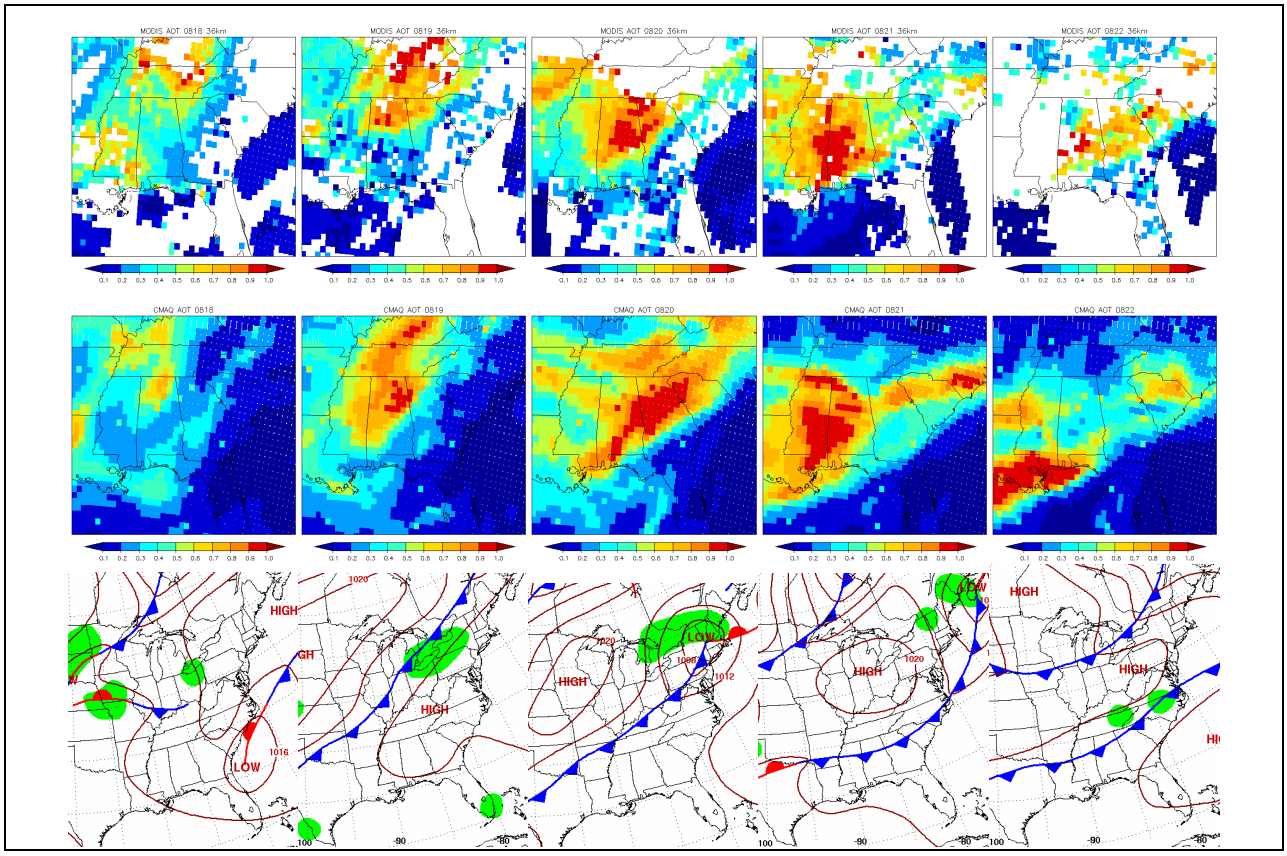


**Figure 42. Frontal passage of August 18-22, 2006, and its impact on $PM_{2.5}$. The top panel shows MODIS AOD, the middle panel shows model AOD based on CMAQ aerosol prediction and the bottom panel shows the surface charts for each day.**

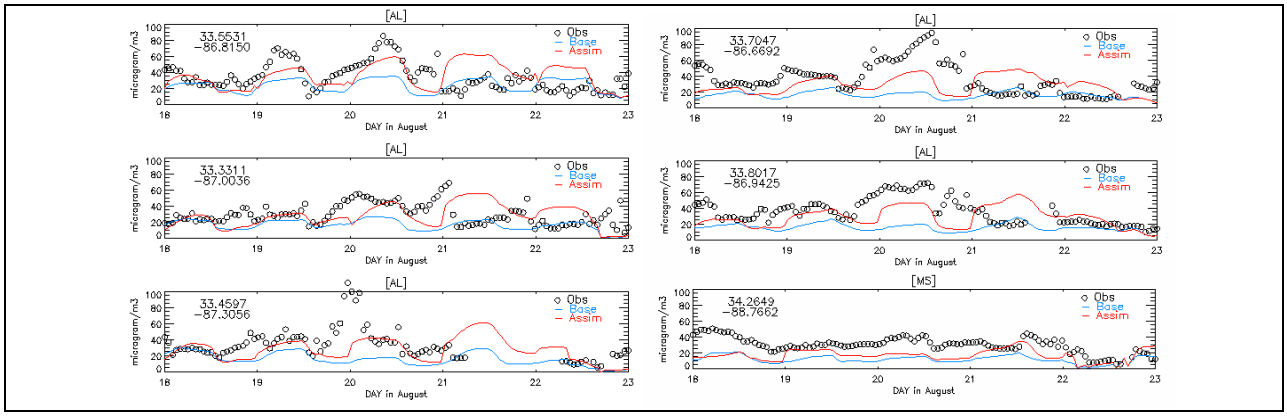


**Figure 43. Observed diurnal variation of $PM_{2.5}$ mass concentration for few monitoring sites in Alabama and Mississippi versus model prediction from CNTRL (here marked as base) and SAT_ICBC (marked as assim) simulations.**

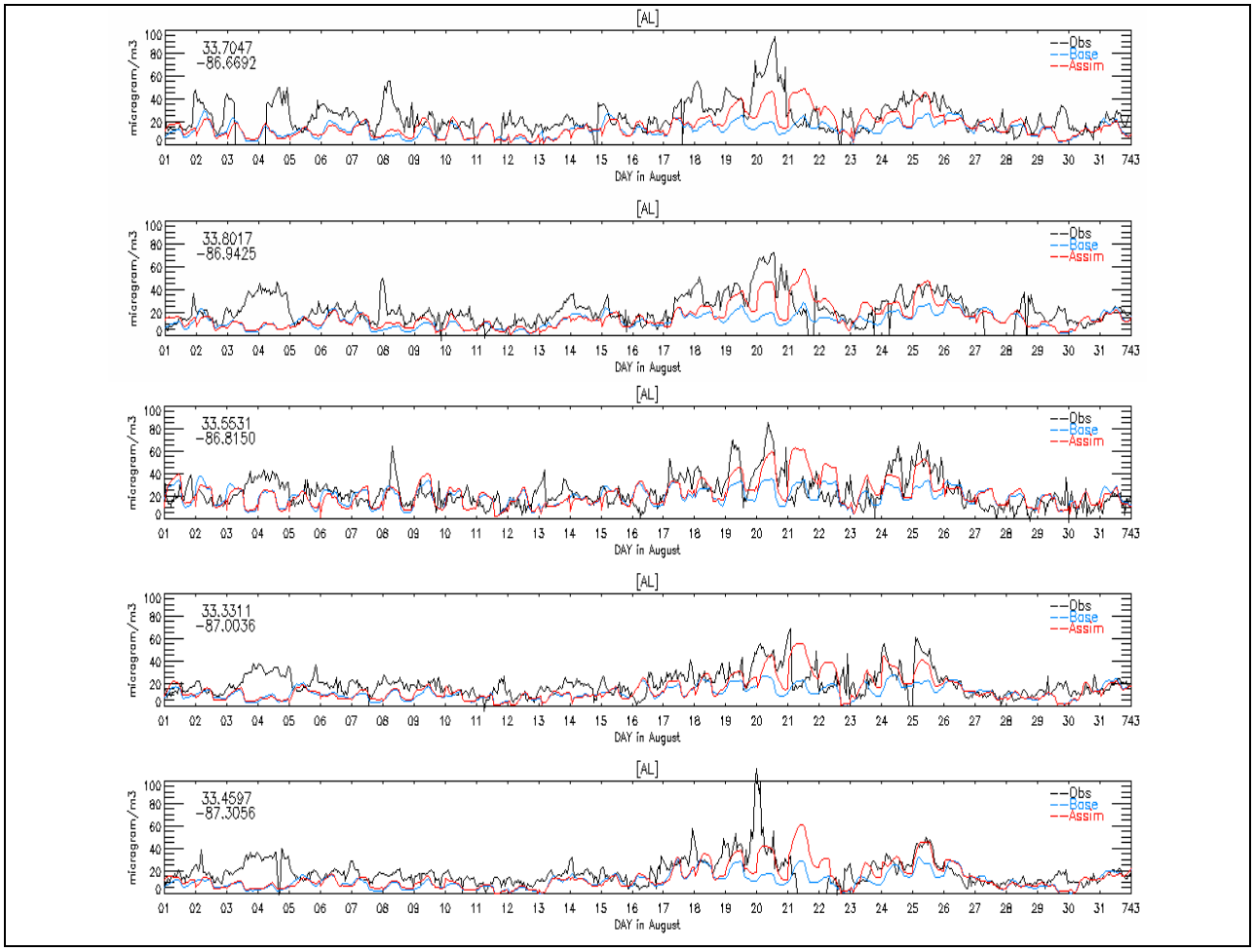


**Figure 44. Observed $PM_{2.5}$ mass concentration for few monitoring sites in Alabama versus model prediction from CNTRL (here marked as base) and SAT_ICBC (marked as assim) simulations for the month of August 2006.**

# 4. CONCLUSION AND RECOMMENDATIONS

Thus far, we have demonstrated the utility of OMI $O_3$ profiles and MODIS aerosol products in CMAQ. OMI $O_3$ significantly improved model performance in the free troposphere and MODIS aerosol products substantially improved $PM_{2.5}$ predictions. There are still issues with respect to the fact that neither OMI nor TES provide adequate information in the boundary layer with respect to $O_3$. Our first efforts, as indicated in this report, have shown marginal improvements in the model performance within the boundary layer. But, with boundary layer $O_3$ being of particular importance to the air quality community, the future work should devise approaches to better characterize pollution episodes. One approach could include the use of other AURA products such as $NO_2$, HCHO, and CO. Since formaldehyde abundance is mainly limited to the boundary layer, column measurements of HCHO can make significant contribution to the better representation of the boundary layer chemical composition.

With respect to the use of aerosol products, while satellite data improved model performance with respect to $PM_{2.5}$ total mass concentration, aerosol speciation remains a challenge. The incorporation of satellite data relied on a key assumption that the aerosol partitioning within the model is reliable. Therefore, revisiting this assumption or improving the aerosol model within CMAQ takes higher priority.

The current project examined the impact of the boundary conditions (BC) on the air quality predictions. The utilization of the satellite data for BC was helpful in the realization of transboundary transport of pollution and helped in better representation of the free tropospheric ozone. Our hypothesis that the recirculation of pollution from Northeast Corridor can play a role over the Gulf of Mexico (GoM) was tested and our model simulations show evidence of such possibility. The episodic transport of pollution by easterlies over the GoM and the southeastern region suggests that in particular the specification of the lateral boundaries and the background air in modeling practices in this region is important.

In this project we also utilized daily information from the satellite to improve the initial condition in the model. This effort can lead to effectively assimilate the satellite data into the model fields. Since the initial conditions greatly impact the short term predictions, use of satellite data for IC can also potentially improve air quality forecasts. The utilization of MODIS AOD in specifying IC greatly improved model prediction of $PM_{2.5}$ concentrations. Our overall assessment of the utility of satellite ozone observations for air quality studies is that the quality of the data for the boundary layer is not satisfactory. OMI observations are valuable in improving ozone fields in the free troposphere which in turn can affect ozone abundance in the boundary layer, but are not adequate to explain the low background ozone concentration in the boundary layer. Ozone in the mid- to upper-troposphere is largely dominated by transport, while the ozone within boundary layer is mostly affected by fast production/loss mechanisms that are impacted by surface emissions, chemistry and removal processes.

The current project did not examine the role of assimilation in improving the physical atmosphere. Future efforts should include an improved physical atmosphere in conjunction with the assimilation of satellite trace gases. For example, it has been shown that the assimilation of

satellite-observed clouds greatly improves model predictions of ozone within the boundary layer. It also eliminates one component of inconsistency between the model and the observations. One of the problems in satellite data assimilation is that the observed physical/chemical world is not always consistent with the model world. A major manifestation of this inconsistency is with respect to the clouds. A discrepancy between model clouds (clear sky) and the satellite clouds (clear sky) impacts the radiation fields, vertical transport and local circulations, the chemistry and microphysical properties. This means that when one component of physical or chemical atmosphere is perturbed (adjusted) by the assimilation of satellite data, the complete environment for supporting and sustaining the adjustment does not exist. Therefore, as we continue to introduce more chemical observations into the modeling framework, it is essential that in a parallel effort we make the physical environment more realistic. This means the inclusion of assimilation of satellite observed skin temperature, moisture, albedo, insolation, and clouds in conjunction with the assimilation of trace gases and aerosols.

Finally, while satellite observation of ozone alone did not fulfill our expectations for air quality studies, the use of satellite observation of ozone and other trace gases in conjunction with surface observations needs to be investigated. For example, there are complementary satellite observations (as indicated before) such as nitrogen dioxide ($NO_2$), formaldehyde (HCHO), and carbon monoxide (CO) that can help in specifying the background air. Also, the routine surface observations can be used to scale satellite observation and introduce diurnal variation to the measurements. Surface measurements, while detailed and continuous, are point measurements and lack the ability of representing a larger region. On the other hand, the information from A-Train polar orbiting satellites is an early afternoon snap shot of the atmosphere and represents an average quantity over a larger area. A natural extension of the efforts documented in this report would be to examine the feasibility of such approaches.

The modeling simulations reported here used relatively coarse grid spacing over the continental United States and was able to explain the large scale impact of long range transport. However, a future study should examine the utilization of the techniques and the data used in this study for a smaller domain over the southeastern U.S. with finer grid spacing.

***Acknowledgments.*** This work was accomplished under partial support from Cooperative Agreement Between the University of Alabama in Huntsville and the Bureau of Ocean Energy Management, Regulation and Enforcement on Gulf of Mexico Issues, and the NASA Science Mission Directorate Applied Sciences Program.

# 5. REFERENCES


Al-Saadi, J., A. Soja, R.B. Pierce, J. Szykman, C. Wiedinmyer, L. Emmons, S. Kondragunta, X. Zhang, C. Kittaka, T. Schaack, and K. Bowman. 2008. Evaluation of near-real-time biomass burning emissions estimates constrained by satellite active fire detections. Journal of Applied Remote Sensing 2:021504, [doi: 10.1117/1.2948785].

Anthes, R.A. and T.T. Warner. 1978. Development of hydrodynamic models suitable for air pollution and other mesometeorological studies. Mon. Wea. Rev. 106:1045-1078.

Beer, R. 2006. TES on the Aura Mission: Scientific objectives, measurements and analysis overview. IEEE Trans. Geosci. Remote. Sens. 44:1102– 1105.

Beer, R., T.A. Glavich, and D.M. Rider. 2001. Tropospheric emission spectrometer for the Earth Observing System's Aura satellite. Appl. Opt. 40:2356–2367.

Bhave, P.V., S. J. Roselle, F.S. Binkowski, C.G. Nolte, S.C. Yu, G.L. Gipson, and K.L. Schere. 2004. CMAQ aerosol module development: Recent enhancements and future plans., Proceedings of the 2004 Models-3/CMAQ Conference, Chapel Hill, N.C., 18–20 October 2004. Internet website: http://www.cmascenter.org/conference/2004/abstracts/Model%20Development/bhave_abstract.pdf.

Binkowski, F.S. and S.J. Roselle. 2003. Models-3 community multiscale air quality (CMAQ) model aerosol component: 1. Model description. J. Geophys. Res. 108(D6):4183, doi:10.1029/2001JD001409.

Bowman K.W., C. D. Rodgers, S.S. Kulawik, J. Worden, E. Sarkissian, G. Osterman, T. Steck, M. Lou, A. Eldering, M. Shephard, H. Worden, M. Lampel, S. A. Clough, P. D. Brown, C. P. Rinsland, M. Gunson, and R. Beer. 2006. Tropospheric emission spectrometer: Retrieval method and error analysis. IEEE Trans. Geosci. Remote Sens. 44(5):1297-1307.

Bowman, K.W., J. Worden, T. Steck, H. M. Worden, S. Clough, and C. Rodgers. 2002. Capturing time and vertical variability of tropospheric ozone: A study using TES nadir retrievals. J. Geophys. Res.-Atmos. 107 :4723.

Brasseur, G., J. Kiehl, J.-F. Müller, T. Schneider, C. Granier, X. Tie, and D. Hauglustaine. 1998. Past and future changes in global tropospheric ozone: Impact on radiative forcing. Geophys. Res. Lett. 25(20):3807-3810.

Brewer J., P. Dolwick, and R. Gilliam. 2007. Regional and local scale evaluation of MM5 meteorological fields for various air quality modeling applications. Presented at the 87th Annual American Meteorological Society Annual Meeting, San Antonio, TX, January 15-18, 2007.

Burrows, J.P., M. Weber, M. Buchwitz, V. Rozanov, A Ladstatter-Weissenmayer, A. Richter, R. De Beek, R. Hoogen, K. Bramstedt, K.W. Eichmann, M. Eisinger, and D. Perner. 1999. The Global Ozone Monitoring Experiment (GOME): Mission concept and first scientific results. J. Atmos. Sci. 56:151-175.

Byun, D.W. and K.L. Schere. 2006. Review of governing equations, computational algorithms, and other components of the models-3 Community Multiscale Air Quality (CMAQ) modeling system. Appl. Mech. Rev. 59:51–77.

Chance, K. 1998. Analysis of BrO Measurements from the Global Ozone Monitoring Experiment, Geophys. Res. Lett. 25:3335-3338.

Chandra, S., J.R. Ziemke, and R.V. Martin. 2003. Tropospheric ozone at tropical and middle latitudes derived from TOMS/MLS residual: Comparison with a global model. J. Geophys. Res. 108(D9):4291, doi:10.1029/2002JD002912.

Chang, J.S., P.B. Middleton, W.R. Stockwell, C.J. Walcek, J.E. Pleim, H.H. Lansford, F.S. Binkowski, S. Madronich, N.L. Seaman, D.R. Stauffer, D. Byun, J.N. McHenry, P.J. Samson, and H. Hass. 1990. The regional acid deposition model and engineering model. Acidic Deposition: State of Science and Technology. Report 4, National Acid Precipitation Assessment Program.

Chang, J.S., R.A. Brost, I.S.A. Isaksen, S. Madronich, P. Middleton, W.R. Stockwell, and C.J. Walcek. 1987. A three-dimensional Eulerian acid deposition model: Physical concepts and formulation. J. Geophys. Res. 92(D12):14681-14700.

Coats, C.J. Jr. 1996. High-performance algorithms in the Sparse Matrix Operator Kernel Emissions (SMOKE) modeling system. Proc. Ninth AMS Joint Conference on Applications of Air Pollution Meteorology with A&WMA, Amer. Meteor. Soc., Atlanta, GA, Pp. 584-588.

DeMore, W.B., S.P. Sander, D.M. Golden, R.F. Hampson, M.J. Kurylo, C.J. Howard, A.R. Ravishankara, C.E. Kolb, and M.J. Molina. 1994. Chemical kinetics and photochemical data for use in stratospheric modeling: Evaluation number 11. JPL Pub. 94-26. Pasadena, CA: National Aeronautics and Space Administration, Jet Propulsion Laboratory.

Dennis, R.L., D.W. Byun, J.H. Novak, K.J. Galluppi, C.J. Coats, and M.A. Vouk. 1996. The next generation of integrated air quality modeling: EPA's Models-3. Atmos. Env. 30(12):1925-1938.

Dudhia, J. 1989. Numerical study of convection observed during the winter monsoon experiment using a mesoscale two-dimensional model. J. Atmos. Sci. 46:3077-3107.

Emery, C.A., E. Tai, and G. Yarwood. 2001. Enhanced meteorological modeling and performance evaluation for two Texas ozone episodes. Texas Natural Resource Conservation Commission, ENVIRON International Corp, 2001, Novato, CA.

EPA. 1999. Science Algorithms of the EPA Models-3 Community Multiscale Air Quality (CMAQ) Modeling System. EPA-600/R-99/030.

Fishman, J. and V.G. Brackett. 1997. The climatological distribution of tropospheric ozone derived from satellite measurements using version 7 Total Ozone Mapping Spectrometer and Stratospheric Aerosol and Gas Experiment data set. J. Geophys. Res. 102:19275-19278.

Grell, G.A., J. Dudhia, and D.R. Stauffer. 1994. A Description of the Fifth-Generation Penn State/NCAR Mesoscale Model (MM5). NCAR Technical Note NCAR/TN-398+STR, National Center for Atmospheric Research, Boulder, CO.

Guenther, A., C. Geron, T. Pierce, B. Lamb, P. Harley, and R. Fall. 2000. Natural emissions of non-methane volatile organic compounds, carbon monoxide, and oxides of nitrogen from North America. Atmos. Environ. 34:2205-2230.

Hand, J.L. and W.C. Malm. 2005. Review of the IMPROVE equation for estimating ambient light extinction coefficients. Internet website: http://vista.cira.colostate.edu/improve/Publications/GrayLit/gray_literature.htm

Hoogen, R., V.V. Rozanov, K. Bramstedt, K.-U. Eichmann, M. Weber, and J.P. Burrows. 1999. Ozone profiles from GOME satellite data-I: Comparison with ozonesonde measurements. Physics and Chemistry of the Earth 24:447-452.

Houyoux, M.R., J.M. Vukovich, C.J. Coats, Jr., N.W. Wheeler, and P.S. Kasibhatla. 2000. Emission inventory development and processing for the seasonal model for regional air quality (SMRAQ) project. J. Geophys. Res. Atmospheres 105(D7):9079-9090

Kemball-Cook, S., Y. Jia, C. Emery, R. Morris, Z. Wang, and G. Tonnesen. 2005. Annual 2002 MM5 meteorological modeling to support regional haze modeling of the Western United States. Prepared for The Western Regional Air Partnership (WRAP), 1515 Cleveland Place, Suite 200 Denver, CO 80202.

Kim, J.H. and M.J. Newchurch. 1998. Biomass-burning influence on tropospheric ozone over New Guinea and South America. J. Geophys. Res. 103:1455–1461.

Kim, J.H., M.J. Newchurch, and K. Han. 2001. Distribution of tropical tropospheric ozone determined by the scan-angle method applied to TOMS measurements. J. Atmos. Sci. 58(18):2699–2708.

Komhyr, W.D., R.A. Barnes, G.B. Brothers, J.A. Lathrop, and D.P. Opperman. 1995. Electrochemical concentration cell ozonesonde performance evaluation during STOIC. 1989. J. Geophys. Res. 100:9231–9244, doi:10.1029/94JD02175.

Kulawik S.S., J. Worden, A. Eldering, K. Bowman, M. Gunson, G.B. Osterman, L. Zhang, S. Clough, M.W. Shephard, and R. Beer. 2006. Implementation of cloud retrievals for Tropospheric Emission Spectrometer (TES) atmospheric retrievals. Part 1: Description and characterization of errors on trace gas retrievals. J. Geophys. Res. 111:D24204, doi:10.1029/2005JD006733.

Liu, X., K. Chance, C.E. Sioris, R.J.D. Spurr, T.P. Kurosu, R.V. Martin, and M.J. Newchurch. 2005. Ozone profile and tropospheric ozone retrieval from global ozone monitoring experiment (GOME): Algorithm description and validation. J. Geophys. Res. 110(D20):D20307, doi:10.1029/2005 JD006240.

Liu X., K. Chance, C.E. Sioris, T.P. Kurosu, R.J.D. Spurr, R.V. Martin, M. Fu, J.A. Logan, D.J. Jacob, P.I. Palmer, M.J. Newchurch, I. Megretskaia, and R. Chatfield. 2006a. First directly-retrieved global distribution of tropospheric column ozone: comparison with the GOES-CHEM model. J. Geophys. Res. 111(D2):D02308, doi:10.1029/2005JD006564.

Liu, X., K. Chance, C.E. Sioris, T.P. Kurosu, and M.J. Newchurch. 2006b. Intercomparison of GOME, ozonesonde, and SAGE-II measurements of ozone: Demonstration of the need to homogenize available ozonesonde datasets. J. Geophys. Res. 101(D14):D114305, doi:10.1029/2005JD006718.

Nassar, R., J.A. Logan, H.M. Worden, I.A. Megretskaia, K.W. Bowman, G.B. Osterman, A.M. Thompson, D.W. Tarasick, S. Austin, H. Claude, M.K. Dubey, W.K. Hocking, B.J. Johnson, E. Joseph, J. Merrill, G.A. Morris, M. Newchurch, S.J. Oltmans, F. Posny, F.J. Schmidlin, H. Vömel, D.N. Whiteman, and J.C. Witte. 2008. Validation of Tropospheric Emission Spectrometer (TES) nadir ozone profiles using ozonesonde measurements. J. Geophys. Res. 113:D15S17, doi:10.1029/2007JD008819.

Newchurch, M.J., X. Liu, and J.H. Kim. 2001. Lower-tropospheric ozone (LTO) derived from TOMS near mountainous regions, J. Geophys. Res. 106 :20 403–20 412, 2001.

Osterman, G. (ed.) 2006. TES L2 data user's guide : Vers. 2.0. Jet Propulsion Laboratory, California Institute of Technology. Internet website: http://tes.jpl.nasa.gov/docsLinks/DOCUMENTS/TESL2DataUsersGuidev2.0.pdf.

Osterman, G.B., S.S. Kulawik, H.M. Worden, N.A.D. Richards, B.M. Fisher, A. Eldering, M.W. Shephard, L. Froidevaux, G. Labow, M. Luo, R.L. Herman, K.W. Bowman and A.M. Thompson. 2008. Validation of Tropospheric Emission Spectrometer (TES) measurements of the total, stratospheric, and tropospheric column abundance of ozone. J. Geophys. Res. 113:D15S16, doi:10.1029/2007JD008801.

Otte, T.L., A. Lacser, S. Dupont, and J.K.S. Ching. 2004. Implementation of an urban canopy parameterization in a mesoscale meteorological model. Journal of Applied Meteorology 43:1648-1665.

Otte, T.L., G. Pouliot, J.E. Pleim, J.O. Young, K.L. Schere, D.C. Wong, P.C.S. Lee, M. Tsidulko, J.T. McQueen, P. Davidson, R. Mathur, H.Y. Chuang, G. DiMego, and N.L. Seaman. 2005. Linking the Eta Model with the Community Multiscale Air Quality (CMAQ) Modeling System to build a national air quality forecasting system. Weather and Forecasting 20:367–384.

Park M., W.J. Randel, D.E. Kinnison, R.R. Garcia, and W. Choi. 2004. Seasonal variation of methane, water vapor, and nitrogen oxides near the tropopause: Satellite observations and model simulations. J. Geophys. Res. 109:D03302, doi:10.1029/2003JD003706.

Pierce, T., C. Geron, L. Bender, R. Dennis, G. Tonnesen, and A. Guenther. 1998. Influence of increased isoprene emissions on regional ozone modeling. J. Geophys. Res. 103(D19):25611-25629.

Rodgers, C.D. 2000. Inverse methods for atmospheric sounding: Theory and practice. London: World Science Publishing. 238 pp.

Rodgers, C.D., and B.J. Connor. 2003. Intercomparison of remote sounding instruments. J. Geophys. Res. 108(D3):4116, doi:10.1029/2002JD002299.

Schoeberl, M.R., A.R. Douglass, E. Hilsenrath, P.K. Bhartia, J. Barnett, R. Beer, J. Waters, M. Gunson, L. Froidevaux, J. Gille, P.F. Levelt, and P. DeCola. 2006. Overview of the EOS Aura Mission. IEEE Trans. Geosci. Remote Sensing 44(5):1066-1074, May 2006.

Smit, H.G., W. Straeter, B.J. Johnson, S.J. Oltmans, J. Davies, D.W. Tarasick, B. Hoegger, R. Stubi, F.J. Schmidlin, and T. Northam. 2007. Assessment of the performance of ECC-ozonesondes under quasi-flight conditions in the environmental simulation chamber: Insights from the Juelich Ozone Sonde Intercomparison Experiment (JOSIE). J Geophys Res. 112:D19306, doi:10.1029/2006JD007308.

Song, C.K., D.W. Byun, R.B. Pierce, J.A. Alsaadi, T.K. Schaack, and F. Vukovich. 2008. Downscale linkage of global model output for regional chemical transport modeling: Method and general performance. J. Geophys. Res. 113:D08308, doi:10.1029/2007JD008951.

Tang, Y., G.R. Carmichael, N. Thongboonchoo, L. Horowitz, G. Pfister, T. Chai, M.A. Avery, R.B. Pierce, J.A. Al-Saadi, T.B. Ryerson, G.W. Sachse, and J. Holloway. 2007. Influence of lateral and top boundary conditions on regional air quality prediction: A multiscale study coupling regional and global chemical transport models. J. Geophys. Res. 112:D10S18, doi:10.1029/2006JD007515

Thompson, A.M., J.B. Stone, J.C. Witte, S.K. Miller, R.B. Pierce, R.B. Chatfield, S.J. Oltmans, O.R. Cooper, A.L. Loucks, and B.F. Taubman. 2007a. Intercontinental chemical transport experiment ozonesonde network study (IONS) 2004: 1. Summertime upper troposphere/lower stratosphere ozone over northeastern North America. J. Geophys. Res. 112:D12S12, doi:10.1029/2006JD007441.

Thompson, A.M., J.B. Stone, J.C. Witte, S.K. Miller, S.J. Oltmans, T.L. Kucsera, K.L. Ross, K.E. Pickering, J.T. Merrill, and G.Forbes. 2007b. Intercontinental chemical transport experiment ozonesonde networks (IONS) 2004: 2. Tropospheric ozone budgets and variability over northeastern North America. J. Geophys. Res. 112:D12S13, doi:10.1029/2006JD007670.

Worden, H.M., J.A. Logan, J.R. Worden, R. Beer, K. Bowman, S.A. Clough, A. Eldering, B.M. Fisher, M.R. Gunson, R.L. Herman, S.S. Kulawik, M.C. Lampel, M. Luo, I.A. Megretskaia, G.B. Osterman, and M.W. Shephard. 2007. Comparisons of Tropospheric Emission Spectrometer (TES) ozone profiles to ozonesondes: Methods and initial results. J. Geophys. Res. 112:D03309, doi:10.1029/2006JD007258.

Worden, J., S.S. Kulawik, M.W. Shephard, S.A. Clough, H. Worden, K. Bowman, and A. Goldman. 2004. Predicted errors of tropospheric emission spectrometer nadir retrievals from spectral window selection. J. Geophys. Res. 109:D09308, doi:10.1029/2004JD004522.

Ziemke, J.R., S. Chandra, and O.K. Bhartia. 2000. A new NASA data product: Tropospheric and statospheric column ozone in the tropics derived from TOMS measurements. Bul. Amer. Meteorl. Soc. 81:580–583.